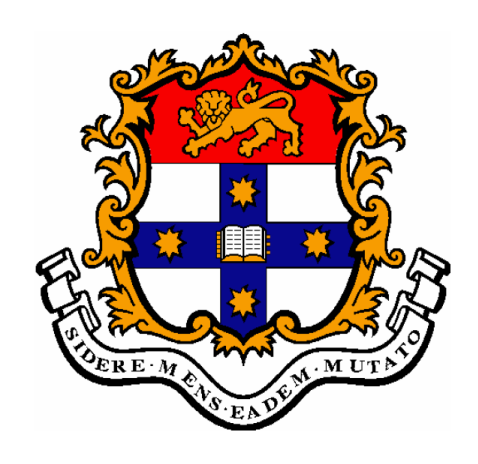
# THE SIMULATION OF

# A NOCTURNAL CLOUD-TOPPED

# **ATMOSPHERIC BOUNDARY LAYER**



A Thesis submitted to the

School of Aerospace, Mechanical and Mechatronic Engineering,

The University of Sydney,

in fulfillment of the requirements of

Bachelor of Engineering (Mechanical) Honours

BY

NEJTEH M. DEMIRIAN

November 2009

To my parents and siblings

Thank you for everything

I owe it all to you...

And to Michael

It has been a pleasure, so thank you.

I hope this makes a small difference...

# **DECLARATION**

I, Nejteh Movses Demirian, hereby declare that t	the work embodied in this Thesis,
submitted in fulfillment of Bachelor of Engineering	g (Mechanical) Honours, represents
my own work and has not been previously submitt	ted to The University of Sydney or
any other institution for any degree or other qualifica	ation.
	N. K. I. D
	Nejteh Demirian
Docto	or Michael Kirkpatrick

# TABLE OF CONTENTS

LIST OF F	IGURES	vi
LIST OF T	ABLES	vi
ACKNOW	LEDGEMENTS	vii
ABSTRAC	Т	viii
1 INTROI	DUCTION	1
	ATURE REVIEW	
2.1	EARLY MICROPHYSICS PARAMETERISATIONS	
2.1.1 2.1.2	Autoconversion	
2.1.2		
2.1.3	•	
2.2	FURTHER DEVELOPMENT OF MICROPHYSICS SCHEMES.	
2.2.1	Autoconversion and accretion processes based on collision theory	
2.2.2		
2.2.3		
2.3	SINGLE MOMENT BULK MICROPHYSICS SCHEME	
2.3.1	Autoconversion	
2.3.2		
2.3.3	r	
2.4	COMPARISON OF CURRENT MICROPHYSICS SCHEMES	
2.4.1	Single-moment bulk microphysics models	
2.4.2	- · · · - · - · · · · · · · · · · · · ·	
2.4.3 <b>2.5</b>	Bin microphysics schemes	
2.5.1	Two-stream and multi-band scheme comparison	
2.5.1		
3. MODEI	DESCRIPTIONS	
3.1	MICRO-PROCESSES INVOLVED IN THE MICROPHYSICS	
3.1.1		
3.1.2	Autoconversion	
3.1.3	Accretion	
3.1.4	· · · · · · · · · · · · · · · · · · ·	
3.2	MICROPHYSICS – SOURCE TERMS	
3.2.1	The folder wester missing restrict form	
3.2.2 3.2.3	The rainwater mixing ratio source term The liquid water potential temperature source term	
3.3	RADIATION	
4. SIMUL	ATION SETUP	36
4.1	PUFFIN-ABL BOUNDARY CONDITIONS	36
4.1.1		37
4.1.2	Boundary Conditions	
4.2	Boundary ConditionsSurface fluxes	
	Surface fluxes	<i>38</i> 38
4.2.1	Surface fluxes	38 38 39
4.2.2	Surface fluxes INITIAL CONDITIONS Physical Constants Microphysics	38 39 39
4.2.2 4.2.3	Surface fluxes  INITIAL CONDITIONS  Physical Constants  Microphysics  Simulation Parameters Summary	
4.2.2 4.2.3 <b>4.3</b>	Surface fluxes INITIAL CONDITIONS Physical Constants Microphysics Simulation Parameters Summary ANALYSIS METHODS	
4.2.2 4.2.3 <b>4.3</b> 4.3.1	Surface fluxes INITIAL CONDITIONS Physical Constants Microphysics Simulation Parameters Summary ANALYSIS METHODS Temporal inversion height variation	38 38 39 39 40 41
4.2.2 4.2.3 <b>4.3</b> 4.3.1 4.3.2	Surface fluxes.  INITIAL CONDITIONS.  Physical Constants.  Microphysics  Simulation Parameters Summary.  ANALYSIS METHODS.  Temporal inversion height variation.  Third moment of vertical velocity profile, < w' <sup>3</sup> >	38 38 39 39 40 41 41
4.2.2 4.2.3 <b>4.3</b> 4.3.1 4.3.2 4.3.3	Surface fluxes  INITIAL CONDITIONS  Physical Constants  Microphysics  Simulation Parameters Summary  ANALYSIS METHODS  Temporal inversion height variation  Third moment of vertical velocity profile, < w <sup>13</sup> >  Vertical statistical profile analysis	38 38 39 39 40 41 41 42
4.2.2 4.2.3 <b>4.3</b> 4.3.1 4.3.2 4.3.3 <b>4.4</b>	Surface fluxes.  INITIAL CONDITIONS  Physical Constants  Microphysics  Simulation Parameters Summary.  ANALYSIS METHODS  Temporal inversion height variation  Third moment of vertical velocity profile, < w <sup>13</sup> > Vertical statistical profile analysis.  DII-SERIES SIMULATIONS.	38 38 39 39 40 41 41 42 44 44
4.2.2 4.2.3 <b>4.3</b> 4.3.1 4.3.2 4.3.3 <b>4.4</b> 4.4.1	Surface fluxes  INITIAL CONDITIONS  Physical Constants  Microphysics  Simulation Parameters Summary  ANALYSIS METHODS  Temporal inversion height variation  Third moment of vertical velocity profile, < w <sup>13</sup> > Vertical statistical profile analysis.  DII-SERIES SIMULATIONS  DII_base	38 38 39 39 40 41 41 42 44 44
4.2.2 4.2.3 <b>4.3</b> 4.3.1 4.3.2 4.3.3 <b>4.4</b>	Surface fluxes.  INITIAL CONDITIONS	38 38 39 39 40 41 41 42 44 44 45

	4.4.4	DII fine	46
	4.4.5		
5.	RESUL	TS	48
	5.1	CLOUD COVER	49
	5.2	ASSESSMENT OF CLOUD STRUCTURE TRANSFORMATION	53
	5.3	PROFILE RESULTS	54
	5.3.1		
	5.3.2		
	5.5		
	5.6	THIRD MOMENT OF VERTICAL VELOCITY PROFILE STATISTIC, $\langle w'^3 \rangle$	67
6.	CONCI	USION	69
R	4.4.5Summary of DII-series simulations		
A]	PPENDE	X A	74
	Microph	ysics source code – Fortran 90	74
A]	PPENDE	Х В	79
A]	PPENDE	X C	80
A]	PPENDE	X D	83
	DII_base	e - Isometric view	83
	DII_base	e - Top view	86
	Kessler1	- Isometric view	89
	Kessler1	- Top view	92
A]	PPENDE	X E	95
	Kessler2	- Profile data	100

# LIST OF FIGURES

Figure 1: Isometric visualisation of base and sensitivity simulations	49
Figure 2: Cloud cover visualisation of base simulation	50
Figure 3: Cloud cover comparison between simulations	51
Figure 4: Cloud cover comparison at the end of the simulation	52
Figure 5: Statistical profiles of liquid water potential temperature	55
Figure 6: Micro-processes profile of base simulation – DII_base	56
Figure 7: Micro-processes profile of fine grid resolution simulation	57
Figure 8: Statistical profiles of the total water mixing ratio	58
Figure 9: Statistical profiles of the cloud liquid water mixing ratio	60
Figure 10: Micro-processes profile of sensitivity simulation – Kessler1	61
Figure 11: Cloud thickness, canopy and base comparison	64
Figure 12: Statistical profiles of relative humidity	65
Figure 13: Temporal inversion height variation	67
Figure 14: Third moment of vertical velocity profile	68
LIST OF TABLES	
Table 1: PUFFIN-ABL Cartesian grid domain values	36
Table 2: Surface flux boundary conditions	37
Table 3: Base simulation parameters summary	40
Table 4: Summary of DII-series simulations	47

# **ACKNOWLEDGEMENTS**

I would like to acknowledge with sincere gratitude, the support and guidance provided by my supervisor Dr. Michael Kirkpatrick over the past year to see the completion of this thesis paper.

I would also like to thank my family for always being ready provide support and encouragement whenever it was needed and for all the sacrifices they made for me.

# ABSTRACT

The simulation of a nocturnal marine boundary layer is conducted with the objective of integrating a fast and reliable cloud microphysics scheme into the PUFFIN-ABL computational fluid dynamics program (Kirkpatrick, 2008), expanding its current capabilities as a micro-scale atmospheric boundary layer (ABL) research platform to adequately simulate cloud micro-processes.

The implementation is conducted using the cloud microphysics scheme proposed by Wyant et al (1997). A single moment bulk microphysics parameterization is used and establishes the groundwork for the development of more accurate ABL simulations within PUFFIN. Without the presence of daytime radiative forcings, only a nocturnal marine cloud-topped boundary layer is simulated.

The model is tested and validated using initial and boundary conditions found in Stevens et al. (2004) and from the DYCOMS-II research flight data. A simple long-wave radiation parameterisation proposed by Stevens et al. (2004) is also implemented into PUFFIN-ABL to ensure that the results can be reliably compared to the DYCOMS-II LES contributions. Sensitivities controlling autoconversion, radiative forcings and domain grid resolution are also tested. Concerns for the accuracy of the microphysics scheme are raised and the problem is identified to be an issue regarding the implementation of the microphysics scheme into PUFFIN-ABL. The results indicate that the model can successfully simulate clouds and with some modifications, has the potential to yield results reliable enough for atmospheric and climate research.

# 1. Introduction

The modeling of cloud micro-processes has become vital in the understanding of global climate change because of the obvious interaction between aerosols, clouds and radiation. As addressed by Smagorinsky (1978), Liou and Ou (1989) and Ackerman et al. (2004) amongst others, there is still considerable uncertainty regarding the actual feedback effect on climate change as a result of cloud cover and the solar cloud albedo. In line with this research, much progress has been made in the development of cloud microphysics schemes using various parameterization methods.

Single moment bulk microphysics schemes devised by authors such as Kessler (1969) and Wyant et al. (1997) have been credited in comparative research papers for successfully driving simulations of the main features of cloud systems yet fall short in completely describing the aerosol-cloud microphysical interactions that are necessary for more accurate predictions of mesoscale quantitative precipitation forecasts (QPF) as highlighted by Seifert et al. (2005). On the other hand, the recent wave of research in the field of spectral bin microphysics schemes has generated significant improvement in the accuracy of cloud microphysics simulations; but this brings into question the actual necessity for such precise models when at present, macro-scale geophysical processes such as cloud top entrainment are still not accurately simulated. Nevertheless, the resources required to process the large number of variables within bin microphysics models places restraint on the current research to basic levels only.

Two moment bulk microphysics schemes such as those proposed by Cotton et al. (1986) and Reisner et al. (1998), provide a balance between the complexity and computing cost of the bin microphysics models and the lack of sufficient data made available from single moment bulk scheme simulations. The two-moment bulk models appear to be the most computationally efficient available for mesoscale forecasts, however taking into consideration time constraints and for the scope of this report, the

microphysical scheme proposed by Wyant et al. (1997) will be simulated and analysed, irrespective of the apparent deficiencies of single moment bulk schemes for mesoscale QPFs; the justification for this will be addressed within the coming paragraphs.

The purpose of this thesis is to integrate a fast and reliable cloud microphysics scheme into the PUFFIN-ABL computational fluid dynamics (CFD) program (Kirkpatrick, 2008), expanding its current capabilities as a micro-scale atmospheric boundary layer (ABL) research platform to adequately simulate cloud micro-processes. There will also be suggestions made regarding further enhancements to the microphysics models currently integrated within PUFFIN-ABL to further improve simulation accuracy; modifications such as the addition of a second moment to the current single moment scheme that could be used to describe aerosol effects as discussed by Seifert et al. (2005). Another necessary enhancement that will be described is the integration of a simple radiation scheme that is necessary to readily model shortwave and long-wave heating and cooling effects on cloud microphysics, on the cloud canopy and below the cloud. A radiation model coupled with a two-moment microphysics scheme within PUFFIN-ABL could be a powerful research tool for the micro-scale analysis of the effects of aerosols and cloud condensation nuclei on the ABL.

The single moment bulk microphysics parameterization used in this report establishes the groundwork for the development of more accurate ABL simulations within PUFFIN. Without presence of daytime radiative forcings however, only a nocturnal marine cloud-topped boundary layer (MNBL) has been simulated; this is sufficient for the analysis of the model proposed in Wyant et al. (1997) since it is only the first attempt at identifying a suitable cloud model to be used for the PUFFIN-ABL simulations. The proposed model attempts to simulate the weather conditions observed during the DYCOMS-II research flights and the initial conditions for the simulations are

based on data used by Stevens et al. (2004) from the atmospheric readings obtained during the research flights. Analyses of results obtained from PUFFIN-ABL output data will then allow an appraisal of Wyant's (1995) cloud microphysics parameterizations in nocturnal marine conditions and its suitability for further research using the PUFFIN-ABL platform.

Since PUFFIN-ABL adopts a large eddy simulation (LES) approach for simulating the ABL, the suitability of the cloud model proposed by Wyant et al. (1997) for the purposes of our research is attributable to the following factors. First, the proposed cloud microphysics model was tested by Wyant et al. using two and three dimensional (2D, 3D) eddy resolving models (ERMs); LES is by definition a subset of eddy resolving models. The success of the simulation by Wyant et al. using their cloud scheme within an ERM framework in modeling the marine stratocumulus to trade cumulus transition establishes support for the application of the cloud microphysics scheme to the PUFFIN-ABL 3D LES model. Secondly, the simulation by Wyant et al. is conducted under diurnal marine conditions to simulate the stratocumulus to trade cumulus transition. Our simulation of the nocturnal marine stratocumulus topped ABL falls within the conditions that Wyant et al. use for their analysis. Essentially, the proposed microphysics model has seen considerable validation within an ERM in the Wyant et al. (1997) paper and this suffices as grounds for using their cloud model.

The initial conditions and validation of the results are based on and conducted with the DYCOMS-II field research data. The DYCOMS-II field experiment was conducted off the subtropical east coast of San Diego, USA. Seven of the nine research flights took place were nocturnal and well formed summertime stratocumulus clouds were observed. The cloud cover was described as solid, unbroken stratus in eight of the nine flights and the outlier was deemed a near solid stratus with occasional breaks. The focus in this paper is on the formation of summertime stratocumulus clouds as observed

in DYCOMS-II; similar more advanced analyses have been conducted by Stevens et al. (2004). Stratocumulus clouds typically form over subtropical oceans off the west coasts of the major continents and develop due to a strong subsidence over a cold ocean surface. The cooler temperatures and large subsidence act to create large static stability. This kind of stability is a precondition necessary for the formation of marine stratocumulus. These marine cloud formations extend over thousands of square kilometers with thicknesses ranging from approximately 100-500m.

The structure of this thesis is as follows. Section 2 provides an in depth discussion of the historical and current research in the field of cloud microphysics. In section 3, a description of the cloud microphysics and radiation schemes used for the simulations is provided. In section 4 we outline the relevant initial and boundary conditions, the PUFFIN-ABL domain and introduce the base and sensitivity simulations along with the diagnostic statistics and analysis methods used to interpret results generated by the simulations. We present our results and findings in Section 5 comparing the base and sensitivity simulations with the results presented in Stevens et al. (2004) and with the DYCOMS-II recorded field research data. Section 6 concludes on the findings from the results, discusses the reliability of the chosen microphysics and radiation schemes, addresses the concerns raised during the analysis of results and presents possible solutions and recommendations regarding the models used for this thesis and for future research.

# 2. LITERATURE REVIEW

A major proponent of cloud modelling in the late 1950's was the US Defense Force. The ambition was to gain a deeper understanding of cloud autoconversion, accretion, evaporation and entrainment processes in modelling the distribution of water vapour, cloud and precipitation in tropical climates. The directive to emphasize research in tropical climates was purely because the US government at the time was focusing attention to Vietnam; a tropical country with heavy rainfall (Kessler et al., 1963).

In terms of atmospheric modelling, the first numerical technique modelling an isolated dry thermal was conducted by Malkus and Witt (1959), further experimentation conducted by Ogura and Phillips (1962) introduced developments that included a scale analysis to derive basic equations for shallow and deep atmospheric convections. Ogura (1963) conducted an investigation of axially-symmetric convective circulation generated by latent heat in a conditionally unstable atmosphere and Orville (1965) added the effects of water vapour to the basic equations of Ogura and applied the results to the development of cumulus clouds in mountainous terrain.

Research on precipitation processes had not previously been undertaken and it was Das (1964) who developed a one dimensional simulation for the downdraft that forms due to the drag of falling raindrops. Takeda (1966) first incorporated precipitation in a two dimensional model including the effects of evaporation; with this model, rainwater evaporated immediately to maintain saturation in the air. The microphysical terms of autoconversion, accretion and evaporation were introduced by Srivastava (1967) with a simple method for computing raindrop mean terminal velocity; the raindrops represented by the Marshall-Palmer raindrop distribution (Marshall and Palmer 1948, Liu and Orville 1969).

### 2.1 Early microphysics parameterisations

The early microphysical parameterisations introduced by Kessler (1969) were simplistic in nature but will be discussed in detail. Two transport equations are used by Kessler (1969) to deal with both precipitation and cloud motion. One equation allows the cloud to share the same motion as air and the other allows for precipitation. In one analysis by Kessler, cloud motion was left out to illustrate the simple case where evaporation is immediately applied to precipitation; in the scheme that will be thoroughly analysed in this thesis, evaporation is applied to regions in the boundary layer where relative humidity is less than unity. This greatly simplifies the model at the cost of only a minor loss in the accuracy of the simulations.

The transport equations used by Kessler (1969) account for local rate of change of precipitation and cloud, their horizontal and vertical advection, divergence associated with the vertical motion in the compressible atmosphere, condensation and evaporation of cloud and changes of the saturation deficit that accompany vertical motion of air and microphysical processes which include autoconversion, accretion, and evaporation of precipitation. Autoconversion can be understood as an increase in the rainwater mixing ratio from changes in the cloud liquid water mixing ratio caused by collisions of cloud water drops; accretion can be interpreted as the collection of cloud water drops by rainwater drops (Wyant et al., 1996).

#### 2.1.1 Autoconversion

The autoconversion process portrayed by Kessler (1969) assumes that to a certain threshold, clouds are stable, and beyond that threshold a fraction of the cloud changes to rain per unit of time:

$$Autoconversion = k_1(m-a)^+.$$
 (L1)

Here the plus sign indicates that  $k_1$  must be zero until m > a, where m is the cloud liquid water ratio and a is a threshold constant determined empirically. This method provides no physical insight into how autoconversion occurs but allows for the analysis of various thresholds and autoconversion rates with high computational efficiency. Furthermore, given an accurate threshold constant, a, reliable autoconversion rates can always be computed. The parameterisation of autoconversion (AC) is then used as an additive term within the precipitation transport equation (T2) and subtractive in the cloud transport equations (T1).

$$\frac{\partial m}{\partial t} = -u \frac{\partial m}{\partial x} - v \frac{\partial m}{\partial y} - w \frac{\partial m}{\partial z} + wG + mw \frac{\partial \ln \rho}{\partial z} - AC - CC + EP$$
 (T1)

$$\frac{\partial M}{\partial t} = -u \frac{\partial M}{\partial x} - v \frac{\partial M}{\partial y} - (V + w) \frac{\partial M}{\partial z} - M \frac{\partial V}{\partial z} + M w \frac{\partial \ln \rho}{\partial z} + AC + CC - EP$$
 (T2)

Kessler (1969) indicates that the model is simple; however it does not appear to be greatly different to the alternative suggested by a colleague that computes cloud autoconversion as a function of the fall speed of a cloud particle and the number of particles. In the previous approach, Kessler (1969) further describes that despite the deficiencies of the simple model for autoconversion, it still provided valuable insights into the kinematic relationships and conservation laws governing wind and water distributions and their relations to the strengths of microphysical processes.

### 2.1.2 Accretion

The accretion process modelled in Kessler (1969) occurs when slow moving cloud particles are collected by the larger precipitation particles as they fall. The process is modelled using the inverse exponential distribution of precipitation of Marshall and

Palmer (1948), where they fit experimental observations to a relation that expresses the rainwater drop size distribution as an inverse exponential function of diameter:

$$N_D = N_0 \exp(-\lambda D) \tag{L2-a}$$

$$\lambda = 41R^{-0.21}cm^{-1}$$
, (L2-b)

here D is the diameter and  $N_0 = 0.08 \text{ cm}^{-4}$  (found empirically) is the value of  $N_D$  when D = 0; this holds for any intensity of rainfall expressed in the equation (L2-b) where R is the rate of rainfall in mm hr<sup>-1</sup>.

The derivation of the accretion rate by Kessler (1969) is conducted by first determining the rate at which cloud is accumulated by a single precipitation particle of a particular diameter, falling at a certain velocity and collecting cloud particles with a given collection efficiency. Next the accretion rate for a precipitation packet is determined by substituting the velocity term with a velocity relation determined by Spilhaus (1948). Finally, the accretion rate for a precipitation packet is multiplied with the Marshall-Palmer distribution and integrated over all diameters to establish the equation for accretion. Kessler (1969) identifies that a more accurate representation of accretion would include effects of the variation of air density with altitude. With this, particles would fall faster at higher altitudes and hence would require the addition of an exponential term that is a function of height and density as multiplier. The accretion term is added to the rate of change of precipitation and is a negative contributor to the rate of change of cloud transport equations.

#### 2.1.3 Evaporation

Evaporation of rain is another aspect that deserves some attention because it contributes to the water budget. Kessler (1969) derives the evaporation model in a

similar fashion to the accretion equation using an expression provided by Kinzer and Gunn (1951).

$$dM/dt_{\text{evaporation}} = 1.93 * 10^{-6} N_0^{7/20} m M^{13/20} \text{ (gm}^{-3} \text{s}^{-1})$$
 (T3)

Here, evaporation is a function of precipitation, M, and the cloud content, m, and can only be considered a crude approximation.

The fall velocity, V, of rain as described in Kessler (1969) moves away from previous models which assumed a constant V over space and time. The approach adopted describes the variation of V with actual precipitation. The fall velocity is taken to be the terminal velocity of the median raindrop on the Marshall-Palmer distribution; this can be further augmented with the exponential term that is a function of height and density to account for changes in V as a result of variation in the air density with altitude.

#### 2.1.4 Implications of early microphysics parameterisations

The implications of the microphysics used by Kessler (1969) are also worthy of discussion. The time taken for the onset of precipitation can be decreased by increasing autoconversion and/or accretion however the influence of one diminishes if the other microphysical factor becomes relatively larger. The model proposed by Kessler for autoconversion could be delayed indefinitely by forcing the coefficient of the equation to remain at zero or by setting the threshold level higher than the level at which cloud is created in rising air currents; simply allowing a greater degree of control over the simulation. More significantly, the autoconversion parameterization proposed by Kessler (1969) is also used in the control simulation by Thompson et al. (2004). The equation incorporates the Heaviside function, H, cloud liquid water ratio q<sub>1</sub> and three threshold values determined empirically:

$$\frac{dq_r}{dt} = aH(q_l - q_{co}) \tag{L3}$$

where  $q_{co} = [0.35, 0.1, 0.5] \times 10^{-3}$  and  $a = 1 \times 10^{-3} \text{ s}^{-1}$  is a time constant.

The apparent simplicity of Kessler's autoconversion parameterization used by Thompson et al. would be useful for reducing the time and cost associated with the execution of simulations; the reliability is also considerably improved if a chosen threshold value holds true empirically. We assume that the threshold value of  $q_{co} = 0.35$  is a suitable value, based on the Thompson et al. (2004) paper.

## 2.2 Further development of microphysics schemes

To follow chronological development of bulk microphysical parameterisations leading to the cloud model proposed by Wyant et al. (1997), there will be some discussion on Liou and Ou (1989). A key change in the purpose of research in the field of geophysics becomes apparent with the focus shifting from military applications to climate modelling.

Liou and Ou analysed the issues facing global climate models and the validity of suggestions that increased greenhouse gases, namely carbon dioxide, actually exert a cooling effect on the climate rather than a warming effect because of increases in the formation of low clouds due to higher CCN concentrations. The cloud model incorporates a comprehensive parameterisation of condensation, accretion, autoconversion and precipitation evaporation; the condensation will be excluded until later in this report in order to draw comparisons across a number of research papers.

### 2.2.1 Autoconversion and accretion processes based on collision theory

Liou and Ou (1989) derive an autoconversion rate,  $P_1$ , from the collision theory, which defines precipitation generation as a linear function of the mean collision

efficiency,  $\overline{E}$ , droplet concentration, N, and the cloud liquid water mixing ratio,  $q_l$ , but is dependent on the mean droplet radius to the fourth power,  $\overline{r}_w^4$ .

$$P_1 = \pi \overline{E} k N \overline{r}_w^4 q_I. \tag{T4}$$

This shows that any slight change in the mean droplet radius would have a significant effect on the autoconversion rate. Stokes law is utilised as the governing equation for the fall velocity of the droplets for droplet radii below 50 micrometers; here fall velocity is proportional to the square of the droplet radius with a constant of proportionality from Rogers (1979). The mean droplet radius is computed from the integral of the rainwater droplet distribution; the distribution used is based on the Marshall-Palmer distribution which approximates the raindrop size distribution to a negative exponential (Marshall and Palmer 1948). Liou and Ou (1989) use the same intercept parameter as Marshall and Palmer (1948) for approximating the rainwater distribution; this is valid if the rainfall rate is below 1mm per hour and hence a key assumption is made regarding the precipitation rate in order to compute the autoconversion rate.

#### 2.2.2 Accretion based on collision theory

The next stage of precipitation is accretion,  $P_2$ , where Liou and Ou (1989) again use the Marshall-Palmer distribution for raindrop size distribution. The raindrop generation in the one-dimensional model is 0.5mm per hour within the cloudy region and thus the intercept parameter used by Marshall and Palmer (1948) would still be valid; the raindrop fall velocity however is computed through the form devised by Liu and Orville (1969). The accretion rate then becomes a function of air density, precipitation flux,  $\overline{P}$ , and the cloud liquid water mixing ratio,  $q_l$ ; the precipitation flux itself being a function of density,  $\rho$ , the rainwater mixing ratio,  $q_r$ , and the bulk terminal velocity of raindrops,  $\overline{w}_r$ .

$$P_2 = k_2 \overline{P}^{0.791} q_l \tag{T5}$$

where  $k_2 = 0.931 \rho^{-0.105}$  and  $\overline{P} = \rho \overline{w}_r q_r$ .

The total rate of precipitation generation, P, essentially becomes the addition of the autoconversion and accretion terms and is similar to that derived by Kessler (1969),

$$P = P_1(autoconversion) + P_2(accretion)$$
 (T6)

with the key difference being that the autoconversion rate is a function of the mean radius to the fourth power in the parameterisation proposed by Liou and Ou (1989).

### 2.2.3 Evaporation

The evaporation rate is also important when considering the water budget and we assume it to be a negligible term only within the cloudy region (Sundqvist, 1978). Liou and Ou (1989) model the effect of evaporation during the precipitation process (beyond the cloudy regions) analogous to the parameterisation of the condensation rate with an additional ventilation factor. The ventilation factor provided by Beard and Pruppacher (1979) is a function of the viscosity of air, the Schmidt number and air density. Again utilising the Marshall-Palmer raindrop size distribution and ventilation factor, the evaporation rate is expressed by Liou and Ou (1989) to be a function of temperature, relative humidity, saturation vapour pressure, air density and the precipitation flux.

The treatment of condensation by Liou and Ou is significantly more comprehensive than that by Wyant et al. (1997) simply because they calculate the rate of condensation explicitly, rather than basing condensation formation solely on the cloud liquid water mixing ratio having a non-zero value only if the total water mixing ratio (TWMR) is greater than the saturation vapour mixing ratio.

The condensation rate equation proposed by Liou and Ou (1989) is derived on the basis of the steady state, one dimensional diffusion theory for water vapour and latent heat transports.

$$Q_c = k_c (q_c / q_s - 1) \tag{T7-a}$$

The expression is a function of a condensation rate coefficient and the relative humidity,  $q_c/q_s$ , within the cloudy region. The condensation rate coefficient is formulated from an equation which is a function of the mean droplet radius,  $\bar{r}_a$ , the number concentration of cloud droplets, N, the air density,  $\rho$ , temperature, T, and the saturation vapour pressure,  $e_s(T)$ ,

$$k_c = 4\pi \overline{r_a} N / \rho (A + B)$$

$$A = L^2 / (R_v K T^2) \qquad B = R_v T / De_s (T)$$
(T7-b)

where L is the latent heat of vaporisation,  $R_v$  is the gas constant for water vapour, D is the mass diffusion coefficient for water vapour in air and K is the thermal diffusivity.

As temperature increases, it has a positive effect on the condensation rate coefficient; since the evaporation rate coefficients are also a function of temperature; the effects of radiative forcings are reflected in changes in evaporation and condensation rates. This also results in a great deal of interaction between condensation and evaporation rates with thermodynamic equations that contain temperature and thermal infrared (IR) fluxes.

## 2.3 Single moment bulk microphysics scheme

Wyant et al. (1997) utilise bulk microphysical parameterisations for the development of rain within their simulation again taking into consideration autoconversion, accretion and evaporation rates. The rainwater is generated through autoconversion and accretion and can evaporate in subsaturated air. Here the

microphysical process associated with atmospheric total water mixing ratio defines the accretion rate,  $P_2$ , and autoconversion rate,  $P_1$ , as negative contributors and the evaporation rate, E, as a positive contributor to the total water mixing ratio.

$$\left(\frac{\partial q_t}{\partial t}\right) = -\left(P_1 + P_2 - E\right) \tag{T8}$$

Conversely, the microphysical component to the atmospheric rainwater mixing ratio defines autoconversion and accretion as positive contributors and evaporation as having a negative feedback; an additional differential term is also included to parameterise change in rainwater flux,  $F_p$ , over height identifying the downward flux of precipitation out of the grid cell.

$$\left(\frac{\partial q_r}{\partial t}\right) = P_1 + P_2 - E - \frac{1}{\overline{\rho}} \frac{\partial F_p}{\partial z}$$
 (T9)

The microphysical parameterisation for the liquid water potential temperature rate is defined as the evaporation rate subtracted from the sum of the accretion and autoconversion rates, multiplied by the latent heat of vapourisation, the constant pressure specific heat of dry air and the environment perturbation as the denominator

$$\left(\frac{\partial \theta_l}{\partial t}\right) = \frac{L}{C_p \Pi_{env}} (P_1 + P_2 - E) \tag{T10}$$

where L is the latent heat of vaporisation,  $C_p$  is constant pressure specific heat of dry air and  $\Pi_{env}$  is the Exner function.

#### 2.3.1 Autoconversion

The autoconversion rate proposed by Wyant et al. (1997) is based on the collision theory derived from Liou and Ou (1989), with the assumption that cloud water drops are stationary.

$$P_1 = \pi \alpha \overline{E}_1 C_1 N \overline{r}_w^4 q_l \tag{T11}$$

Here the rate of precipitation generation due to autoconversion is a function of the cloud liquid water mixing ratio,  $q_l$ , mean droplet radius,  $\bar{r}_w^4$ , the terminal fall speed of a drop of a given radius given by  $C_1 r^2$ ; the cloud droplet concentration, N, and mean autoconversion efficiency,  $\bar{E}_1$ .

A critical assumption is made in this model, that cloud condensation nuclei (CCN) below a fixed supersaturation are activated in cloud at one to a drop, hence the number concentration N, is assumed to be equal to the CCN. They also note that a factor of eight increase in CCN concentration would halve the autoconversion rate; which is indicative that there is a very strong dependence of autoconversion on CCN concentration. This has important implications since Seifert et al. (2006) underpin the significance of bin cloud microphysics by identifying that aerosol particles acting as CCN cause the formation of different cloud types due to their different characteristics in size, distribution and chemical composition.

Wyant et al. (1997) may have oversimplified the process of autoconversion for the scope of modelling the stratocumulus to trade cumulus transition. The mean droplet radius (also referred to as the fourth moment drop radius) is fixed by Liou and Ou (1989), but is estimated from the cloud liquid water mixing ratio,  $q_i$ , in line with the selected method preferred by Chen and Cotton (1987) and Baker (1993).

$$\bar{r}_{w} = \left(\frac{1}{N} \frac{3}{4\pi} \frac{\bar{\rho}}{\rho_{l}} q_{l}\right)^{1/3} \tag{T12}$$

Wyant et al. (1997) moderate the original computed autoconversion rate following Baker (1993) and Austin et al. (1995) after they identify that the original rates are too high in comparison to better microphysical schemes. To do this a multiplicative constant,  $\alpha$ , is applied to ensure that the rate is reduced to levels obtained from other more accurate sources.

### 2.3.2 Accretion

The parameterisation of accretion by Wyant et al. (1997) utilises the assumption that cloud water drops are stationary. The accretion rate is based on the cloud liquid water mixing ratio,  $q_l$ , the precipitation flux,  $F_p$ , and the mass weighted drop radius,  $r_m$ , derived from a Marshall-Palmer type drop size distribution following Liou and Ou (1989),

$$P_2 = -\frac{3}{16} \frac{\overline{E}_2 \times F_p \times q_l}{\rho_l r_m} \tag{T13}$$

$$r_m = \left(\frac{\bar{\rho}q_r}{8\pi\rho_1 n_0}\right)^{1/4} \tag{T14}$$

where  $\overline{E}_2$  is the collision efficiency,  $\rho_l$  is the density of liquid water (1000 kg.m<sup>-3</sup>) and  $\overline{\rho}$  is the anelestic base state density.

The rainwater droplet distribution is assumed to follow the general relation obtained by Marshall and Palmer (1948). The mass weighted drop radius, a vital parameter for the calculation of the accretion rate, is solved through the integration of the modified Marshall-Palmer distribution. Another key parameter for calculating the accretion rate is the precipitation flux, which is a function of the rainwater mixing ratio,  $q_r$ , the mass weighted drop radius,  $r_m$ , and the fall speed parameterisation,  $C_2$ , given by Rogers and Yau (1989).

$$F_p = -4\overline{\rho}C_2 r_m q_r \tag{T15}$$

The precipitation flux is calculated by integrating the rainwater fall speed over the Marshall-Palmer type drop size distribution. Wyant et al. (1997) also use the differential of the precipitation flux over height to calculate the rainwater mixing ratio.

### 2.3.3 Evaporation

The evaporation rate computed by Wyant et al. (1997) is a function of the mass weighted drop radius, relative humidity, temperature and saturation vapour pressure; a relation derived from the droplet evaporation expression presented by Rogers and Yau (1989).

## 2.4 Comparison of current microphysics schemes

Over the past four decades there have been significant advancements in cloud models from the early dry convection to the modern bin microphysics; with this there has been an increase in the sophistication of the models representing the physical processes of turbulence, microphysics, radiation and surface fluxes (Costa et al. 2000). The current progress in the development of bulk microphysics schemes has been paralleled with research into two-moment microphysics models and bin microphysics parameterisations in an attempt to further refine the simulations

#### 2.4.1 Single-moment bulk microphysics models

Bulk microphysics parameterisations such as those proposed by Kessler (1969) are based on the prediction of liquid contents of only a small number of hydrometeor classes; parameterisations which can be classified as a one-moment scheme. The majority of earlier microphysics parameterisations were based on predictions of a single moment of the hydrometeor size-spectra, namely, the mass mixing ratio of the species (Walko et al., 1995).

Previous research using bulk microphysics schemes have yielded accurate results however those models used did not carry sufficient information regarding the size or number of cloud droplets and could not simulate aerosol-cloud effects

effectively; there are also suggestions that bulk microphysics parameterisations would not be able to achieve accurate mesoscale atmospheric models (Seifert et al., 2006).

## 2.4.2 Two-Moment bulk microphysics models

More recently, there has been a change to extend those earlier bulk microphysics schemes to include predictions on an additional moment of the spectrum. This can include the distribution of the number concentration of the liquid and ice hydrometeor species (hydrometeors being any water based species that can gravitationally settle) and can even include the distribution in the concentration of CCN. This slight deviation from the simple single-moment parameterisations, are classified as two-moment microphysics schemes that use the traditional mass mixing ratio variables and introduce the number concentrations of the liquid and ice hydrometeors or CCN concentrations.

### 2.4.3 Bin microphysics schemes

Regarding the more experimental bin microphysics schemes, an added level of complexity is presented by the spectral bin microphysics models which develop predictions of the spacio-temporal behaviour of a number of size categories for each type of hydrometeor; these models consider CCN as part of the aerosol distributions which cause droplets to form. Simply put, bin microphysics represents drop size and CCN with "bins" based on their size distributions; these bins containing information about cloud drop sizes and CCN sizes then interact with one another based on their size related properties. There is an inherent requirement for the computation of a very large number of variables; accordingly, there is also a greater cost associated with preparing regional climate models or quantitative precipitation forecasts and that is why the use of bin microphysical models is currently limited to basic research only (Seifert et al., 2006).

Khairoutdinov and Kogan (1999) employed a bin microphysics framework to simulate a stratocumulus boundary layer model originally designed for a cumulus cloud model developed by Kogan (1991). Within the model, two drop size distribution functions are used to represent the microphysical processes; one for cloud drops and the other for cloud condensation nuclei (CCN).

$$\frac{\partial n}{\partial t} + \frac{\partial}{\partial x_j} (u_j n) = -\left[\frac{\partial n}{\partial t}\right]_{\text{nucl}} + \frac{\partial}{\partial x_j} \left(K_m \frac{\partial n}{\partial x_j}\right)$$
(T16)

The first function (Eq. T16) specifies the size distribution of the condensation nuclei, n, and can be used to define the number of CCN per unit volume at a point with radii within the range r and r + dr. Here the  $\left[\frac{\partial n}{\partial t}\right]_{nucl}$  term describes the loss of CCN by activation; where activation is the process that describes the formation of a cloud droplet.

The second function (Eq. T17) is used to represent the cloud drop mass distribution where the function defines the number of cloud drops at a particular point with a mass within the range m and m + dm:

$$\frac{\partial f}{\partial t} + \frac{\partial}{\partial x_{j}} \left[ (u_{j} - V(m)\delta_{j3})f \right] = \left[ \frac{\partial f}{\partial t} \right]_{\text{nucl}} + \left[ \frac{\partial f}{\partial t} \right]_{\text{cond}} + \left[ \frac{\partial f}{\partial t} \right]_{\text{col}} + \left[ \frac{\partial f}{\partial t} \right]_{\text{br}} + \frac{\partial}{\partial x_{j}} \left( K_{m} \frac{\partial f}{\partial x_{j}} \right)$$
(T17)

where V(m) is the fall velocity of drops with mass, m. Here the microphysical effects (denoted by subscripts) of nucleation (nucl), condensation/evaporation (cond), coalescence (col) and break-up (br) are added to the drop mass distribution function; this equation describes the advective and turbulent transport taking place for each drop mass in the range m and m + dm. The drop size distribution is represented by 29 bins logarithmically spaced in a range from 1 to 645 micrometers; the CCN size spectrum is resolved in the range from 0.0076 to 7.6 micrometers, varying within 8 to 19 bins. In

this particular model, there is the expectation that the drop sizes represented are sufficient to study a drizzling stratocumulus boundary layer.

One issue presented by the increased level of sophistication with the modelling of CCN is that since there is very little known about CCN processing within clouds, long simulations would begin to affect the spectrum shape and total CCN number. This is attributable to the decrease in the number of CCN due to washout by drizzle even after CCN spectra are returned to their original shape after cloud drop evaporation (Khairoutdinov and Kogan, 1999).

The CCN distribution function as used by Kogan (1991) comprises of a term that accounts for the loss of condensation nuclei after activation when supersaturation is greater than the critical value and a term that identifies the change of the size distribution of CCN due to turbulent transport. The drop distribution function is represented by an equation that includes terms for advective and turbulent transport and accounts for changes caused by nucleation, condensation/evaporation, coalescence and break-up. Nucleation is described to take place when cloud condensation nuclei are activated at each spatial point as soon as the supersaturation exceeds a critical value determined using the Kohler equation; a relation that equates supersaturation, S, to the radius of the dry salt nucleus,  $r_n$ , the cloud droplet radius, r, the density,  $\rho_{w,n}$ , and molecular mass,  $M_{w,n}$ , of water and the dry salt nucleus denoted by the subscripts w and n respectively.

$$S - \frac{2\sigma}{\rho_{w}R_{v}T} + \frac{2\rho_{n}M_{w}r_{n}^{3}}{\rho_{w}M_{n}r^{3}} = 0$$
 (T18)

Kogan (1991) defines the growth after activation of CCN as the droplet growth equation similar to one used by Mordy (1959),

$$\frac{dr}{dt} = \frac{D_{\nu}e_{s}(T)F_{\nu}}{\rho_{\nu}R_{\nu}T} \frac{\left(S - \frac{2\sigma}{\rho_{\nu}R_{\nu}Tr} + \frac{2\rho_{n}M_{\nu}r_{n}^{3}}{\rho_{\nu}M_{n}r^{3}}\right)}{\left(r + r*\right)\left(1 + \frac{D_{\nu}L^{2}e_{s}(T)}{KR_{\nu}T^{3}}\right)} 
r* = D_{\nu}/\alpha\sqrt{2\pi/R_{\nu}T} / 1 + \frac{D_{\nu}L^{2}e_{s}(T)}{KR_{\nu}T^{3}},$$
(T19)

where the growth rate is a function of the thermal conductivity of air, K, the Kohler equation (T18) and the diffusivity,  $D_v$ , saturation pressure,  $e_s(T)$  and the specific gas constant,  $R_v$ , of water vapour. The ventilation coefficient,  $F_v$ , is dependent on the Schmidt and Reynolds numbers and the  $r^*$  term is used here to account for gas kinetic effects on the diffusion coefficient for small droplets where  $\alpha$  is the condensation coefficient. The cloud droplet growth equation for condensation is taken in a form very similar to the growth rate during nucleation, however the relation is presented in a far more simplified format since accounting for the soluble material becomes unnecessary after the short time-span following activation. The coalescence and break-up terms are also of significance within the microphysics model proposed by Kogan (1991); here coalescence is taken as a stochastic coalescence equation which is based on the fall velocity of drops as a function of mass, drop radius and collision efficiency. The break-up term of cloud droplets is defined by Kogan as the probability of break-up for a drop of a particular mass per unit time and the number of drops formed due to the disintegration of one drop of a particular mass.

### 2.5 Radiation schemes

A second important component to atmospheric boundary layer simulations is the incorporation of a radiation model. Although the primary focus of this paper is the simulation and analysis of nocturnal marine stratocumulus clouds which greatly simplifies the complexity of the radiative forcings to longwave radiative cooling within

the model, it is worthwhile discussing daytime radiation schemes in order to establish the full potential of expandability of PUFFIN-ABL for more complex analyses in the future.

Considering only the application of radiation on bulk microphysics schemes, there is always the requirement to develop models that are both accurate yet efficient; with this, it is suggested that two stream radiation models are the best options. In order to couple two-stream radiation models to a microphysics model, there is also a requirement to efficiently compute cloud optical properties; cloud optical properties consisting of the single scatter albedo, the optical depth and the asymmetry parameter. The computation of the parameters must be done for each band of the radiative transfer model and are combined from values computed from each hydrometeor type (Harrington and Olsson, 2001).

#### 2.5.1 Two-stream and multi-band scheme comparison

According to Wyant et al (1996) in their selection of a radiation scheme, there is the suggestion that the overall radiative flux divergence through the cloud layer obtained from the two-stream scheme for both long wave and short wave radiation by Herman and Goody (1976) is in very close agreement to the detailed multi-band scheme proposed by Roach and Slingo (1979). Wyant et al. compute the transmissivites of water vapour and liquid water used in the two-steam scheme as a function of the vertical water vapour and liquid water paths respectively, disregarding pressure corrections. Slight adjustments are made from the Herman and Goody scheme in order to achieve heating rates that are in accordance with the Slinger and Schrecker (1982) scheme for stratocumulus clouds with the sun at zenith. Wyant et al. (1997) indicate that there is a preference to observe the effect of heating caused by radiation as opposed to study the

albedo; this is because heating has a direct effect on the cloud dynamics and was a major component of their paper.

## 2.5.2 Simple long wave radiation parameterisation

In this paper we adopt the simple radiation model proposed by Stevens et al. (2004) for the evaluation of large eddy simulations using the observations of nocturnal marine stratocumulus clouds from the DYCOMS-II research data. The  $\delta$ -four stream radiative code developed by Fu and Liou (1993) was parameterised by Stevens et al. and the simple long wave radiative model was then derived from the radiative flux profiles derived from the  $\delta$ -four stream model:

$$F_{rad}(x,y,z,t) = F_0 e^{-Q(z,\infty)} + F_1 e^{-Q(0,z)} + \rho_i c_p D\alpha_z \left[ \frac{(z-z_i)^{4/3}}{4} + z_i (z-z_i)^{1/3} \right] \tag{L4} \label{eq:L4}$$

here, Stevens et al. (2004) indicate that the parameterization was selected for ease of comparison however the model is still described as fairly accurate. The first term on the right hand side describes cooling per square meter at the cloud top; the second describes the cloud base warming per square meter and the third term is the cooling of the boundary layer above the inversion, from the height of the inversion to the top of the boundary layer.

# 3. MODEL DESCRIPTIONS

#### 3.1 Micro-processes involved in the microphysics

The microphysics model we have integrated into PUFFIN-ABL is the one adopted by Wyant et al. (1997); a hybrid of the schemes proposed by Liou and Ou (1989), Chen and Cotton (1987) and Baker (1993). This microphysics scheme can be broken down into the key components of autoconversion, accretion and evaporation. There is also the process of condensation which dictates the presence of clouds and is tantamount to the overall simulation. It is important to note that the cloud model used is a single moment bulk microphysics scheme; single moment because only a single moment within the hydrometeor size-spectra is used in the parameterisations, namely, the mass mixing ratio of the hydrometeor species. This single moment scheme disregards the variation in size or quantity of the cloud droplets. This is considered one of the shortfalls of single moment schemes for the purposes of mesoscale forecasts.

The microphysics parameterisations attach as partial time derivatives to the transport equations for the three scalar prognostic variables that govern the macro processes of the species in question. The transport equations describe the change in liquid water potential temperature, the total water mixing ratio and the rainwater mixing ratio. The microphysics source terms adjust the prognostic variables at each time step and allow the simulation of the cloud microphysics to occur. The transport equations are written:

$$\begin{split} & \frac{D\theta_{l}}{Dt} = -\frac{1}{\overline{\rho}C_{p}\Pi_{env}} \frac{\partial F_{R}}{\partial z} + \frac{1}{\overline{\rho}} \nabla \cdot \overline{\rho}K_{H} \nabla \theta_{l} + \left(\frac{\partial \theta_{l}}{\partial t}\right)_{microphysics} \\ & \frac{Dq_{t}}{Dt} = \frac{1}{\overline{\rho}} \nabla \cdot \overline{\rho}K_{Q} \nabla q_{t} + \left(\frac{\partial q_{t}}{\partial t}\right)_{microphysics} \\ & \frac{Dq_{r}}{Dt} = \frac{1}{\overline{\rho}} \nabla \cdot \overline{\rho}K_{Q} \nabla q_{r} + \left(\frac{\partial q_{r}}{\partial t}\right)_{microphysics} \end{split} \tag{1}$$

where  $\theta_l$  is the liquid water potential temperature,  $q_t$  is the total water mixing ratio and  $q_r$  is the rain-water mixing ratio. The three microphysics source terms contain parameterisations for the four processes: condensation, autoconversion, accretion and evaporation.

#### 3.1.1 Condensation

Condensation is the process of cloud formation. Within this microphysics scheme, the cloud liquid water mixing ratio identifies the presence of clouds within the boundary layer. Based on the simple formula below, condensation occurs when the total water mixing ratio is greater than the saturation vapour mixing ratio:

$$q_l = \langle q_t - q_{sat}(T, p_{env}) \rangle^+ \tag{2}$$

the  $^+$  sign denoting a zero value for all negative  $q_l$ , where  $q_l$  is the cloud liquid water mixing ratio and  $q_{sat}$  is the saturation vapour mixing ratio. To calculate the cloud liquid water ratio, the saturation vapour mixing ratio must also be determined and is done so by Wyant et al. using the following approximations:

$$e_{s}(T) = e_{0} \exp \left[ -\frac{L}{R_{v}} \left( \frac{1}{T} - \frac{1}{T_{0}} \right) \right]$$

$$q_{sat} = \frac{R_{d}}{R_{v}} \frac{e_{s}(T)}{p}$$
(3)

where T is the temperature,  $L = 2.5 \times 10^6 \text{ J.kg}^{-1}$  is the specific heat of vaporisation at 273.16K,  $R_v = 461.0 \text{ J kg}^{-1} \text{ K}^{-1}$  is the gas constant for water vapour,  $R_d$  is the ideal gas constant, p is the pressure,  $e_o = 610.78 \text{ Pa}$  and  $T_0 = 273.16 \text{ K}$ .

It is important to address the advantages and limitations of the cloud liquid water mixing ratio parameterisation proposed by Wyant et al. This is arguably a very simple method of determining the cloud liquid water mixing ratio that greatly improves the speed and efficiency of the microphysics simulations at the cost of some accuracy. This parameterisation flows on through the entire microphysics scheme and acts as a proxy for the presence of clouds; hence the simple nature of this condensation function may generate erroneous results via a deviation from actual geophysical processes during the simulation of the ABL with the microphysics scheme.

#### 3.1.2 Autoconversion

Autoconversion is the process by which rainwater is created through the collisions between cloud water drops. As such, the parameterisation used to determine the rate of autoconversion (5) is derived from collision theory (4):

$$P = q_1 \overline{E}_1 \int \pi r^2 V(r) n(r) dr \tag{4}$$

$$P = \pi \overline{E}_1 C_1 N \overline{r}_w^4 q_I \tag{5}$$

where  $\overline{E} = 0.55$  is the mean autoconversion efficiency parameter, N, the integral of n(r) is approximated as the total cloud water drop concentration,  $\overline{r}_w$  is the fourth moment drop radius (the kurtosis of the distribution of cloud drops). The velocity term, V(r) within the integral is the fall speed parameterisation given by Rogers and Yau (1989):

$$V = C_1 r^2 \qquad r < 40 \mu m$$

$$V = C_2 r \qquad r \ge 40 \mu m$$
(6)

$$C_1 = 1.19 \times 10^8 \,\text{m}^{-1} \,\text{s}^{-1}$$
 and  $C_2 = 8.0 \times 10^3 \,\text{s}^{-1}$ 

For the autoconversion parameterisation, the relevant velocity function is for a drop radius less than 40 $\mu$ m; hence the use of the  $C_1$  term in the parameterisation. The fourth moment drop radius is assumed to vary with the cloud liquid water mixing ratio as proposed by Chen and Cotton (1987) and Baker (1993):

$$\bar{r}_{w} = \left(\frac{1}{N} \frac{3}{4\pi} \frac{\bar{\rho}}{\rho_{l}} q_{l}\right)^{1/3},\tag{7}$$

where  $\bar{\rho}$  is the anelastic base state density variable and  $\rho_l$  is the density of liquid water. As we can see here, this fourth moment distribution function is not based on a

statistical distribution, but an approximation based on the cloud liquid water mixing ratio. This here is another approximation which further reduces the accuracy of the microphysics scheme; the extent to which remains ambiguous within this report but is a testable parameterisation in later research.

An important generalisation made in the autoconversion parameterisation is that the number concentration of cloud particles, N, equals the concentration of cloud condensation nuclei (CCN). In reality this relationship does not hold; yet the avoidance of a geophysical chemistry parameterisation improves the speed of the simulations. Furthermore, CCN transport equations do not exist in PUFFIN at present and the model is simply simulated with a given N value determined through research data available on the number concentration of cloud particles for a given cloud type. Should PUFFIN be modified to include CCN transport equations and with the presence of an atmospheric CCN chemistry parameterisation, even the number concentration of cloud particles, N, could be determined within the simulations.

The final expression for the autoconversion rate adopted by Wyant et al. is a slightly modified version of equation (5):

$$P_{1} = \pi \alpha \overline{E}_{1} C_{1} N \overline{r}_{w}^{4} \chi (\overline{r}_{w}) q_{1}$$
 (8)

$$\chi(\overline{r}_w) = 1$$
 $\overline{r}_w \ge 10 \mu m$ 

$$\chi(\overline{r}_w) = (\overline{r}_w / 10 \mu m)^3$$
 $\overline{r}_w < 10 \mu m$ 

here the multiplicative constant,  $\alpha$  ( $\alpha$  = 0.5), is incorporated into the parameterisation. Another function is incorporated into the parameterisation which has the effect of gradually smoothing the fourth moment drop radius value to a zero value for drops with a radius less than  $10\mu m$ .

The second autoconversion parameterisation used for the sensitivity simulations is based on the autoconversion relation proposed by Kessler (1969) and adopted by Thompson et al. (2004) in equation (L3).

$$\frac{dq_r}{dt} = aH(q_l - q_{co}), \qquad (L3)$$

where the threshold value,  $q_{co} = 0.35 \times 10^{-3}$ ,  $a = 1 \times 10^{-3} \text{ s}^{-1}$  is a time constant and H is the Heaviside function (See section 2.1.4 for further details).

#### 3.1.3 Accretion

Accretion by definition is the collection of cloud droplets by rainwater as they fall through the cloud layer. Again, this makes use of the collision theory given in equation (4). The key difference between the autoconversion and accretion parameterisations is that the accretion function is based on the mechanism through which droplets are collected to form larger droplets or rain; a mechanism linked to the increased size and velocity of hydrometeors descending through the cloud layer.

Here, the Marshall-Palmer raindrop distribution function in equations (L2-a) and (L2-b) is adopted to determine the integral of the drop size distribution found in the collision theory (4):

$$n(r) = n_0 \exp(-r/r_m) \qquad (9)$$

Based on the assumption that the rainwater content is minimal in stratocumulus clouds,  $n_0$  is held constant at 8 x  $10^6$  m<sup>-4</sup>. This could be modified to vary with the rainwater mixing ratio through the parameterisation of raindrop break-up effects as done by Tripoli and Cotton (1980) but our assumption of minimal rainwater content eliminates the necessity to do so. The integral of equation (9) over the entire range of droplet radii provides us with the relation for the mass weighted droplet radius,  $r_m$ :

$$r_m = \left(\frac{\overline{\rho}q_r}{8\pi\rho_l n_0}\right)^{1/4},\tag{10}$$

here  $q_r$  is the rainwater mixing ratio,  $\bar{\rho}$  is the anelastic base state density variable,  $\rho_l$  is the density of liquid water and  $n_0 = 8 \times 10^6 \,\mathrm{m}^{-4}$ .

Using the fall speed parameterisation from Rogers and Yau (1989), a parameterisation of the precipitation flux, and collection efficiency,  $E_2$ , of 1.0 we have an approximate solution for the accretion rate:

$$P_2 = -\frac{3}{16} \frac{\overline{E}_2 \times F_P \times q_l}{\rho_l r_m} \tag{11}$$

$$F_p = -4\overline{\rho}C_2 r_m q_r \quad . \tag{12}$$

Here the precipitation flux,  $F_p$ , is derived through the integration of fall speed over the drop size distribution in (9). Although Wyant et al. neglect the small  $C_1$  term in their parameterisation, we have included it in our model due to concerns over the stability of PUFFIN. The accretion term is based on the cloud liquid water and the rainwater mixing ratios; this is because accretion is the process in which cloud droplets are collected by rainwater droplets and the presence of clouds and rainwater in our model are only defined through their respective mixing ratios.

#### 3.1.4 Evaporation

The parameterisation for evaporation as used by Wyant et al. is sourced from Rogers and Yau (1989) in their droplet evaporation expression. The evaporation function makes the assumption that evaporation only occurs when relative humidity (RH) is less than unity. The expression itself is formulated through the integration of the droplet evaporation expression by Rogers and Yau over the Marshall-Palmer raindrop distribution and is parameterised as follows:

$$E = \frac{8\pi n_0}{\overline{\rho}} \frac{(1 - RH)}{(A + B)} \left[ 0.39 r_m^3 + 0.4 \left( \frac{\overline{\rho} C_2}{\mu} \right)^{1/2} r_m^3 \right] \qquad RH < 1.0$$

$$E = 0 \qquad RH = 1.0$$

$$RH = \frac{q_v}{q_{sat}} \qquad A = \frac{L^2}{KR_v T_{env}^2} \qquad B = \frac{R_v T_{env}^2}{D_{vap}^2 e_s (T_{env})} .$$

The water vapour mixing ratio,  $q_v$ , is the difference between the total water mixing ratio and the liquid water mixing ratio (14). This water vapour mixing ratio is used to directly calculate relative humidity which is a function of the evaporation rate. The evaporation rate is the evaporation of raindrops in subsaturated air; where relative humidity is less than 100%.

$$q_{v} = q_{t} - q_{l} \qquad (14)$$

This model assumes that within regions where relative humidity is unity, evaporation can not occur. This is another approximation since evaporation within cloudy regions does occur during the course of natural geophysical processes, but will suffice for the purposes of our analysis.

## 3.2 Microphysics – Source terms

As described earlier, the cloud microphysics attach as partial time derivatives to the prognostic variables (1). The conceptual framework for the formulation of these partial derivatives is based on the effect each of the three micro-processes (autoconversion, accretion and evaporation) have on the prognostic variables. Autoconversion and accretion form rainwater, evaporation occurs in subsaturated air, when the relative humidity is less than 100%; the evaporated rainwater then returns into the boundary layer to reform clouds. From this simple formula, the clouds can now form through the availability of water and water vapour in the atmospheric boundary layer, and disappear due autoconversion and accretion.

## 3.2.1 The total water mixing ratio source term

The total water mixing ratio in (1) identifies the presence of the cloud liquid water mixing ratio and the water vapour mixing ratio that is present in the ABL; this relationship is described by (14). The cloud liquid water mixing ratio is determined through (2). Anywhere within the ABL where there is a presence of water identified with a total water mixing ratio greater than zero, there will always exist some proportion of either cloud liquid water or water vapour (identified through their respective mixing ratios). Here the microphysics plays the central role of exerting an unambiguous positive or negative effect on the total water mixing ratio as computed by the prognostic relation, dependent solely on the rate at which the autoconversion, accretion and evaporation micro-processes are occurring.

Since we have already described the parameterisations for the micro-processes, it is necessary to introduce the equation used to compute the partial time derivative microphysics term for the total water mixing ratio:

$$\left(\frac{\partial q_t}{\partial t}\right)_{microphysics} = -\left(P_1 + P_2 - E\right). \tag{15}$$

The autoconversion and accretion parameterisations in equations (8) and (11) respectively exert a negative effect on the microphysics governing the total water mixing ratio (also discussed in Section 2 of this thesis). The evaporative process has a positive effect on the total water mixing ratio; actively increasing the total water present in the ABL. It should be of no surprise that the cloud liquid water mixing ratio, determined through (2), is one of the factors that acts to increase autoconversion and accretion. This indicates that the processes are all linked together in a complex manner; the complexity reflects on the capacity to simulate atmospheric micro-processes, tying into our discussion earlier regarding complexity and computing cost.

## 3.2.2 The rainwater mixing ratio source term

The second prognostic variable that is vital for the simulation of cloud microphysics is the rainwater mixing ratio. As the name indicates, this is the microphysics component of the rainwater mixing ratio as represented in (1) that is used to represent rainfall in the ABL as a result of the micro-processes of autoconversion, accretion and evaporation. The microphysics here is represented in the following form:

$$\left(\frac{\partial q_r}{\partial t}\right)_{\text{microphysics}} = P_1 + P_2 - E - \frac{1}{\overline{\rho}} \frac{\partial F_p}{\partial z} .$$
(16)

Here autoconversion and accretion have a positive influence on the rainwater mixing ratio as they would be expected to intuitively. By definition, autoconversion is the process where cloud drops collide to form larger cloud drops that can then begin to contribute to the formation of raindrops and accretion is the collection of cloud droplets by raindrops falling through the cloud layer, increasing the quantity of rain in the ABL and hence increasing the rainwater mixing ratio. The evaporation process here acts to evaporate the falling raindrops and has the negative effect on the rainwater mixing ratio. There is a fourth term in the source however; the partial derivative of the precipitation flux,  $F_p$ , see equation (12), with respect to altitude. The precipitation flux partial derivative term is present for the purposes of parameterising the rainfall through the boundary layer from one grid square to another; essential for the simulation of rain.

#### 3.2.3 The liquid water potential temperature source term

The liquid water potential temperature microphysics function dictates changes in potential temperature variable caused by autoconversion, accretion and evaporation in the ABL. This potential temperature function is necessary because it is used to influence the air temperature within the ABL as there must always be energy released in the form of heat when water vapour condenses. The opposite occurs during evaporation because

evaporation is an endothermic process; here there is a cooling effect during the evaporation process on raindrops. This directly implies that the microphysics term that contributes to the potential temperature variable of the PUFFIN LES model is a function of the autoconversion, accretion and evaporation rates. The source term computes the reduction or increase of the potential temperature within the boundary layer based upon fluctuations of the total water, cloud liquid water and rainwater mixing ratios as follows:

$$\left(\frac{\partial \theta_l}{\partial t}\right)_{\text{microphysics}} = \frac{L}{C_p \Pi_{env}} (P_1 + P_2 - E) .$$
(17)

where L is the latent heat of vaporisation at 273 K,  $C_p$  is the constant pressure specific heat and  $\Pi_{env}$  is the Exner function; the environment temperature divided by the environment potential temperature.

Disregarding the slight variation in our model with the introduction of the Exner function, the microphysics component for the liquid water potential temperature is the multiplication of the autoconversion, accretion and evaporation rates with a time varying constant located outside of the brackets throughout the entire ABL. Our model simply modifies this slightly with a more accurate altitude and time varying constant which multiplies with the micro-processes. It is necessary to raise the point that without the liquid water potential temperature microphysics function, the model would become extremely unstable. The temperature effects of condensation, autoconversion, accretion and evaporation must be accounted for; on the aggregate macro-scale, these temperature effects due to the microphysics have a substantial impact on the ABL. This is a powerful yet obvious statement but raises a far more discrete notion; one that highlights the significance of cloud micro-processes acting on the macro-scale geophysical processes within the ABL. This idea will be taken further into the analysis stage of this

report to the extent that data analysis of the cloud microphysics need only be limited to comparisons between macro-scale data including inversion height and vertical wind velocity profiles.

## 3.3 Radiation

The radiation budget must be considered in order to drive reasonable simulations in PUFFIN-ABL. The simulations conducted are all nocturnal, however there still exist radiation considerations for long wave cooling and warming. As discussed in section 2, the parameterisation by Stevens et al (2004) has been used because it was specifically developed for the DYCOMS-II LES simulations; the work conducted in this paper parallels that research and it is the ideal parameterisation to use since it would standardise the results to some degree.

$$F_{rad}(x, y, z, t) = F_0 e^{-Q(z, \infty)} + F_1 e^{-Q(0, z)}$$

$$+ \rho_i c_p D \alpha_z \left[ \frac{(z - z_i)^{4/3}}{4} + z_i (z - z_i)^{1/3} \right]$$

$$Q(a, b) = \kappa \int_a^b \rho q_i dz$$
(18)

here, the first term  $F_0e^{-Q(z,\infty)}$  is used to define cloud top cooling,  $F_1e^{-Q(0,z)}$  defines cloud base warming and the third term is the long wave cooling of the free troposphere above the cloud top. The parameter values selected by Stevens et al. (2004) are the same we have used where  $F_0 = -70Wm^{-2}$ ,  $F_1 = 22Wm^{-2}$ ,  $\kappa = 85 \text{ m}^2 \text{ kg}^{-1}$ ,  $c_p = 1.015 \text{ kJ kg}^{-1} \text{ K}^{-1}$ ,  $D = 3.74 \times 10^{-6} \text{ s}^{-1}$  is the divergence of large scale winds,  $\alpha_z = 1 \text{ m}^{-4/3}$  (used to cancel out the metre dimension within the brackets). Regarding the variables,  $z_i$  is the inversion height,  $z_i$  is any height subject to  $z_i \le z < \infty$ , and  $\rho_i$  is the air density just below the cloud top; Stevens et al. (2004) assume this to be a constant value,  $\rho_i = 1.13 \text{ kg m}^{-3}$ .

The Q(a,b) function is a negative power of the exponential term; resulting in an exponential decay on the cooling and warming parameters  $F_0$  and  $F_1$  respectively. In cloud top and cloud base regions of high density and increased levels of cloud liquid water, the cooling term is considerably reduced. The opposite occurs with negligible density and cloud liquid water; as the exponential decay function tends to unity, the cloud top cooling and cloud base warming reach their maximum values. Since the long wave cooling and warming terms are all expressed in watts per metre squared, additional manipulation had to be conducted in order to translate them all into dimensions that could be added to the potential temperature source term in PUFFIN to apply the radiative forcings onto the model.

See Appendix A for the source codes

# 4. SIMULATION SETUP

## 4.1 PUFFIN-ABL boundary conditions

The simulations have been conducted within a non-uniform 3D Cartesian grid domain. The coarse resolution (CR) and high resolution (HR) simulation grid setup in PUFFIN-ABL uses the settings presented in Table 1.

X	Maximum Cells	West Boundary	East Boundary
CR	50	-2,000 m	2,000 m
HR	80	-2,000 m	2,000 m

Y	Maximum Cells	South Boundary	North Boundary
CR	50	-2,000 m	2,000 m
HR	80	-2,000 m	2,000 m

Z	Maximum Cells	Bottom Boundary	Top Boundary
CR	40	0 m	1,600 m
CR Fine Regions		0 – 10 m	850 – 860 m
HR	80	0 m	1,600 m
HR Fine Regions		0-5 m	850-855 m

**Table 1:** PUFFIN-ABL 3D Cartesian grid domain settings for the base, sensitivity and the high resolution simulations, located in the PUFFIN-ABL input file (Appendix C). Only the DII\_fine sensitivity simulation is tested within the high resolution domain.

The domain grid parameters are located within the PUFFIN-ABL input file that can be modified as required for each simulation. All the simulations save one were conducted using the base settings for consistency. The dimensions of the domain are of sufficient magnitude to simulate the development of cloud structures without unnecessarily exhausting computing resources and time. The simulations were run for 7200 seconds;

suitable for the available hardware resources and time. This included a spin up period of 3600 seconds, a process suggested by Stevens et al. (2004) to avoid the inclusion of errors in the results from an increase of turbulent kinetic energies occurring in response to the destabilisation of the ABL due to the specified surface fluxes and radiative forcings.

## 4.1.1 Boundary Conditions

The boundary conditions for the simulations were again set in the PUFFIN-ABL input file and were kept at one setting to maintain consistency with the simulations. The domain boundary was set up to match the actual geophysical processes as closely as possible. The north, south, east and west boundaries are all periodic, which makes them open to the mass and momentum fluxes which traverse the domain. At the bottom boundary mean fluxes have been set for the total water mixing ratio, the potential temperature and the momentum. The rainwater mixing ratio was given a zero flux condition at the bottom boundary and the top boundary layer had all the scalars and velocities set to zero flux.

Parameter	Value	<b>PUFFIN Parameter</b>	Value	
Surface Drag Coefficient - C <sub>D</sub>	0.0011	Friction Velocity – u*	0.208 m.s <sup>-1</sup>	
Surface Latent Heat Flux – Q`s	115 W.m <sup>-2</sup>	Surface Moisture Flux – c*u*	3.77 x 10 <sup>-5</sup> kg/kg . m.s <sup>-1</sup>	
Sensible Heat Flux – Q`s	15 W.m <sup>-2</sup>	Surface Heat Flux – θ*u*	0.0121 K. m.s <sup>-1</sup>	

**Table 2:** The surface flux boundary conditions are listed. The table contains surface flux parameters given by Stevens et al. (2004) and their respective PUFFIN parameters (see Appendix B for conversion calculations).

## 4.1.2 Surface fluxes

The surface fluxes described above have been determined using the following parameters given by Stevens et al. (2004) for their DYCOMS-II LES simulations. The bulk aerodynamic drag coefficient is given as  $C_D = 0.0011$  which corresponds to a surface sensible heat flux of 15 W.m<sup>-2</sup> and a surface latent heat flux of 115 W.m<sup>-2</sup>. To use this data in PUFFIN, these parameters must be first converted to the dimensions in which they are used as input parameters within the PUFFIN input file. Table 2 presents a tabulated summary of the surface flux boundary conditions.

See *Appendix B* for calculations

## 4.2 Initial Conditions

We used the initial conditions set by Stevens et al. (2004) for our own simulations to maintain consistency with the comparison of our model. The PUFFIN input file requires only two temperatures for the initial conditions required to run a simulation; the remainder is resolved by PUFFIN-ABL during the simulation. The temperature just above the surface of the boundary layer is set at 290.4 K and the surface temperature which in our case is also the sea-surface temperature is 292.5 K. The geostrophic wind speeds were input as 5.5 m/s for westerly flowing wind and 7 m/s for northerly flowing wind and it was the resultant of the westerly and northerly wind speed values that was used for the surface friction velocity calculation. There are two input parameters for the total water mixing ratio. One is to specify the free tropospheric total water mixing ratio above the inversion and the other below the inversion for the boundary layer. The values used are as follows:

$$q_t = 0.009$$
  $z \le z_i$   
 $q_t = 0.0015$   $z > z_i$ ,

here  $z_i$  is the inversion height, initially set at 840m. For the simulations this inversion height is identified as the height at which the planar averaged total water mixing ratio is 8g/kg. This was selected because the presence of water encounters a sharp drop at the inversion and is an accurate identifier of the inversion height. Stevens et al. (2004) and Wyant et al. (1997) use the 8g/kg and 5g/kg isolines respectively for determining the inversion height; varying these parameters within the bounds 1.5 - 8 g/kg should not result in a noticeable disparity between the inversion heights. An arbitrary initial inversion thickness of 100m was used for the simulations since no other data was available from the DYCOMS-II research and the LES simulations by Stevens et al. (2002, 2004).

## **4.2.1** Physical Constants

For certain physical constants such as the specific latent heat of vaporisation,  $L_{\nu}$  and constant pressure specific heat,  $c_p$ , we have used values that are slightly different, but these would not make a great difference to the results in the simulation and changing the values to be exact would be unnecessary considering the scope and breadth of the simulations we are conducting for this report.

# 4.2.2 Microphysics

Cloud structure is an important consideration to take into account, particularly because the microphysics parameterisations in Wyant et al. (1997) that we have used rely heavily on the cloud droplet number concentration. This has already been discussed in both section 2 and 3. For the DII-series simulations, an average number concentration,  $N = 145.3 \text{ cm}^{-3}$  was used; this average was taken from the DYCOMS-II flight data (Stevens et al., 2002). In their paper, Wyant et al (1995) paper make the assumption that the cloud particle number concentration is equal to the CCN

concentration; we have not employed this assumption directly for our simulations since we are already provided with actual data for the cloud number concentration. Stevens et al. use an expression to determine the number concentrations with the coefficients derived from fitted data:  $N = Cs^k$ . The derivation of this expression does not need to be discussed, however it must be said that the value of N we have used, implicitly involves the use of the expression proposed by Stevens et al. (2004). Regarding the current model, if the exact value of N isn't known or provided, the simple relationship between CCN and N as discussed in section 3.1.2, suffices for future experimentation.

**4.2.3** Simulation Parameters Summary

Туре	Parameter	Value
<b>Boundary Conditions</b>	Sea Surface Temperature	292.5 K
	Temperature just above surface	290.4 K
	Easterly Geostrophic wind flow	-5.5 m/s
	Northerly geostrophic wind flow	7.0 m/s
	Cloud number concentration, N	145.3 cm <sup>-3</sup>
Initial Conditions	Inversion height	840 m
	Thickness of inversion	100 m
	Free tropospheric q <sub>t</sub>	1.5 g/kg
	Boundary layer q <sub>t</sub>	9.0 g/kg
Simulation	Length of simulation	7200 seconds
	Time step	0.1 - 20 seconds
	Start recording statistical data	3600 seconds

**Table 3**: Parameters used for the base and sensitivity tests: DII\_base, NoRad, Kessler1, Kessler2 and DII\_fine. Includes the summary of initial and boundary conditions and simulation settings.

# 4.3 Analysis methods

Several data analysis techniques have been employed to interpret the data made available from the simulations. Profile data samples are taken from the last 3600 seconds of the simulations and then averaged. The analysis we conduct compares the data made available from our own simulations, with data and findings obtained from the DYCOMS-II research flights and the DYCOMS-II LES collaborations in Stevens et al. (2004). More specifically, the more sophisticated comparisons have been conducted using the rate of change of the inversion height and the skewness of vertical wind profiles within the boundary layer. These two statistical measures make use of the significant influence of cloud systems on physical processes within the ABL.

## **4.3.1** Temporal inversion height variation

The temperature inversion above the turbulent planetary boundary layer (PBL) is a heavily researched phenomenon because it is the location of entrainment processes that drive the development, decoupling and dissipation of cloud structures in the planetary boundary layer.

As streams of dry air entrain into the boundary layer below the inversion, they mix with the cloud canopy below. The increased quantity of dry air entraining into the boundary layer can cause a localised dissipation of the cloud canopy in certain regions through drying effects. Depending on the rate of entrainment, this phenomenon can contribute to an increase of the inversion height altitude and can also initiate the decoupling or break-up of the cloud structure. Currently there are limitations to the reliability of entrainment data obtained from LES simulations because many physical processes play key roles in the process of entrainment, including radiative forcings, thermodynamic and cloud microphysical processes (Stevens et al. 2004). The latter of

the three is the basis on which the inversion height analysis is conducted for our simulations.

A gradual increase in inversion height will be determined through the measurement of the total water mixing ratio at the 8g/kg isoline. The increase in inversion height is attributed to the increased entrainment of air from the free troposphere into the cloud canopy and boundary layer, which pushes the inversion to higher altitudes. The data is collected by recording the inversion height over time and comparing that with the results observed in the DYCOMS-II simulations. The entrainment rate is computed by dividing the change in inversion height over time,  $\Delta z_i/\Delta t$ . It is this entrainment rate that will provide insight into the behaviour of our cloud and radiation models in comparison to the DYCOMS-II LES simulations.

## **4.3.2** Third moment of vertical velocity profile, $< w'^3 >$

Cloud micro-processes affect the turbulence statistics of the vertical component of velocity, w. The analysis of w statistics allows for a comparison with results obtained by Stevens et al. (2004). The third moment or skewness of w offers a great deal of information regarding the effects of cloud microphysical processes on the ABL. This can assist in ascertaining the validity of our cloud model by running comparisons with the more accurate microphysics programs in the DYCOMS-II LES simulations.

To be more specific, the profile of  $< w'^3 >$  can be used to characterize the turbulent structure of the ABL; it is this turbulent structure that is influenced by the presence of clouds. Provided the LES model used to run an ABL simulation is accurate, cloud structures within an ABL simulation can be compared for different LES models and cloud microphysics models. Since the third moment of w measures the structure of turbulence, we analyse properties of skewness results and interpret them according to observable properties of clouds with respect to upward and downward turbulent motion

caused by buoyancy effects. A negative skewness is used to identify a strong downdraft likely to be caused by flow driven by radiative cooling and positive skewness indicates updrafts associated with the surface and cloud convection. It is also important to appreciate the role of radiative forcings that drive the turbulent flow within the cloud structures, since the cooling and warming of the clouds act to enhance the localised turbulence within the cloud structure, rendering the localised flow within clouds distinctly observable in the third moment or skewness profile.

With the comparison of temporal inversion altitude variations and the third moment of the vertical velocity profile between our simulations and the LES simulations conducted by Stevens et al. (2004), an appraisal of the cloud microphysics schemes we have adopted is possible. PUFFIN-ABL is an LES model, similar to those used in the DYCOMS-II LES collaborative simulations and the LLAMA plug-in (a subgrid scale turbulence model coefficient algorithm and LES length scale calculator developed by Kirkpatrick) we have used for some of our testing was also used for the DHARMA simulation presented in the DYCOMS-II LES contributions. Furthermore, the standardised radiation parameterisation used for the DYCOMS-II simulations has also been used in our model.

Within the bounds of resource constraints, every possible detail has been addressed to ensure a satisfactory degree of consistency with the LES simulations in the Stevens et al. (2004) simulations. Variations and errors in the data from the DII series simulations we have conducted can therefore be attributed to factors including errors or inconsistencies in the microphysics code, integration issues between the microphysics module and PUFFIN-ABL (again a programming issue), incorrect implementation of long wave radiation budget or an ensuing disagreement with the microphysics code and the proposed radiation model. The hope of this research is to obtain a rate of change of the inversion height and skewness of vertical wind profiles in very close correlation to

the data from the DYCOMS-II research flights and the LES simulations by Stevens and the other contributors. This then would suggest that the cloud microphysics scheme integration into PUFFIN is satisfactory for further micro-scale ABL and PBL research.

## 4.3.3 Vertical statistical profile analysis

The vertical profiles of the total water mixing ratio, the cloud liquid water mixing ratio and the liquid water potential temperature variables are utilised to interpret and compare mean results collected from the final hour of the simulations (hence a statistical profile – using the mean of temporal profile data). The mixing ratio profiles and the liquid water potential temperature profile have been used to further assess the behaviour of the simulations. The Wyant et al. (1997) and Stevens et al. (2004) papers provide the relevant comparisons in order to determine the reliability of data produced from our DII-series simulations.

## 4.4 DII-series simulations

Five simulations have been tested in the DII-series simulations we have conducted for this thesis.

 DII\_base - The base simulation incorporating the microphysics model proposed by Wyant et al (1995) and the radiation model proposed by Stevens et al. (2004).

## 2. Sensitivity simulations

- i. NoRad Base simulation excluding the radiative forcings proposed by Stevens et al.
- ii. Kessler1 Base simulation with microphysics modified to adopt Kesslers autoconversion parameterisation with a threshold value of  $0.35 \times 10^{-3}$ .

- iii. Kessler2 Base simulation with microphysics modified to adopt Kesslers autoconversion parameterisation with a threshold value of  $0.5 \times 10^{-3}$ .
- iv. DII\_fine High resolution simulation incorporating base simulation parameters, microphysics and radiation models, with a modified, finer discretization of the 3D Cartesian grid domain.

## **4.4.1 DII** base

The base simulation incorporates the microphysics scheme adopted by Wyant et al. (1997), as well as the radiation paramaterisations proposed by Stevens et al (2005). The simulation, initial and boundary conditions for DII\_base were previously specified in section 4.2.3 and Table 3. These were based on the data collected during the DYCOMS-II research flights and the initial and boundary conditions specified in the Stevens et al. paper for the LES collaborations. The DII\_base simulation is designed to closely reflect all the observed conditions during the DYCOMS-II research in order to run a thorough comparison.

#### **4.4.2** NoRad

This sensitivity simulation is designed to determine the overall effect of radiative forcings on the ABL when coupled with the microphysics scheme in DII\_base. This is essential to understanding the nature of the microphysics, with and without the presence of radiation. Analysis is conducted on the cloud structure, entrainment rate and temperature effects of radiative forcings on the boundary layer.

## 4.4.3 Kessler1, Kessler2

The Kessler1 and Kessler2 sensitivity simulations modify the base simulation microphysics scheme to incorporate the autoconversion parameterisation in equation (L3) proposed by Kessler (1969) and adopted by Thompson et al. (2004). The effectiveness of a simpler autoconversion parameterisation is assessed using this simulation in comparison to both the DII\_base simulation and the DYCOMS-II LES simulations. The threshold value,  $q_{co} = 0.35 \times 10^{-3}$  is used for Kessler1 because it is a revised and tested threshold value used by Thompson et al. for their base simulation and  $q_{co} = 0.5 \times 10^{-3}$  is used in the Kessler2 simulation to assess how varying the threshold value can affect the simulation.

## **4.4.4 DII\_fine**

A high resolution sensitivity test is conducted with the same simulation parameters, microphysics scheme and radiation model that have been tested in the base simulation. The purpose of this is to ascertain the impact of a reduction in discretization errors during the simulation. Discretization error reduction is realised through the testing of the model within a high resolution domain. In order to achieve this, the high resolution PUFFIN-ABL domain input parameters in Table 1 are required to generate a finer discretization of the domain during the simulation. The reason for only a single high resolution simulation is primarily due to the excessively long processing times that were required to test the simulations within a more finely discretized 3D grid domain; attributable to the limited computing resources available. For this thesis, there was only the need for one high resolution sensitivity simulation simply to establish a point of comparison between course and high resolution simulations.

# 4.4.5 Summary of DII-series simulations

Simulation Name	Description	Domain Grid	Radiation
DII_base	Adopting microphysics scheme proposed by Wyant et al. (1997) and radiation model proposed by Stevens et al. (2004). Initial conditions presented in Table 3 given by Stevens et al. (2004) and DYCOMS-II flight data	Coarse Resolution	X
NoRad	DII_base microphysics. Analysis of microphysics scheme with no radiative forcings.	Coarse Resolution	
Kessler1	Modification of the microphysics scheme proposed by Wyant et al. (1997) with the autoconversion parameterisation replaced with Kessler's autoconversion in equation (L3) where $q_{co} = 0.35 \times 10^{-3}$ .	Coarse Resolution	X
Kessler2	Modification of the microphysics scheme proposed by Wyant et al. (1997) with the autoconversion parameterisation replaced with Kessler's autoconversion in equation (L3) where $q_{co} = 0.5x10^{-3}$ .	Coarse Resolution	X
DII_fine	Tested within the high resolution PUFFIN-ABL grid domain using DII_base initial conditions, boundary conditions, microphysics and radiation schemes	High Resolution	X

**Table 4:** A short summary of the DII-series base and sensitivity simulations. The radiation parameterization is proposed by Stevens et al. (2004). Domain grid resolution is described in Section 4.1, Table 1.

# 5. RESULTS

We have used the results and visualisations generated by the DII-series simulations to describe cloud structure and cover as well as to analyse the entrainment rate, the skewness of  $< w^{13} >$  and the micro-processes driving the cloud microphysics scheme. The observations of cloud cover, thickness and structure were conducted using the top and side view simulation visualisations. Figure 1 is particularly useful in performing a preliminary assessment of the cloud structures and the precipitation generated as a result of the microphysics and radiation schemes implemented into PUFFIN-ABL.

Key characteristics of an accurate model include the presence of a single solid stratocumulus cloud structure with an average cloud thickness of 366m, a cloud canopy approximately located between 600m to 1075m and a cloud base located between 200m to 650m; these figures are obtained from the DYCOMS-II research data in Stevens et al, (2002). The single solid stratocumulus layer could not be replicated in the final hour of testing of the DII-series simulations, however the presence of cloud (white) and precipitation (transparent blue) provide a means of identifying the factors that could be used to refine the cloud microphysics scheme to perform more reliable and accurate simulations in the future.

DII\_base and NoRad appear to produce very similar results in terms of cloud cover and precipitation in the form of drizzle and rain; this suggests that the nocturnal long-wave radiative forcings only have a minor effect on the cloud microphysics. The sensitivity simulations all produce similar isolated cumulus cloud systems, with DII\_fine being the exception having a noticeably greater cloud depth based on figure 9. The Kessler1 and Kessler2 models both retain cloud systems covering greater areas of the domain for a longer period of time; however they too undergo dissipation and break-up toward the end of the simulation and similar in appearance to DII\_base.

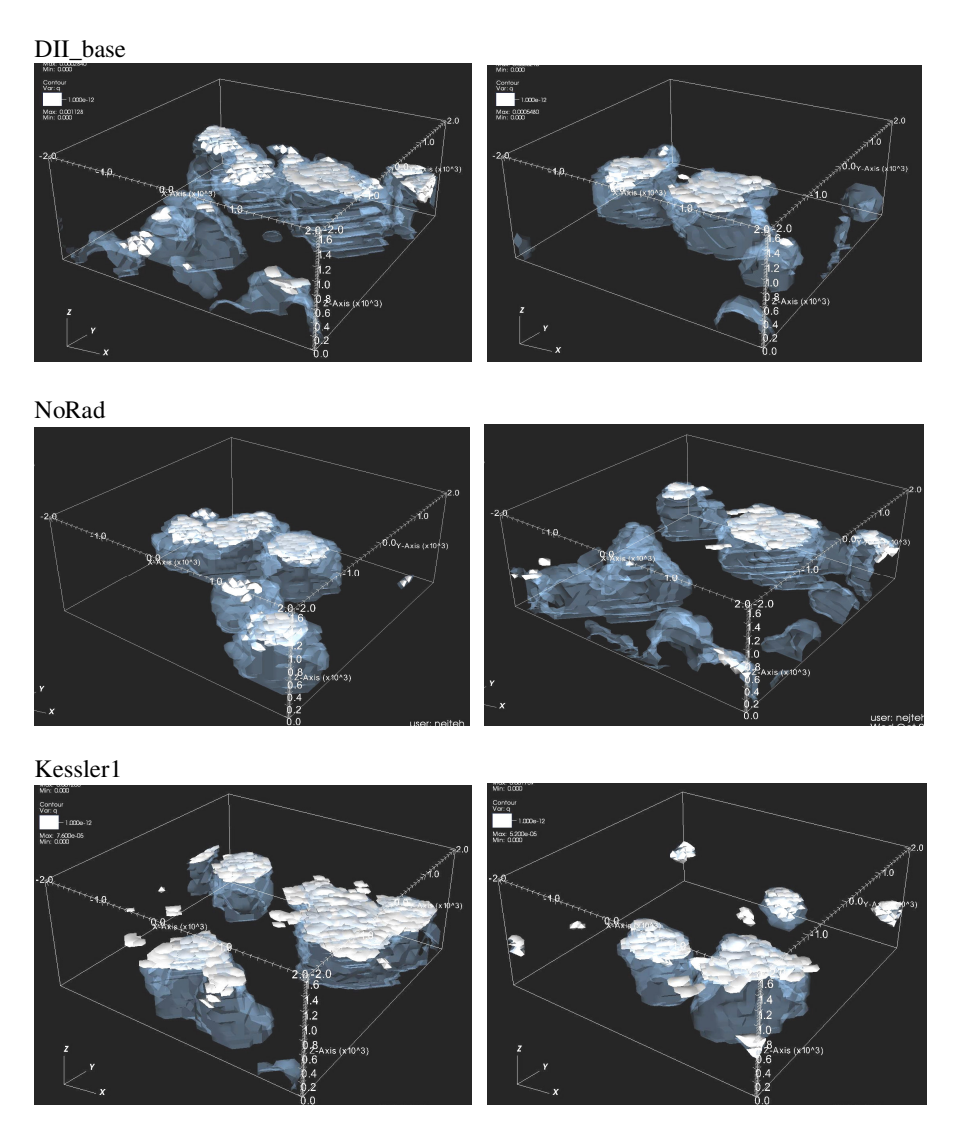


**Figure 1**: Isometric views of the simulations taken at the beginning (left) and end (right) of the final hour of simulations for each test case (at time=3600 seconds and time=7200 seconds respectively). There is evidence of considerable precipitation (and drizzle) generated within the isolated cumulus cloud systems in the domain.

Visualisations of the DII\_base and Kessler1 simulations are presented in *Appendix D*.

## 5.1 Cloud cover

From the base and sensitivity simulations, considerable break-up and dissipation of the cloud structure is observed after the first hour as depicted in Figure 2. Toward the end of the simulation, the cloud structures break down into smaller, isolated cumulus systems that still generate precipitation.

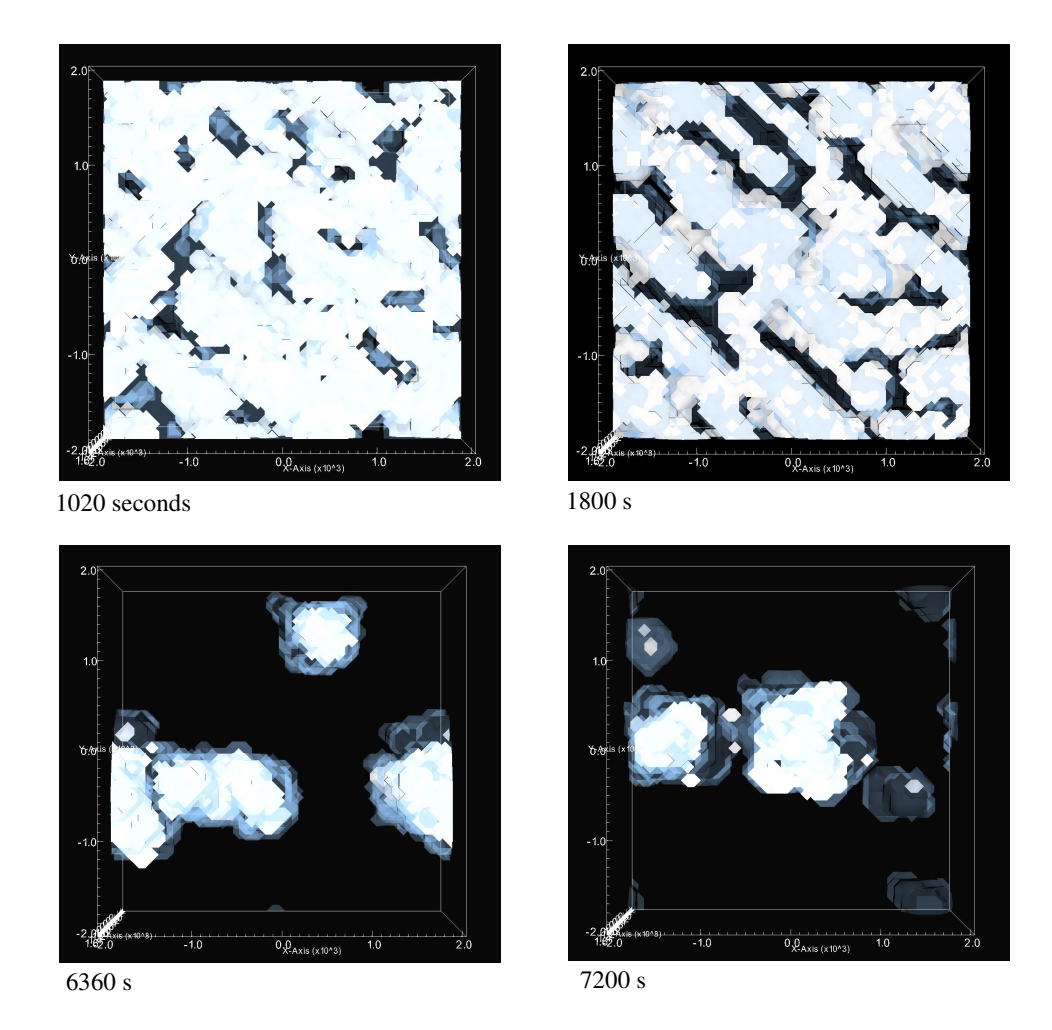


**Figure 2**: The cloud cover observations from the DII\_base simulation show considerable break-up of the near solid, stratocumulus cloud layer to isolated cumulus cloud systems.

During the spin up period, the cloud structure appears to be in line with the formation of a single solid stratocumulus cloud layer albeit with occasional breaks. However, the results obtained from the spin-up period are mostly ignored because of the unreliability of the data produced. This is due to the increase in turbulent kinetic energy within a temporarily destabilized boundary layer at the start of the tests; the source being surface fluxes and radiative forcings. After the first hour of the simulations, once the boundary layer stabilizes, the mostly uniform stratocumulus layer has been transformed into isolated clouds traversing the boundary layer as shown in Figure 2.

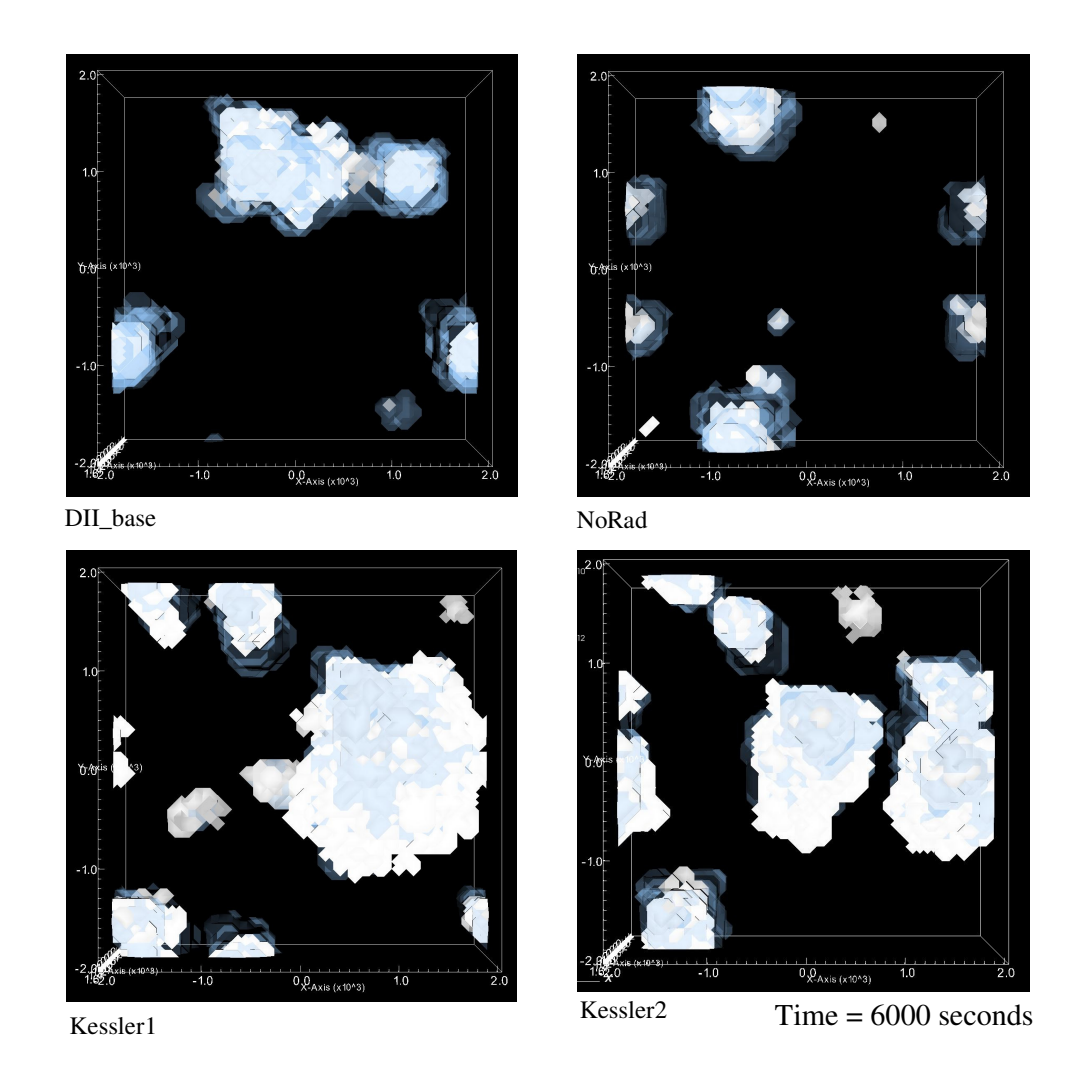


**Figure 3**: The cloud cover observations taken at time= 6000 seconds to compare the DII\_base, NoRad, Kessler1 and Kessler2 simulations. There are obvious indications that although considerable cloud break-up does occur in all four simulations, the Kessler1 and Kessler2 simulations undergo far less dissipation.

There is also a considerable quantity of precipitation generated by these clouds indicating that the autoconversion and accretion parameterizations may require some modification to moderate the excessive rainfall and drizzle observed; we postulate that this is also the probable cause of the transformation of the single cloud layer because the micro-processes contributing to total change of the rainwater mixing ratio reduce the total water mixing ratio by the same amount.

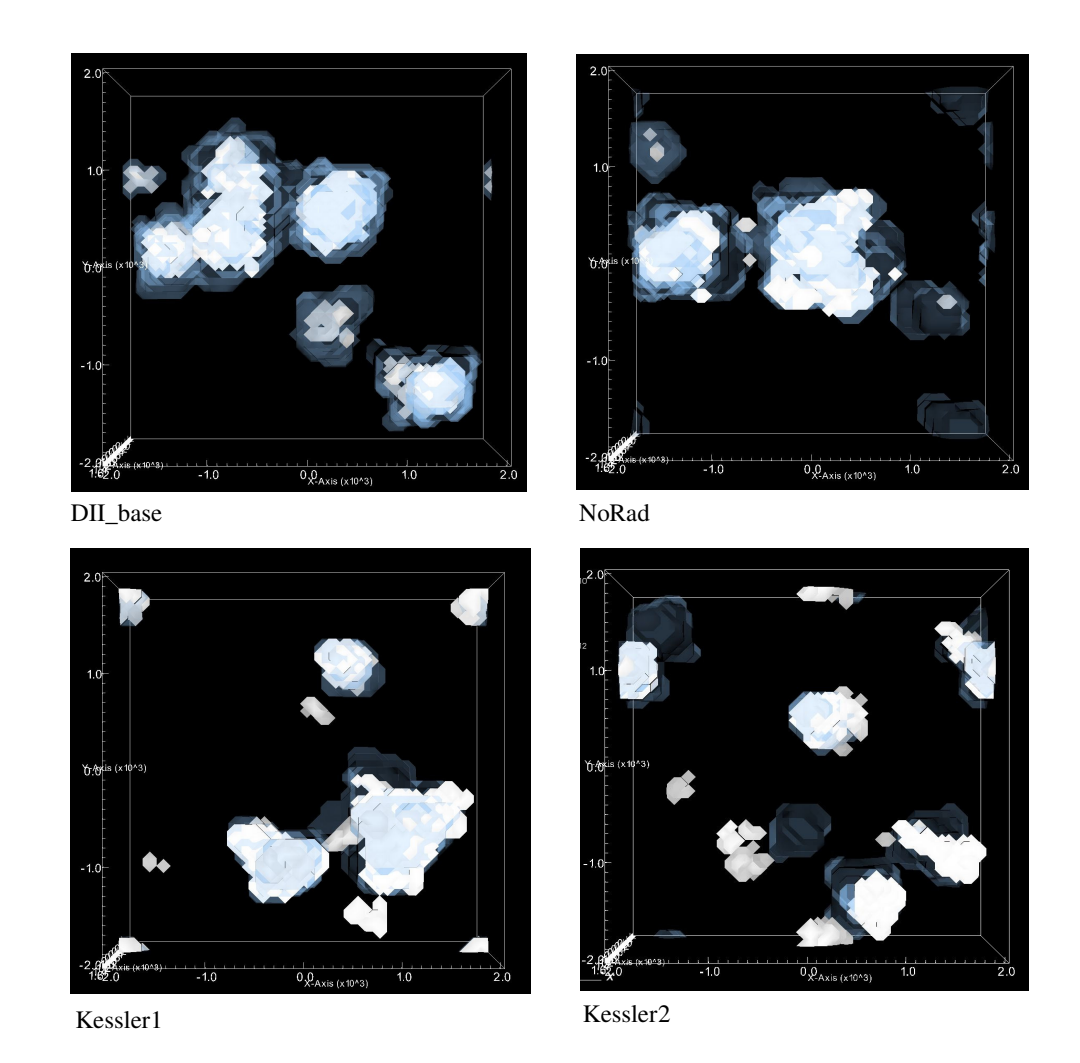


**Figure 4**: The observations of cloud cover at time = 7200 seconds indicate that the base simulation and three coarse resolution sensitivity simulations all appear to experience the same degree of dissipation and break up. The autoconversion modification implemented into the Kessler1 and Kessler2 models simply slows down the rate of dissipation.

The sensitivity simulations also provided similar results in terms of cloud cover with considerable break-up occurring during the final hour of the simulations (see Figure 3). The Kessler1 and Kessler2 simulations both showed slightly increased overall cloud cover during the final hour of the simulations; these cloud cover observations are confirmed by results obtained for the cloud liquid water mixing ratio statistical profiles (see Figure 9). The autoconversion parameterization used for the Kessler1 and Kessler2 simulations both reduced the autoconversion rate to level that

allowed the cloud formations to dissipate less than those in the DII\_base and NoRad simulations.

The cloud cover observed at the end of the second hour of all the simulations appear to be very similar. Even though the cloud structures for the Kessler1 and Kessler2 simulations remain large enough to cover a greater proportion of the boundary layer during most of the simulation, they eventually succumb to the same forces that contribute to the high levels of dissipation and break-up that are observed in the DII\_base and NoRad simulations evident in Figure 4. This implies that the autoconversion model proposed by Kessler (1969) has only managed to prolong, but not eliminate the cause of the high level of break up and dissipation. Furthermore, it allows us to identify a possible the cause of the break-up and dissipation as the implementation of the microphysics parameterisations.

## **5.2** Assessment of cloud structure transformation

In an attempt to circumvent this broken cloud structure, simulations were also run with a gradual spin-up procedure where the radiative forcings were applied beyond a certain time after the tests had started. This provided no change in the outcome of the simulations, but eliminated any assumptions that the spin-up procedure had any effect on the issue of cloud layer dissipation and break-up. Similarly, some of the DYCOMS-II LES collaborations, namely the UCLA-1 simulation, also encountered dissipation and break-up of the cloud structures and testing with a gradual spin-up procedure made no significant change to the behaviour of the models.

As discussed previously, the model also underwent preliminary testing with the LLAMA dynamic sub-grid scale turbulence models to establish whether that could reduce the cloud break-up and dissipation rate observed in the simulations that by default used classical Smagorinsky turbulence coefficients. The tests with the LLAMA

model did not indicate any improvement on the cloud structures and the results from the simulations with LLAMA were subsequently ignored.

Of the models tested with LLAMA and the gradual spin-up procedure, not one indicated a reduction of the cloud break-up and dissipation observations. This was consequently used to exclude any causal relationship between the use of the classical Smagorinsky turbulence model or spin-up procedure and the observed levels cloud dissipation and break-up. From here we can also deduce with some degree of certainty that the cloud break-up problem is more closely tied to the ABL model and the microphysics scheme implementation. This becomes more evident through the statistical profile analysis of the Kessler1 and Kessler2 tests where a simple modification of the autoconversion parameterization is shown to result in prolonged high levels of average cloud cover over the final hour of the simulations; a result that suggests that the implementation of the microphysics scheme proposed by Wyant et al (1995) may require revisiting.

#### 5.3 Profile results

Profile analysis is useful to establish the effects of the cloud microphysics scheme on the boundary layer. Since the tests were designed to match the DYCOMS-II conditions, the validation of the statistical profiles has been conducted using the results presented in Stevens et al. (2004) for the DYCOMS-II LES contributions.

See <u>Appendix E</u> for DII-series profile data.

#### 5.3.1 $\theta_1$ – statistical profile

The profile of the liquid water potential temperature,  $\theta_l$ , in Figure 5 is used as a useful measure of comparison between the DII-series simulations and the DYCOMS-II LES contributions presented by Stevens et al (2005). This is because the potential

temperature profile is affected by the formation of clouds and the evaporation of rainwater. With this in mind, we can analyse the effects of cloud cover on the mean liquid water potential temperature along the vertical axis of the domain.

In addition, the overall effects of the microphysics and the radiation schemes on the liquid water potential temperature can be assessed by comparing the DII\_base simulation and the NoRad simulation results.

#### Statistical Profile - θ<sub>1</sub> 1600.0 1400.0 1200.0 1000.0 Altitude (m) 800.0 <del>─</del>DII\_base 600.0 NoRad 400.0 Kessler2 DII fine 200.0 0.0 300.0 305.0 310.0 315.0 320.0 325.0 330.0 335.0 Temperature (K)

Figure 5: The  $\theta_l$  statistical profile identifies the height of the inversion in the boundary layer. The course and fine simulation profiles are approximately 20K and 10K higher than the initial  $\theta_l$  profile. The significant difference in  $\theta_l$  between the coarse and fine resolution profiles can not be identified. The temporal increase in  $\theta_l$  can be linked to lower levels of evaporation in comparison to autoconversion.

There was no great observable difference between the  $\theta_l$  profiles of DII\_base and the sensitivity simulations (see figure 5) and although the profile shapes were in line with those produced by the DYCOMS-II LES master ensemble, the  $\theta_l$  statistical profiles were over 20 Kelvins higher in the DII-series simulations. There is an obvious gradual temporal change in the vertical (sea-surface to inversion)  $\theta_l$  profile of the ABL during the DII-series simulations, from an initial state of 290K to a final hour average of approximately 314K save DII\_fine with a final hour mean of approximately 305K. This

is unlike the  $\theta_l$  profile statistics illustrated by Stevens et al. (2004), where no significant temporal temperature change is observed; this comparison suggests that there may be evidence of an ambiguous linkage between  $\theta_l$  and the factors contributing to the cloud break-up and dissipation.

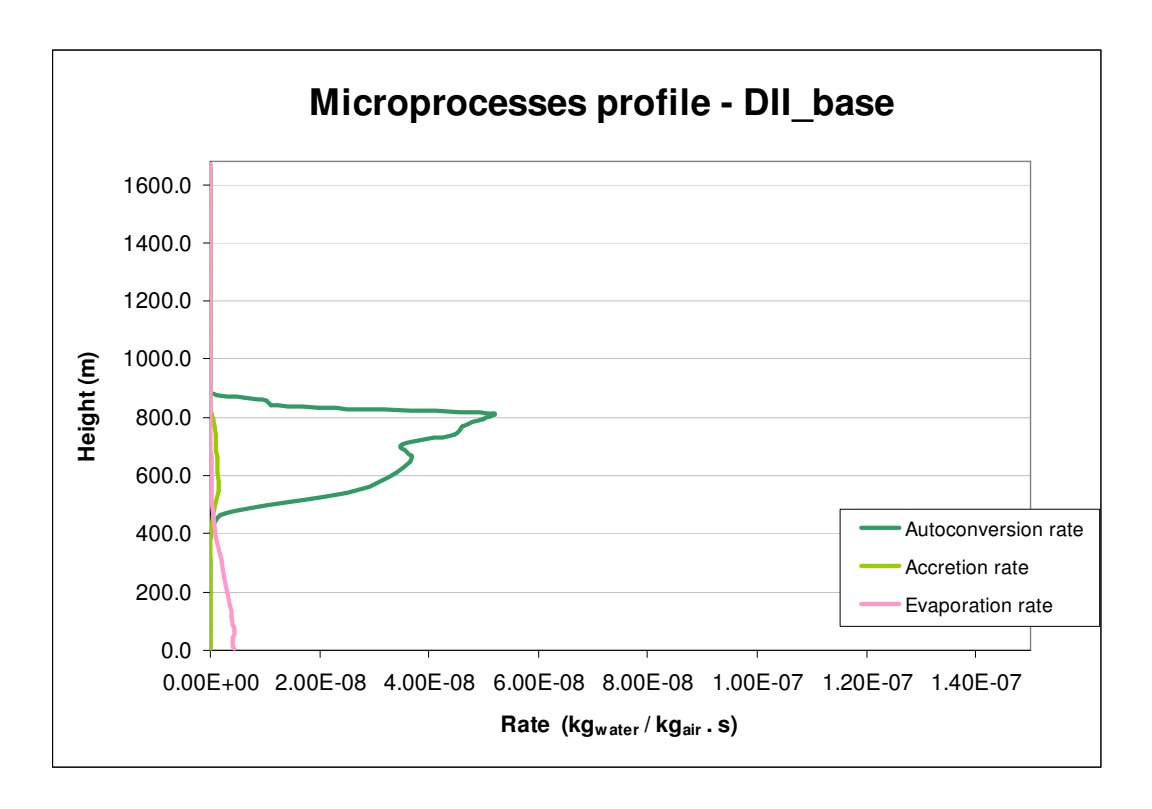


**Figure 6**: The profiles for autoconversion, accretion and evaporation indicate considerably higher rates of autoconversion compared to accretion and evaporation as presented here for the DII\_base simulation. This result is observable for all the sensitivity simulations (see Appendix E) and suggests that this may be one of the possible causes of cloud dissipation and break-up in the ABL. It remains to be said that since a modified autoconversion rate (as in the Kessler1 and Kessler2 tests) still did not reduce the dissipation, the evaporation process appears to be another likely source of the problem.

This ambiguity can be further narrowed because we already know that autoconversion and accretion are both positive contributors and evaporation is a negative contributor to the  $\theta_l$  source term from equation (17). Furthermore, evident from observing Figure 6, the autoconversion rate is much greater than the accretion rate, however the modification of autoconversion for the Kessler1 and Kessler2 tests did not yield any unique results in terms of the  $\theta_l$  profile (see Figure 5).

Based on these observations, the effect of modifying the accretion rate is unnecessary and what remains are the significantly low evaporation rates in the DII-series simulations; marking another possible contributor to the break-up and dissipation of the stratocumulus cloud structure.

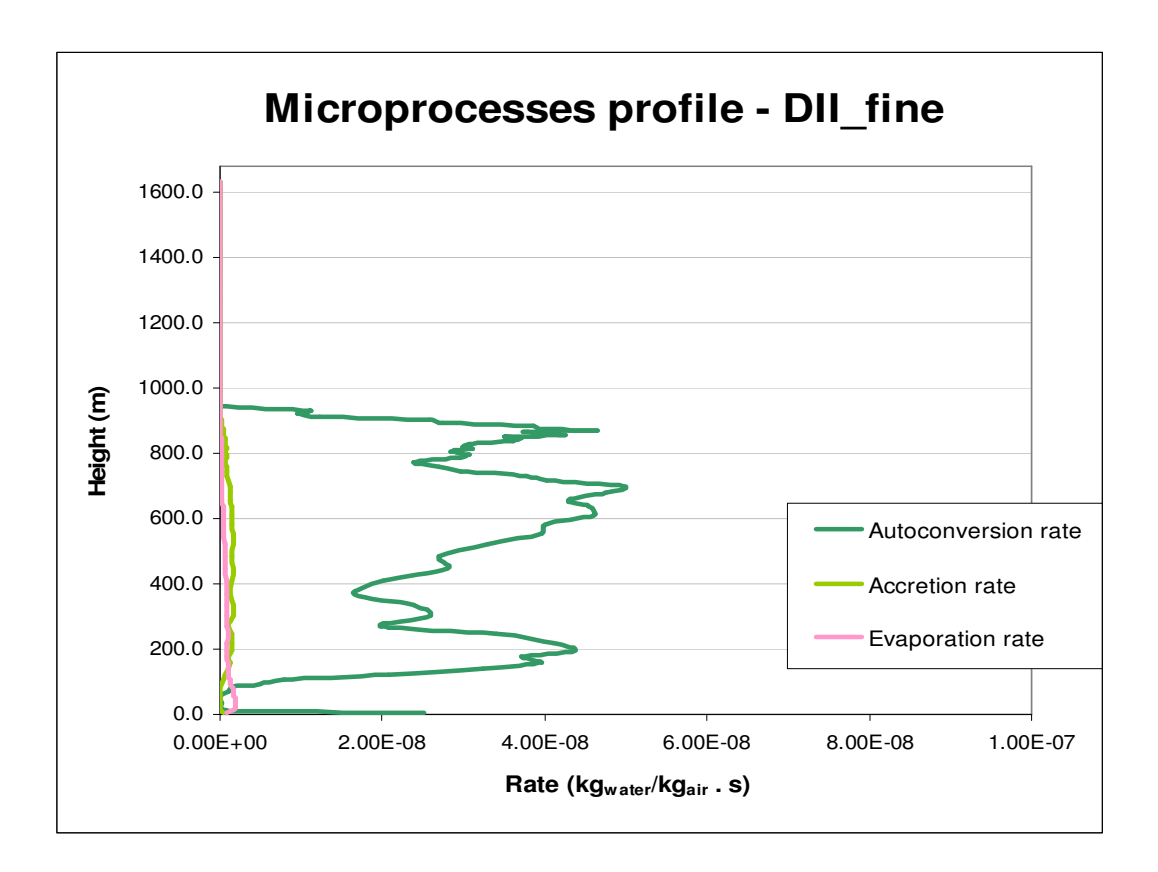


**Figure 7**: The DII\_fine, high resolution simulation profiles for autoconversion, accretion and evaporation (the finer resolution simulation) reinforce the analysis conducted on DII\_base and similarly identify the disproportionately low rate of evaporation in comparison to autoconversion. In DII\_fine, autoconversion occurs at levels in the range of DII\_base but over a greater vertical distance and a negligible evaporation rate.

From Figure 6 there is evidence of a disproportionate rate of autoconversion to accretion and evaporation during the base and sensitivity simulations (see Appendix E). Significantly, the high resolution simulation, DII\_fine, (see Figure 7) yielded an almost negligible evaporation rate and similar maximum levels of autoconversion across a greater vertical portion of the domain in comparison to DII\_base, further reinforcing our analysis of Figure 6. Granted this information, cooling of the boundary layer due to the

process of evaporation is in fact very low compared to the increase of  $\theta_l$  from the autoconversion process. This may contribute to the temporal increase in  $\theta_l$ , observed during the DII-series simulations; the actual extent of this contribution remains ambiguous

## 5.3.2 Statistical profile - $q_t$

The vertical profile of the total water mixing ratio,  $q_t$ , (see Figure 8) has allowed us to determine the mean presence of water over the vertical axis of the ABL domain.

# Statistical profile - q<sub>t</sub>

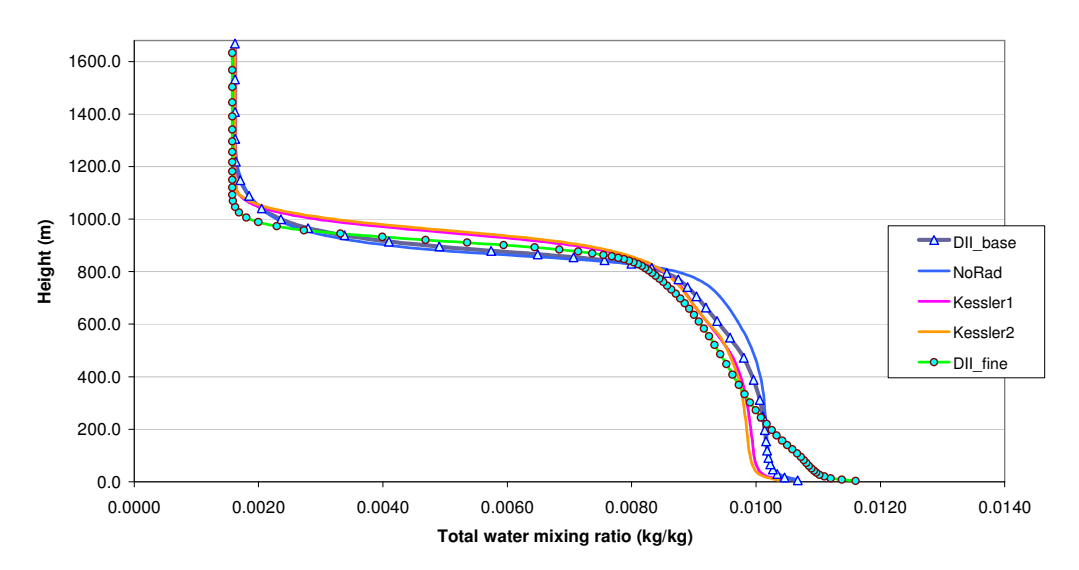


**Figure 8:** The time averaged statistical profile for the total water mixing ratio identifies an inversion close to the initial inversion height of 840m for each of the simulations. This provides preliminary evidence that entrainment did not take place during the simulation; and a phenomenon that is not in agreement with results from the DYCOMS-II LES contributions.

The primary use of this profile is to determine the location of the inversion identified by the rapid change in  $q_t$ . Determining the location of the inversion and other variations in total water mixing ratio is important to interpret the micro-processes incorporated into the cloud microphysics scheme, particularly in quantifying the time averaged effect of entrainment on cloud cover and on the distribution of water along the vertical axis of the boundary layer.

The location of the inversion, identified using  $\theta_l$  profile in Figure 5 and the  $q_t$  profile in Figure 8, reveals an interesting result in relation to the entrainment rate observed during the tests. The initial conditions establish an inversion at the height of 840m and the statistical profile data for  $\theta_l$  and  $q_t$  indicate a time averaged inversion height not too dissimilar to the initial inversion height. This indicates an entrainment rate that could be considered negligible; contrary to results obtained for the DYCOMS-II LES contributions.

The statistical profile for  $q_t$  is in closer agreement to the observed and initial  $q_t$  profiles in Stevens et al. (2004). The NoRad test appears to retain a more curved  $q_t$  profile than the remaining simulation profiles that flatten out to a linearly increasing profile at an altitude between 400m and 800m. This indicates that the presence of a long-wave cooling scheme in the DII\_base, Kessler1 and Kessler2 simulations may have induced increased levels of precipitation and a subsequent decrease in  $q_t$  within the boundary layer based on the negative relationship between the  $q_t$  and  $q_r$  source terms (See equation 15 and 16).

The DII\_fine simulation produced an almost linear  $q_t$  profile up to the inversion, further suggesting a flattening due to an increased  $q_r$  as a consequence of radiative cooling; the reason as to why the linear profile extends from the sea surface could be explained by the thicker cloud layer and lower cloud base observed during the simulation as depicted in Figure 9.

## 5.3.3 Statistical profile - q<sub>l</sub>

The cloud liquid water mixing ratio,  $q_l$ , profile in Figure 9 provides a clear indication of the cloud structure, composition and a means to identify the location of the cloud canopy and cloud base. The cloud canopy is generally located at an altitude just below the inversion and the analysis of the inversion height coupled with the  $q_l$  profile

for each test can help determine whether or not the observed dissipation and cloud break-up may have been related to entrainment. A comparison of the base and sensitivity simulation results has also been conducted and validated with the results produced by the DYCOMS-II LES collaborations in Stevens et al. (2004) to determine the reliability of the model variations tested for the DII-series simulations.

# Statistical profile - q

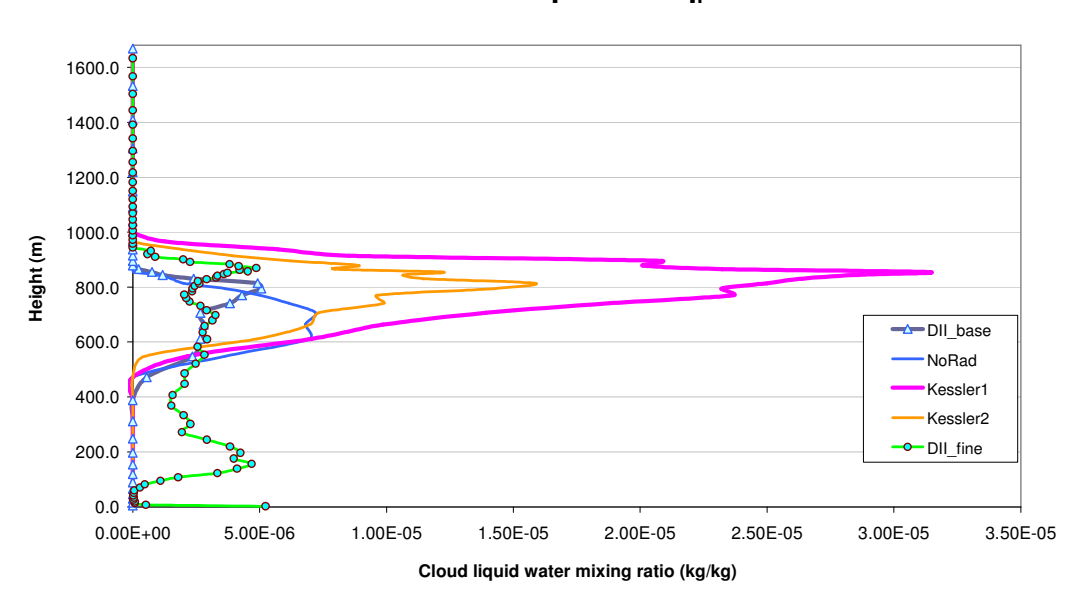


**Figure 9**: The q<sub>1</sub> profile provides valuable information about cloud structure and composition. The profile can also be used to map the cloud canopy, base and cloud layer thickness. The Kessler1 and Kessler2 simulations generate the highest values of q<sub>1</sub>, however these are still far less than those generated in the DYCOMS-II LES simulations as indicated in Stevens et al. (2004). The DII\_fine high resolution simulation yielded a cloud structure, evident from the q<sub>1</sub> profile extending from approximately 100m to 900m yet dissipation in the cloud structure is still prevalent. The removal of long-wave radiative cooling also increased the levels of q<sub>1</sub> in comparison to the base simulation.

The cloud liquid water mixing ratio provides a far deeper insight into the nature of the cloud microphysics models we have used for the base and sensitivity simulations. The cloud cover analysis in section 5.1 is substantiated with the  $q_1$  profiles of each of the five model variants tested. Of particular significance is the considerable broken cloud structure observed in the DII\_base simulation and the comparably lower  $q_1$ 

statistical profile generated over the final hour of the simulation. This profile does not agree with the results generated by Stevens et al. (2004) as there are significantly lower levels of  $q_l$ , somewhere in the order of 50 times less, generated within DII\_base; we can identify only an maximum  $q_l$  of only 0.00507g/kg as opposed to 0.24 g/kg in the results from the DYCOMS-II LES collaborations.

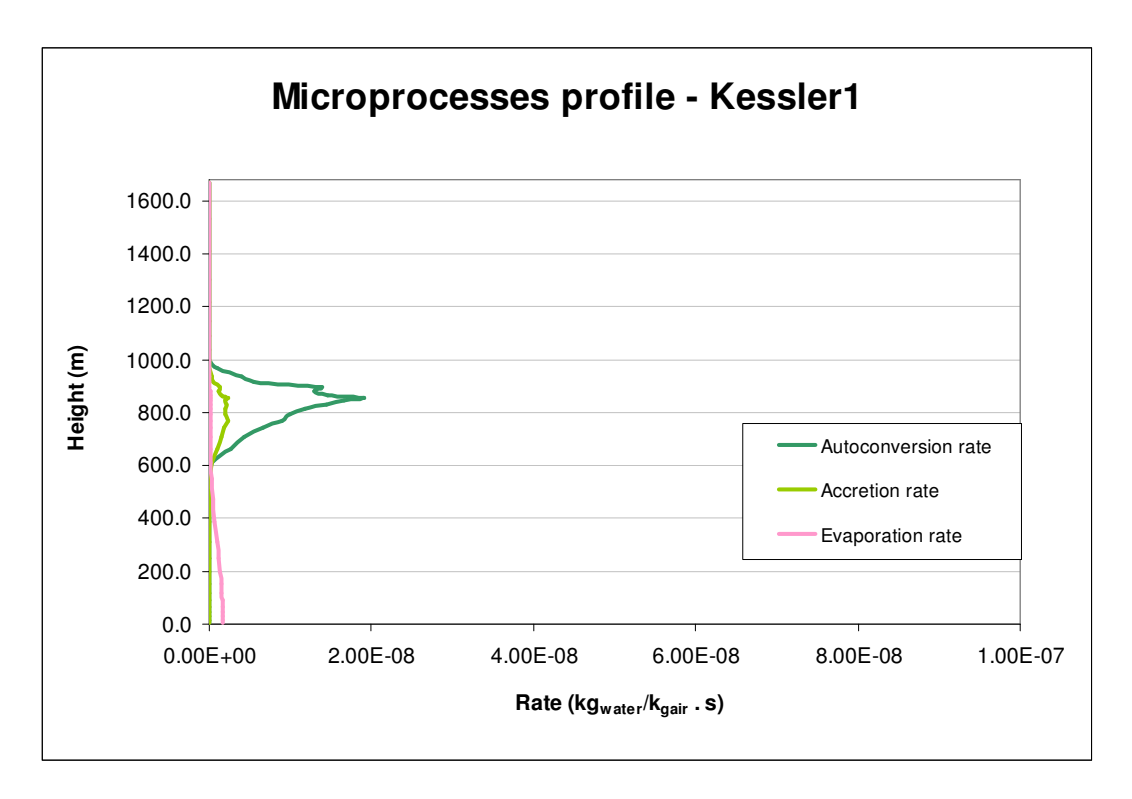


Figure 10: The time averaged profile of the Kessler1 sensitivity simulation again indicates a high autoconversion rate in comparison to the evaporation and accretion micro-processes. The autoconversion rate generated in Kessler1 is dwarfed when compared to the statistical micro-process profiles of DII\_base and DII\_fine in Figures 6 and 7 respectively. It is the reduced autoconversion rate that can be attributed to the larger cumulus cloud structures observable for a longer period of time within the domain.

The exclusion of radiative forcings in the NoRad sensitivity simulation made only a slight improvement to the  $q_1$  profile, however this provided evidence only to settle any skepticism regarding the role of the radiation model in causing the unreasonably high levels of cloud dissipation or break-up observed during the final hour of the simulations. The implementation of Kessler's autoconversion parameterization

yielded more promising results. With the results generated from Kessler1, a far greater  $q_l$  profile is observed in comparison to DII\_base, with a maximum of 0.0313g/kg; this would suggest that the microphysics scheme proposed by Wyant et al. (1997) is another possible source of the stratocumulus break-up and dissipation occurring after the first hour of simulations. However the maximum  $q_l$  obtained from Kessler1 is still a considerably lower value than the average maximum recorded during the DYCOMS-II research flights of 0.7 g/kg.

The modification of the microphysics scheme using Kessler's autoconversion parameterisation made a considerable improvement to the q<sub>1</sub> profile. The improvement in the levels of q<sub>1</sub> observed in the Kessler1 and to a lesser extent, the Kessler2 sensitivity simulations are explained by the considerably lower autoconversion rates generated in comparison to the base simulation (See Figure 10). However as previously mentioned, the modification of the autoconversion parameterisation only had a temporary effect on maintaining larger cloud formations as dissipation and break-up were still prevalent in the Kessler1 and Kessler2 simulations toward the latter stages of the tests. The maximum observed q<sub>1</sub> was also still far lower than the average maximum recorded during the DYCOMS-II research flights and results generated in the DYCOMS-II LES contributions. Furthermore, the Kessler2 sensitivity simulation had a threshold constant higher than that used for the Kessler1 autoconversion parameterization, yet differences in cloud dissipation and break-up were almost indiscernible between the two simulations. Counter-intuitively, increasing the threshold value in the Kessler2 simulation acted to reduce the levels of q<sub>1</sub> within the ABL during the simulation; this was besides the fact that the recorded maximum mean autoconversion rate was 3.5 times lower than in the DII base simulation.

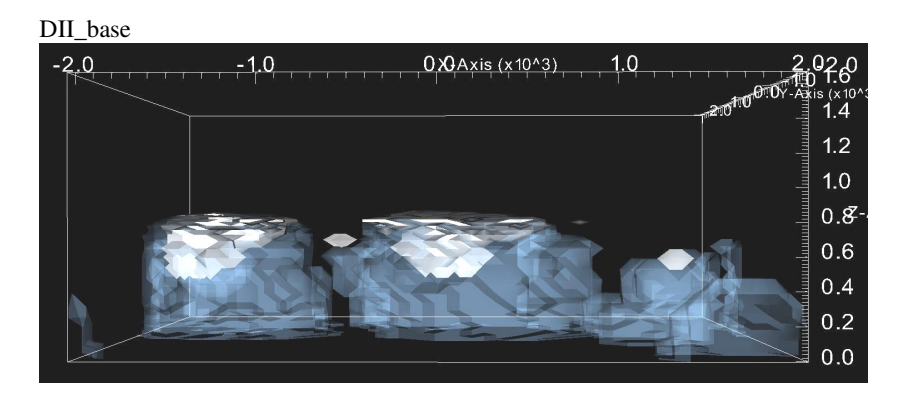
The simplicity of the autoconversion parameterization (Equation L3) ensures the mitigation of implementation issues, furthermore, the threshold constant used in

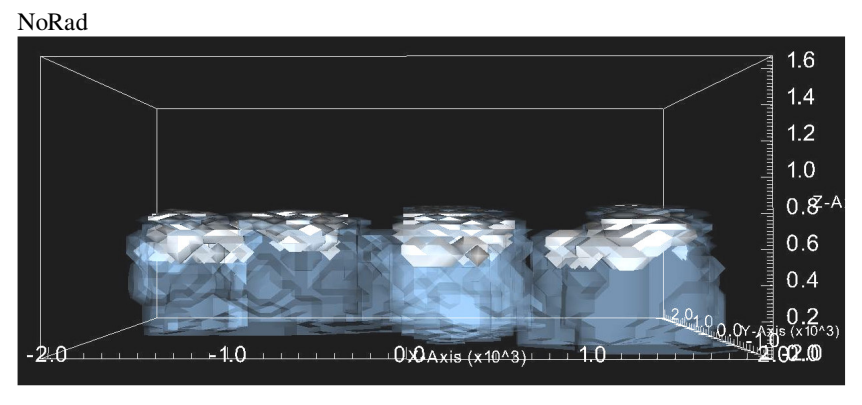
Kessler1 has been established from empirical testing (Thompson et al., 2004) and changing this value to yield more desirable results without any empirical or scientific substantiation can not be justified; therefore although higher levels of q<sub>1</sub> are demonstrated in the Kessler1 and Kessler2 simulations, the modification of the autoconversion parameterization can not on its own provide us with a reliable and accurate microphysics scheme. The DII\_fine simulation generated a q<sub>1</sub> profile that fell within in the range of the DII\_base values, but over a greater vertical distance indicating greater cloud depth and volume. This in itself shows that adequate resolution is critical for reliably simulating the ABL, however it also goes so far as to indicates the likely increase in cloud cover and volume within the boundary layer for the NoRad, Kessler1 and Kessler2 models provided they are tested within a finer resolution domain.

## 5.4 Cloud structure and precipitation

The analysis of the cloud structures is necessary to compare results with data made available from the DYCOMS-II flights. This presents the opportunity to compare the DII-series simulation results with the actual observed atmospheric data provided in Stevens et al. (2002). The mean cloud thickness calculated from the DYCOMS-II flight data summary is 366m.

The cloud thickness observed at the end of the base simulation (time = 2 hours) was approximately 394m apparent through a simple observation of Figure 11 and more accurately validated with the data from the cloud liquid water mixing ratio profile in Figure 9 and Appendix E. This figure falls within the maximum and minimum cloud thickness range of 510m and 265 respectively, recorded during the DYCOMS-II flights. Similarly, NoRad and Kessler1 also generate cloud systems within the DYCOMS-II thickness range.





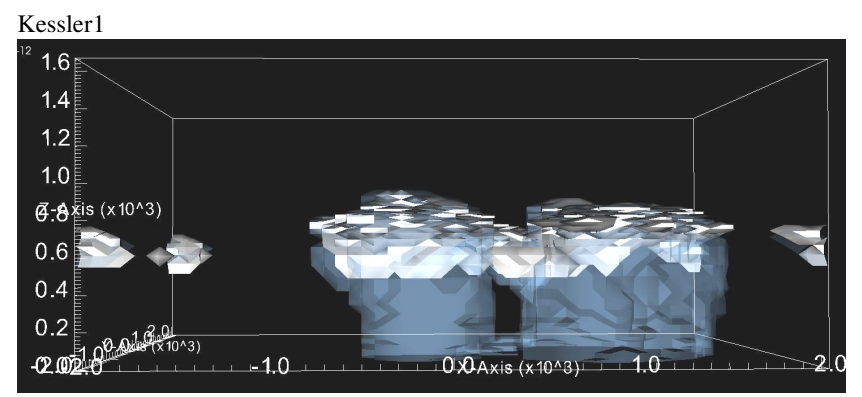


**Figure 11:** The cloud thickness, canopy and base at t = 2 hours are compared with the DYCOMS-II flight summary in Stevens et al. (2002) to identify any points of similarity between the DII-series simulations and the DYCOMS-II flight data.

The isolated cumulus clouds appear to have to retained elements of the cloud structure and as such there were no obvious signs of thinning; however the break-up and dissipation of the cloud formations are still particularly evident in Figure 11.

The precipitation seen in blue includes all values of  $q_r$  even encompassing values lower than 0.001 g/kg, this is particularly useful in visualizing the entire range of hydrometeor precipitation. It also provides a visual reference to assess the magnitude of

the autoconversion rate in comparison to the uncharacteristically low evaporation rates. Using Figure 11 as a guide, a key assessment can be made regarding the reasons behind the low evaporation rates discussed in section 5.3.1. Figure 12 presents the statistical profile of relative humidity along the height of the domain.

### Statistical profile - Relative Humidity

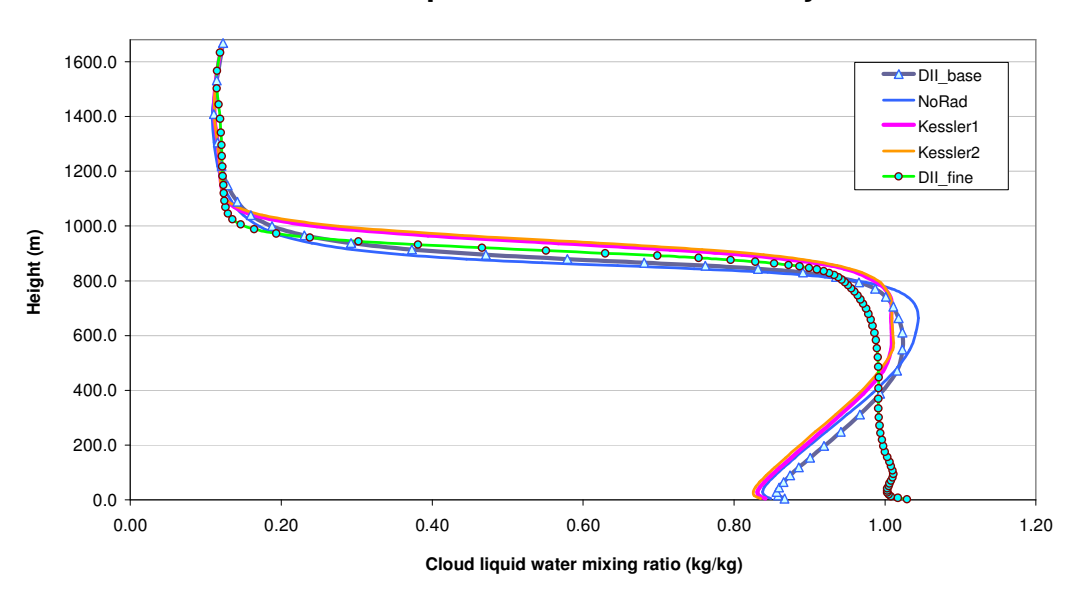


**Figure 12:** The time averaged relative humidity levels are recorded along the height of the boundary layer during the final hour of the simulation. There is ample evidence to suggest that the humidity levels during the final hour of the simulations are quite high and can offer some explanation regarding the lower observed evaporation rates.

Considering only the results from DII\_fine, we can see that relative humidity is close to 100 per cent right up to the height of the inversion. A distinct assumption made for the evaporation parameterization in equation (13) is that evaporation can not occur in regions of the boundary layer where relative humidity is unity; and as evident in figure 12 the relative humidity may be too high in many regions of the boundary layer to allow any kind of evaporation to take place.

The final point worthy of discussion is the height of the cloud canopy which is required in order to drive a complete analysis of the observations relating to temporal inversion height variation and thus the entrainment. Data collected from the DYCOMS-II research flights show a minimum and maximum canopy altitude of 600m and 1075m.

Figure 11 depict cloud tops of the selected simulations within this range. By looking at Figure 9 and the profile data for q<sub>I</sub>, we can locate the maximum height of the cloud tops to be located at 866m, 855m and 966m for DII\_base, NoRad and Kessler1 simulations respectively. We can also identify here that the cloud tops of DII\_base and NoRad are located at an altitude that just touches the inversion and Kessler1 penetrates past the inversion. This will be particularly useful for the discussion of entrainment in the next section.

### 5.5 Temporal inversion height variation and entrainment

There is almost no observable change in inversion height during the base and sensitivity simulations evident as graphed in Figure 13. Consequently the entrainment rate, computed as the rate of change of the inversion height over time is negligible. Since entrainment rate is effectively zero and considering the discussion in section 4.3.1 regarding the dissipative effects of entrainment on cloud structures, we can somewhat eliminate entrainment as the likely cause of the observed cloud break-up and dissipation during the DII-series simulations.

This is not in accordance to the results presented by Stevens et al., where entrainment was observed in both coarse and finer resolution simulations. As discussed in Stevens et al. (2004), there was evidence of reduced entrainment in the high resolution simulations however there was no discernible difference between the temporal variation in inversion height for the DII\_fine sensitivity simulation and the other DII-series tests conducted. Based on the difference in entrainment results between the DII-series simulations and the DYCOMS-II LES contributions, we can postulate that there may be a fundamental issue explicitly linked to the implementation of the cloud microphysics scheme within PUFFIN-ABL.

### **Temporal inversion height variation**

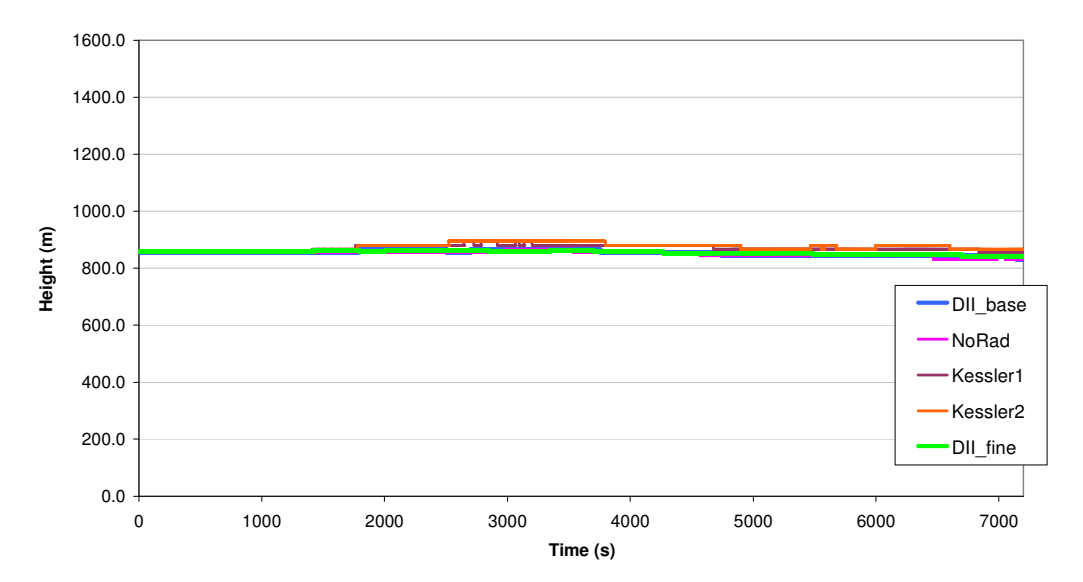


**Figure 13:** The temporal inversion height variation is used to directly compute the entrainment rate. Something overtly evident is that the entrainment rate can be approximated to zero since no distinct visible increase in the altitude of the inversion is observable. This can be used to cancel out any possible links between entrainment and the high levels of cloud dissipation and break-up observed during the simulations. Based on the fact that entrainment is observed in the DYCOMS-II LES simulations, we can suggest the models used for the DII-series simulations may not be reliable enough; an issue relating to the implementation of the microphysics scheme.

# 5.6 Third moment of vertical velocity profile statistic, $< w^{3} >$

The statistical profiles of the third moment of w, indicate that there is a great deal of downdraft occurring in the lower portion of the boundary layer in the simulations (see Figure 14). This can be explained by the downward velocity caused by the heavy drizzle and rainfall observed in the simulations; this turbulent motion appears to settle above the inversion. The  $< w'^3 >$  profiles presented in Stevens et al (2004) show a wide range of results, from profiles that show evidence of only updrafts identified by mostly positive values of  $< w'^3 >$  to the downdrafts generated within the UCLA-0 simulation. The DII-series simulations have generated profiles of mostly negative  $< w'^3 >$  values which may be explained only by the high levels of precipitation observed during the simulations.

# Statistical Profile - <w<sup>3</sup>>

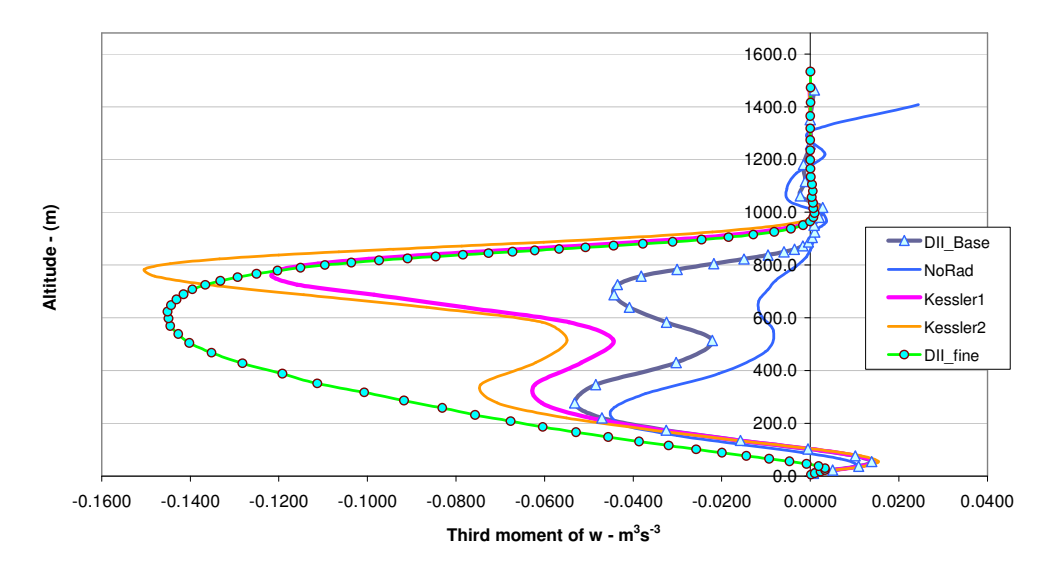


**Figure 14:** The  $< w'^3 >$  profiles indicate that heavy downdrafts were mostly present during the simulations; likely to be a result of precipitation. The DII\_fine profile also closely matches the profile generated by UCLA-0 in the DYCOMS-II LES master ensemble and indicates a requirement of simulations with a finer grid resolution to generate more reliable simulation statistics.

Furthermore, the  $\langle w'^3 \rangle$  profile values produced by Kessler1, Kessler2 and DII\_fine come close to the maximum values of approximately  $\pm 1.2 m^3 s^{-3}$  generated by the DYCOMS-II LES simulations. The DII\_fine simulation generates a  $\langle w'^3 \rangle$  profile that more closely resembles the profile generated by the UCLA-0 DYCOMS-II contribution; both with a maximum negative value observed at a height of 600m. The single difference between DII\_base and DII\_fine is the finer grid resolution, however this alone has been sufficient to generate a maximum value in DII\_fine in the order of 3.5 times larger than in DII\_base. Such a drastic variance in results simply due to the use of a finer grid resolution suggests that coarse resolution simulations may not be adequately reliable in the simulation and analyses of the clout topped ABL.

## 6. CONCLUSION

It is evident from the DII-series simulations results that we have successfully managed to simulate clouds and precipitation within the marine nocturnal boundary layer. Having said that, we have also encountered a problem relating to the implementation of the microphysics scheme; this has of course affected the accuracy of the results generated. This is not a great concern because the primary focus of this thesis was to have a working microphysics model integrated into PUFFIN-ABL in order to simulate the atmospheric boundary layer; the secondary objective of having an accurate and reliable microphysics scheme can easily be achieved through subsequent improvements based on the results presented in this thesis.

Briefly considering the radiation model, it was established from the NoRad sensitivity simulation that long-wave radiative forcings only made a minor contribution to the overall outcome of the simulations; having the effect of simultaneously increasing autoconversion and the cloud liquid water mixing ratio present in the boundary layer. The incorporation of a radiation model was absolutely necessary to be able to reliably compare our results with the DYCOMS-II LES contributions and the DYCOMS-II research flights.

From the visualisations generated during the simulation, it was apparent that there was a considerable level of cloud break-up and dissipation taking place during the final hour of the simulations. The most likely reasons for this were identified to be the disproportionately high autoconversion rates, the almost negligible evaporation rates, the use of a coarse grid resolution domain and of course, problems with the actual implementation of the microphysics scheme.

The statistical profiles of  $\theta_l$ ,  $q_t$  and  $q_l$  provided us with detailed information regarding the likely factors contributing to the dissipation and break-up of the stratocumulus cloud layer. Although the results indicated that the problem was to some

extent associated with the autoconversion and evaporation micro-processes, testing of modified microphysics schemes in the Kessler1 and Kessler2 sensitivity simulations still produced results that showed considerable cloud break-up and dissipation. Indeed there was a marked increase in the cloud liquid water mixing ratio during final hour of the simulations and the cloud structures did remain larger for a longer period of time, however this could not substantiate the assertion, that the dissipation of the cloud layer was solely linked to the chosen parameterizations of the micro-processes.

The DII\_fine simulation conducted within the finer grid resolution domain provided an invaluable insight into the absolute necessity of high resolution simulations to yield accurate results. It proved that there was a noticeable compromise in the reliability of the coarse resolution simulations, DII\_base, NoRad, Kessler1 and Kessler2, once the results were compared with those generated by the DII\_fine simulation. With the high resolution simulation, cloud volume was shown to increase (see Figure 9), a significantly lower liquid water potential temperature profile was observed (see Figure 5) and a  $< w^{13} >$  profile was generated that was in close resemblance to the UCLA-0 DYCOMS-II contribution; this was a significant improvement in accuracy in comparison to the base simulation.

Considering everything mentioned above, one would then go on to suggest that the issue of cloud dissipation and break-up could be resolved by designing a microphysics scheme incorporating Kessler's more successful autoconversion parameterisation simulated within a finer grid resolution domain. This attempt may prove to be futile, simply because the simulation modifications mentioned were both subject to cloud break-up and dissipation during the final hour of simulations; combining the two would not eliminate the source of the problem.

The problem appears to lie in the implementation of the microphysics scheme. For one, the DII-series simulations were all subject to the same dissipative forces,

meaning that any modifications only contributed to a temporary improvement in the cloud structures during the simulations; evidently there was something forcing the simulations to generate the observed isolated cumulus clouds. More importantly, as we discussed in the results, there was no evidence of entrainment in any of the DII-series simulations; the results were almost entirely identical. This occurred despite the large variations in the results observed in the statistical profiles, indicating that the microphysics model had very little effect on processes occurring within the boundary layer.

Stevens et al. (2004) meticulously deal with entrainment since it is a geophysical phenomenon that is readily observable yet difficult to understand and model. Since entrainment was not observed in the DII-series simulations we can only postulate that the implementation of the microphysics scheme must be revisited in order to ensure that the microphysics scheme can adequately influence geophysical processes including entrainment within the boundary layer.

The research conducted in this thesis has been directed at expanding the capabilities of PUFFIN-ABL as an atmospheric research platform. The implementation of a cloud microphysics scheme and a simple long-wave radiation model has been successful, however further modifications are required to improve the reliability and accuracy of the simulations. The primary objective of this thesis in integrating a fast and reliable cloud microphysics scheme into PUFFIN-ABL has been achieved and from here, further progress can be made to develop and simulate far more accurate cloud and radiation models for the purposes of atmospheric and climate research.

### REFERENCES

- Austin, P., Y. Wang, R. Pincus and V. Kujala, 1995: Precipitation in stratocumulus cloud: Observational and modelling results, *Journal of the Atmospheric Sciences*, **52**, 2329-2352
- Baker, M.B., 1993: Variability in concentrations of cloud concentration nuclei in the marine cloud-topped boundary layer, *Tellus*, **45B**, 458-472
- Chen, C., and W.R. Cotton, 1987: The physics of marine stratocumulus-capped mixed layer, *Journal of the Atmospheric Sciences*, 44, 2951-2977
- Costa, A.A., Almeida, G.P., 2000: A bin-microphysics cloud model with high-order positive-definite advection, Atmospheric Research, 55, 225-255
- Harrington, J.Y. and Olsson, P.Q., 2001: A method for the parameterization of cloud optical properties in bulk and bin microphysical models. Implications for arctic cloudy boundary layers, *Atmospheric Research*, 57, 51-80
- Herman, G. and Goody, R., 1976: Formation and Persistence of Summertime Arctic Stratus Clouds, Journal of the Atmospheric Sciences, 33, 1537-1553
- Kessler, E. 1969: On the Distribution and Continuity of Water Substance in Atmospheric Circulations, Meteorological Monograph, 10(32), 88pp
- Khairoutdinov, M.F. and Kogan, Y.L., 1999: A large eddy simulation model with explicit microphysics: Validation against aircraft observations of a stratocumulus-topped boundary layer, *Journal of the Atmospheric Sciences*, **56**, 2115-2131
- Kinzer, G.D. and Gunn, R., 1951: The evaporation, temperature and thermal relaxation-time of freely falling waterdrops, *Journal of Meteorology*, **8(2)**, 71-83
- Kogan, Y.L, 1991: The simulation of a convective cloud in a 3-D model with explicit microphysics. Part I: Model Description and Sensitivity Experiments, *Journal of the Atmospheric Sciences*, 48(9), 1160-1189
- Liou, K. and Ou S., 1989: The role of cloud microphysical processes in climate: An assessment from a one-dimensional perspective, *Journal of Geophysical Research*, 94(D6), 8599-8607
- Liu, J.Y. and Orville, H.D., 1969: Numerical modelling of precipitation and cloud shadow effects on mountain induced cumuli, *Journal of the Atmospheric Sciences*, **26**, 1283-1289
- Marshall, J.S. and Palmer W. McK., 1948: The Distribution of Raindrops with size, *Journal of Meteorology*, 5, 165-166
- Roach., W.T. and A. Slingo, 1979: A high resolution infrared radiative transfer scheme to study the interaction of radiation with cloud, *Quarterly Journal of the Royal Meteorological Society*, 105, 603-614
- Rogers, R.R., 1979: A Short Course in Cloud Physics, Pergamon Press, Oxford, 235 pp.
- Rogers, R.R. and M.K. Yau, 1989: A Short Course in Cloud Physics 3d ed., Pergamon Press, 293 pp.
- Seifert, A., Khain, A., Pokrovsky, A., Beheng, K.D., 2006: A comparison of spectral bin and two-moment bulk mixed-phase cloud microphysics, *Atmospheric research*, **80**, 46-66
- Spilhaus, A.F., 1948: Raindrop size, shape and falling speed, Journal of Meteorology, 5, 108-110

- Stevens et al. 2002: Dynamics and Chemistry of Marine Stratocumulus DYCOMS -II, Bulletin of the American Meteorological Society
- Stevens et al. 2005: Evaluation of Large-Eddy Simulations via Observations of Nocturnal Marine Stratocumulus, *Monthly Weather Review*
- Sundqvist, H., 1978: A parameterization scheme for non-convective condensation including prediction of cloud water content, *Quarterly Journal of the Royal Meteorological Society*, **104(441)**, 677-690
- Thompson, G., Rasmussen, R.M. and K. Manning, 2004: Explicit Forecasts of Winter Precipitation Using an Improved Bulk Microphysics Scheme. Part I: Description and Sensitivity Analysis, *Monthly Weather Review*, **132**, 519-542
- Walko, R.L., Cotton, W.R., Meyers, M.P. and J.Y. Harrington, 1995: New RAMS cloud microphysics parameterization Part I: the single-moment scheme, *Atmospheric Research*, **38**, 29-62
- Wyant, M.C., Bretherton, C.S., Rand, H.A. and Stevens, D.E., 1997: Numerical Simulations and a Conceptual Model of the Stratocumulus to Trade Cumulus Transition, *Journal of Atmospheric Sciences*, **54**, 168-192

### APPENDIX A

### Microphysics source code – Fortran 90

```
! T: temperature
do n = 1.5
do k = kg1,kg2; do j = jg1, jg2; do i = ig1, ig2
   T(i,j,k) = (h(i,j,k) + h_0(k)) * Exner(k) + Lv * q_l(i,j,k) / Cp
end do; end do; end do;
! e_s: computes saturation water vapour pressure
end do; end do; end do
! q_s: computes saturation vapour mixing ratio
do k = kg1,kg2; do j = jg1, jg2; do i = ig1, ig2
   q_s(i,j,k) = Rgas/Rv * (e_s(i,j,k)) / (p_0(k)+p_1(k))
end do; end do; end do
! q_I: computes cloud liquid water mixing ratio
do k = kg1,kg2; do j = jg1, jg2; do i = ig1, ig2
   IF (c(i,j,k) > q_s(i,j,k)) THEN
       q_l(i,j,k) = c(i,j,k) - q_s(i,j,k)
   ELSE
        q_l(i,j,k) = 0.0
   END IF
end do; end do; end do
end do
! calculate h 2 which is perturbation of virtual potential temp. required for buoyancy term
do k = kg1,kg2; do j = jg1, jg2; do i = ig1, ig2  h\_2(i,j,k) = ( \ T(i,j,k) \ ^* \ ( \ 1.0 + 0.608 \ ^* c(i,j,k) \ ) \ - \ (t\_v\_1(k) + t\_v\_0(k)) \ ) \ / \ Exner(k) 
end do; end do; end do
! c_rw, r_w: Fourth moment drop radius
 \begin{array}{l} \text{do } k = kg1, kg2; \ \text{do } j = jg1, \ jg2; \ \text{do } i = ig1, \ ig2 \\ r\_w(i,j,k) = ( \ ( \ 3.0 \ ^* \ (\text{den}\_0(k) + \text{den}\_1(k)) \ ^* \ q\_l(i,j,k) \ ) \ / \ ( \ 4.0 \ ^* \ N \ ^* \ pi \ ^* \ \text{den}\_w \ ) \ )^{**}(1.0/3.0) \ ! \ \text{simplified} \end{array} 
   IF (r_w(i,j,k) >= 10.0e-6) THEN
        c_rw(i,j,k) = 1.0
   ELSE
        c_rw(i,j,k) = (r_w(i,j,k)/10.0e-5)**3
   END IF
end do; end do; end do
```

```
! P1:autoconversion rate - Wyant et al. (1997)
do k = kg1,kg2; do j = jg1, jg2; do i = ig1, ig2 
 P1(i,j,k) = pi * alpha * E1 * C1 * N * r_w(i,j,k)**4.0 * c_rw(i,j,k) * q_v(i,j,k)
end do; end do; end do
! P1:autoconversion rate - Kessler (1969)
do k = kg1,kg2; do j = jg1, jg2; do i = ig1, ig2
   IF (q_l(i,j,k) >= 1.0e-4) THEN
       P1(i,j,k) = 1.0e-3 * (q_l(i,j,k)-1.0e-4)
   ELSE
       \mathsf{P1}(\mathsf{i},\mathsf{j},\mathsf{k})=0
  END IÈ
end do; end do; end do
! r m: free parameter used to determine rainwater component
do k = kg1,kg2; do j = jg1, jg2; do i = ig1, ig2
  r_m(i,j,k) = (((den_0(k)+den_1(k))*max(q_r(i,j,k),0.0))/(8.0*pi*den_w*n0))**0.25
end do; end do; end do
! Fp: precipitation flux
do k = kg1,kg2; do j = jg1, jg2; do i = ig1, ig2
if (r_m(i,j,k) < 600.0e-5) then
if ( r_m(i,j,k) < 40.0e-6 ) then ! I am not sure whether this is correct but it sure helps stabilize it
  Fp(i,j,k) = -4.0 * (den_0(k)+den_1(k)) * C1 * (r_m(i,j,k)**2) * q_r(i,j,k)
 Fp(i,j,k) = -4.0 * (den_0(k)+den_1(k)) * C2 * r_m(i,j,k) * q_r(i,j,k)
 endif
 endif
end do; end do; end do
! P2: accretion rate
do k = kg1,kg2; do j = jg1, jg2; do i = ig1, ig2
  P2(i,j,k) = (-3.0/16.0) * (E2 * Fp(i,j,k) * q_l(i,j,k)) / (den_w * max(r_m(i,j,k),1.0e-20))
end do; end do; end do
! water vapour mixing ratio, q_v = c - q_l
! relative humidity = q_v/q_sat
do k = kg1,kg2; do j = jg1, jg2; do i = ig1, ig2
  if (c(i,j,k) < q_l(i,j,k)) then
     q\_I(i,j,k) = c(i,j,k)
  end if
     q_v(i,j,k) = c(i,j,k) - q_l(i,j,k)
     rh(i,j,k) = q_v(i,j,k)/q_s(i,j,k)
end do; end do; end do
```

```
! A, B: A and B
do k = kg1,kg2; do j = jg1, jg2; do i = ig1, ig2 
 A(i,j,k) = Lv^{**}2.0 / (Ktc * Rv * (T_0(k)+T_1(k))^{**}2.0)
 B(i,j,k) = Rv * (T_0(k)+T_1(k)) / (Dvap * e_s(i,j,k))
end do: end do: end do
! evaporation rate
do k = kg1,kg2; do j = jg1, jg2; do i = ig1, ig2
 IF (rh(i,j,k)<1.0) THEN
      EV(i,j,k) = (8.0 * pi * n0 * (1.0 - rh(i,j,k))) /
               ( (den_0(k)+den_1(k)) * ( A(i,j,k) + B(i,j,k) ) ) * &
( 0.39 * r_m(i,j,k)**3 + 0.40 * ( (den_0(k)+den_1(k)) * C2 / mju )**0.5 * r_m(i,j,k)**3.0 )
 ELSE
      EV(i,j,k) = 0.0
 END IF
end do; end do; end do;
! m_QT: microphysics for total water mixing ratio
\begin{array}{l} do \; k = kg1, kg2; \; do \; j = jg1, \; jg2; \; do \; i = ig1, \; ig2 \\ m\_QT(i,j,k) = -(P1(i,j,k) + P2(i,j,k) - EV(i,j,k)) \end{array}
end do; end do; end do;
! d_fp: differential component of rainwater mixing ratio microphysics
do k = kb1,kb2; do j = jb1, jb2; do i = ib1, ib2
   d_{fp}(i,j,k) = (Fp(i,j,k+1)-Fp(i,j,k-1))/(z(k+1)-z(k-1))
end do; end do; end do
! m_QR: microphysics for rainwater mixing ratio
do k = kb1,kb2; do j = jb1, jb2; do i = ib1, ib2
   m_QR(i,j,k) = -m_QT(i,j,k) - d_fp(i,j,k) / (den_0(k)+den_1(k))
end do; end do; end do;
! m_LWPT: Microphysics for liquid water potential temperature
do k = kb1,kb2; do j = jb1, jb2; do i = ib1, ib2
   m_LWPT(i,j,k) = -Lv / (cp * Exner(k)) * m_QT(i,j,k) !changed from perturbation exner function to Pi_env
end do; end do; end do;
```

```
!-----
```

### ! Cloud liquid water mixing ratio vertical profile

 $\begin{array}{l} ql\_prof = 0 \\ do \ k = kg1,kg2; \ do \ j = jg1, \ jg2; \ do \ i = ig1, \ ig2 \\ ql\_prof(k) = ql\_prof(k) + q\_l(i,j,k)*scell\_area\_u(i,j) \\ end \ do; \ end \ do; \ end \ do \\ do \ k = kg1,kg2 \\ ql\_prof(k) = ql\_prof(k)/dom\_area(3) \\ end \ do \end{array}$ 

#### !-----

### !Total water mixing ratio vertical profile

!-----

```
 \begin{array}{l} qt\_prof = 0 \\ do \ k = kg1,kg2; \ do \ j = jg1, \ jg2; \ do \ i = ig1, \ ig2 \\ qt\_prof(k) = qt\_prof(k) + c(i,j,k)*scell\_area\_u(i,j) \\ end \ do; \ end \ do; \ end \ do \\ do \ k = kg1,kg2 \\ qt\_prof(k) = qt\_prof(k)/dom\_area(3) \\ end \ do \\ \end{array}
```

## Radiative cooling source code – Fortran 90

```
! code to convert W/m^2 to puffin parameter
do k = kg1,kg2; do j = jg1, jg2; do i = ig1, ig2
          g_{w(i,j,k)} = scell_area_u(i,j) / (Cp^*(den_0(k)+den_1(k)))
end do; end do; end do
! code to find inversion using total water mixing ratio
do k = kb1,kb2
   if (at prof(k)>0.) then
    if (qt_prof(k)< 0.008) exit
end do
z_z = k
! Cooling in the free troposphere just above cloud top (inversion)
do k = kmin, kmax-1; do j = jmin, jmax; do i = imin, imax
     F_{free}(i,j,k) = rho_i * Dval * Cp * ((z(k+1)-z(z_z))**(4/3))/4. &
            + (z(z_z) * (((z(k+1) - z(z_z))**(1/3))))
    if (k > kmin) su_ab(i,j,k) = su_ab(i,j,k) - F_free(i,j,k) * g_lw(i,j,k)
    if (k < kmax-1) su_ab(i,j,k+1) = su_ab(i,j,k+1) + F_free(i,j,k) * g_lw(i,j,k)
end do; end do; end do
! cloud top cooling
do k = kmin, kmax-1; do j = jmin, jmax; do i = imin, imax
      q_{int}(i,j,k) = kval * SUM((den_0(k+1:kmax) + den_1(k+1:kmax)) * q_i(i,j,k+1:kmax) * sud(k+1:kmax))
      cl_{top}(i,j,k) = F_0 * exp(-q_int(i,j,k))
      if (k > kmin) su_ab(i,j,k) = su_ab(i,j,k) - cl_top(i,j,k) * g_lw(i,j,k)
       \text{if } (k < kmax-1) \ su\_ab(i,j,k+1) = su\_ab(i,j,k+1) + cl\_top(i,j,k) \ ^* \ g\_lw(i,j,k) \\ 
end do; end do; end do
! cloud base warming
do k = kmin, kmax-1; do j = jmin, jmax; do i = imin, imax
      q_int(i,j,k) = kval * SUM((den_0(kmin:k) + den_1(kmin:k)) * q_l(i,j,kmin:k) * sud(kmin:k))
      cl_base(i,j,k) = F_1 * exp(-q_int(i,j,k))
      if (k > kmin) su ab(i,j,k) = su ab(i,j,k) - cl base(i,j,k) * g lw(i,j,k)
      if (k < kmax-1) su_ab(i,j,k+1) = su_ab(i,j,k+1) + cl_base(i,j,k) * g_lw(i,j,k)
end do; end do; end do
```

### APPENDIX B

### Friction Velocity - u\*

Given the dimensionless surface drag coefficient  $C_D$  and the resultant geostrophic wind velocity flowing in the northerly and easterly directions we can determine the parameter used in the PUFFIN input file  $u_*$ .

- Surface drag coefficient:  $C_D = 0.0011$
- Geostrophic wind flowing in easterly direction:  $U_G = 7 \text{ ms}^{-1}$
- Geostrophic wind flowing in northerly direction:  $V_G = -5.5 \text{ ms}^{-1}$

$$u_* = \left(\frac{1}{2}C_D \mid U_G + V_G \mid^2\right)^{1/2} = 0.209 ms^{-1}$$

#### Surface Heat Flux into domain − θ\*u\* K.m/s

The surface sensible heat flux through the bottom boundary can be transformed into the input variables used by the PUFFIN input file using the following relation:

$$u_*\theta_* = \frac{Q'_s}{\rho c_p} K.ms^{-1}$$

Where  $c_p = 1.015 \text{ kJ.kg}^{-1}\text{K}^{-1}$  and  $\rho = 1.22 \text{ kg.m}^{-3}$ .

#### **Surface Moisture Flux into domain – c\*u\*** kg/kg.m/s

In a similar fashion we can solve the latent heat flux used by Stevens et al. (2004) to determine the surface moisture flux into the domain in the PUFFIN input file dimensions.

$$u_*c_* = \frac{Q_L'}{\rho L_v} kg / kg.ms^{-1}$$

By substituting the value  $L_v = 2.5 x 10^6 \text{ J.kg}^{-1}$  and  $\rho = 1.22 \text{ kg.m}^{-3}$  we obtain a value for the surface moisture flux into the PUFFIN domain.

# APPENDIX C

# PUFFIN-ABL Input File – Relevant Fields

GENERAL SECTION	
Description of	
Sample simulation	on of DYCOMS-II Lar to that used by Stevens et al, JAS 2004.
	unt time for the simulation
true <- us 7200.0 <- ts	ime (s)
true <- f:	inish exactly at the end of the specified time
Equations to so	Lve
	<pre>&lt;- solve mass conservation</pre>
true	<- solve mass conservation <- solve u
true	<- solve v
true true	<pre>&lt;- solve w &lt;- solve virtual potential temperature (h)</pre>
true	<pre>&lt;- solve moisture* (c)</pre>
true	<- solve rainwater* (q)
_	atio of water (kg/kg)
Non-uniform Car	tesian Grid
GRID SECTION	//////////////////////////////////////
==========	BASE GRID PAGE
	cells west boundary east boundary ( 1 cell for 2D)
	50 -2000.0 2000.0
-	No. $x-min$ $x-max$ (gaps will be filled)
	cells south boundary north boundary
	50 -2000.0 2000.0
-	No. y-min y-max (gaps will be filled)
• • • • • • • • • • • • • • • • • • • •	
Z max	cells bottom boundary top boundary
	40 0.0 1600.0
	No. z-min z-max (gaps will be filled)
	1 0.0 10.0 1 850.0 860.0

```
Boundaries of the domain
DOMAIN BOUNDARIES SECTION
Define simple domain boundary conditions. More complex boundary
conditions and internal blockages / inlets and outlets
can be defined using blockset.F90.
Boundary type
      east
            south north bottom top
west
......
                   1 11 20 <- uvw
1 11 20 <- h
1 11 20 <- c
1 20 20 <- q
      1
             1
 1
 1
       1
              1
             1
      1
 1
Key to available boundary types
1 = periodic
2 = inlet
3 = outlet
10 = impermeable - Dirichlet
11 = impermeable - set mean fluxes
12 = impermeable - interactive mean fluxes
20 = zero flux (freeslip / adiabatic)
LARGE EDDY SIMULATION SECTION
Classical Smagorinsky model
true <- use Smagorinsky model
        <- Smagorinsky coefficient
0.18
        <- subtract trace from Sij
false
true
        <- use Richardson number correction for buoyancy
Mason & Thomson (JFM, 1992) near surface model
<- use Mason-Thomson near surface model
Use LLAMA models (set controls in llama.in)
......
false <- use LLAMA
Surface conditions
<- friction velocity (ustar)
<- surface heat flux +ve into domain</pre>
                                      (if set fluxes) (m/s)
n (if set fluxes) (K.m/s)
0.209
0.0121
         <- surface moisture flux +ve into domain (if set fluxes) (kg/kg.m/s)
3.77e-5
15.0
          <- stability parameter = -z_{inv} / L (L is M-O length)
         <- surface roughness length
0.16
292.5
          <- temperature at surface
                                                       (K)
0.015
          <- mass mixing ratio for water at surface
                                                       (kg/kg)
otherwise initialise from inputs below
<- geostrophic wind flowing in easterly direction
<- geostrophic wind flowing in northerly direction
<- temperature just above surface
<- superadiabatic lapse rate of virtual temp in boundary layer</pre>
                                                            (m/s) *
-5.5
                                                            (m/s)
289.0
                                                            (K)
                                                             (K/km)
0.0
8.5
         <- virtual temp change across inversion
                                                             (K)
-10.0
          <- superadiabatic lapse rate of virtual temp above boundary layer (K/km)
840.0
         <- initial inversion height (z_inv)
100.0
          <- thickness of inversion
                                                             (m)
         <- mass mixing ratio for water in boundary layer
                                                             (kg/kg)
```

(kg/kg)

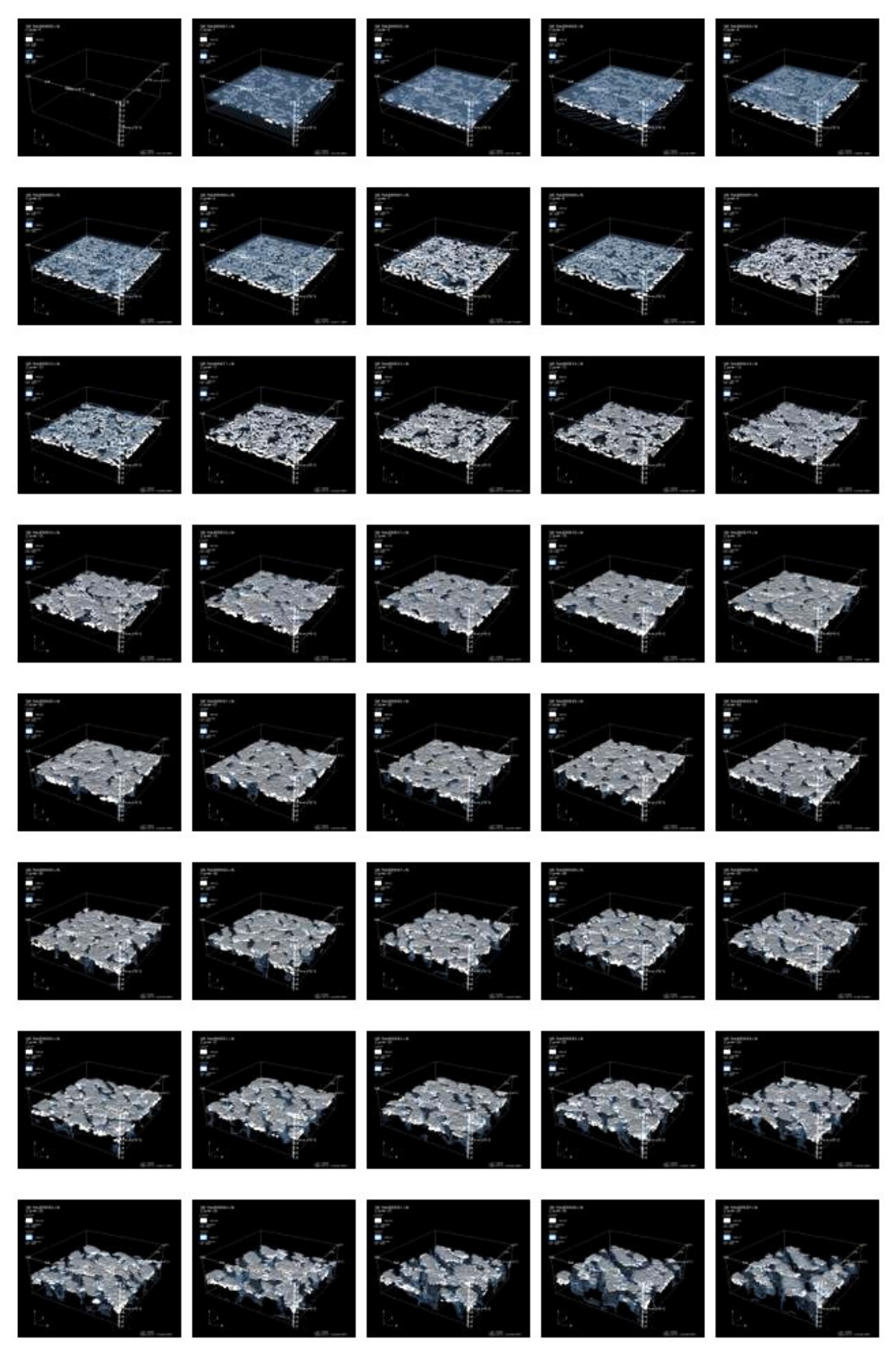
<- mass mixing ratio for water above boundary layer

0.009 0.0015

VISIT	OUI	PUI	rs s	ECT	ION								'//////// '/////////				
true 60.0				• • •		<-	prod	uce	file	s fo	r Vi		outputs?		•		
Real					_												
	-			-				-				-	vortici	-			
													1		0	1	
Post-	~~~ proc	ess	 sing	·~~~	~~~~	~~~	·~~~~	~~~~	~~~~	. ~ ~ ~ ~ . ~ ~ ~ ~	·~~~	. ~ ~ ~ ~ ~		. ~ ~ ~ ~ ~	~~~~~	~	
/////. DATA 1							/////	////	////	/////	////	/////	//////////	///////	////		
/////	////	////	////	///	////	////							//////////				
true				• • •									of run		•		
3600.0	)						to										
25.0						_				,			- 1 edd	4	over tir	ne)	
true							aver						present	-			
false								_	_				ound z a	axis			

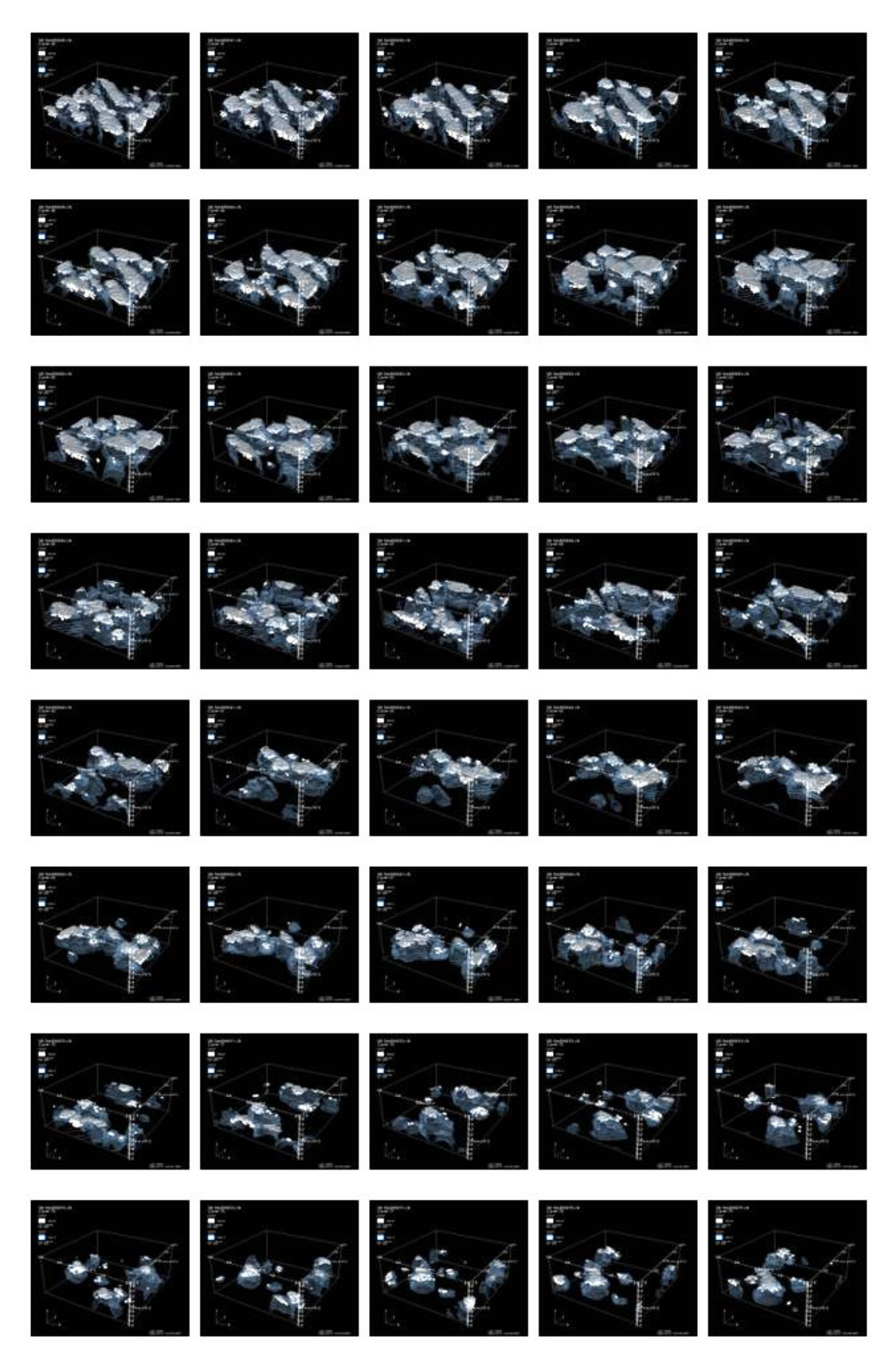
# APPENDIX D

# DII\_base - ISOMETRIC VIEW



0 to 2400 seconds

# DII\_base - ISOMETRIC VIEW

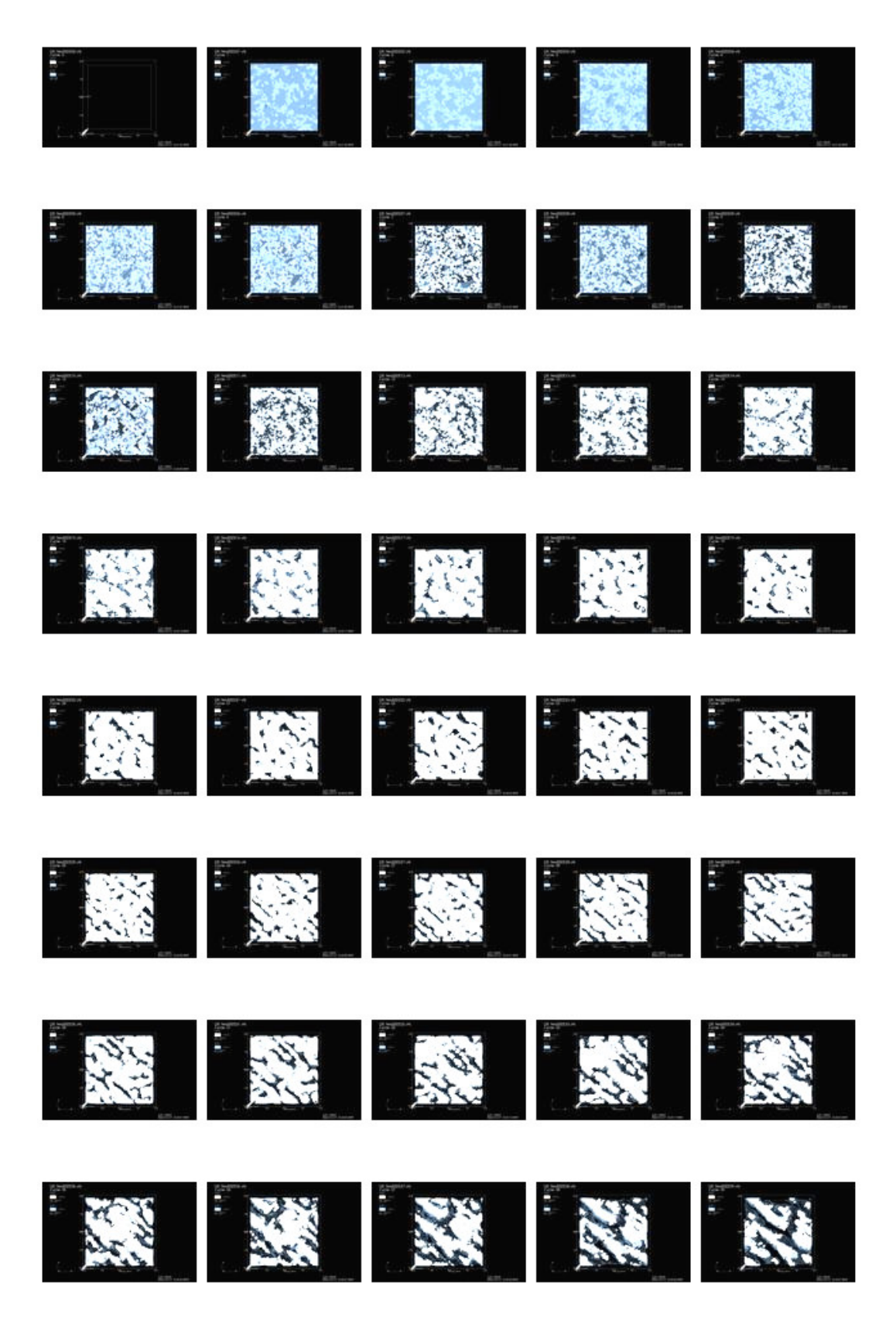


2400 to 4800 seconds

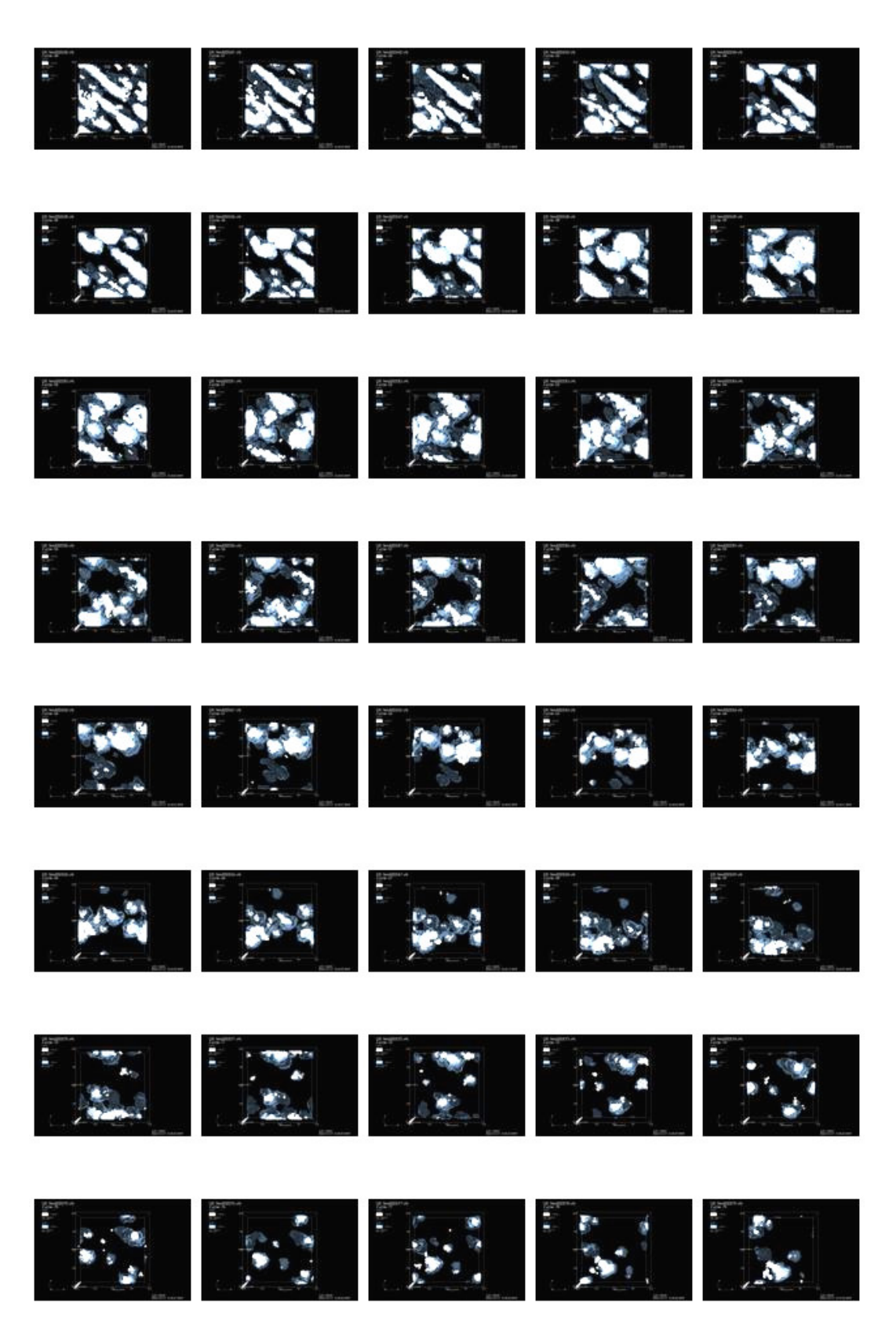
# DII\_base - ISOMETRIC VIEW



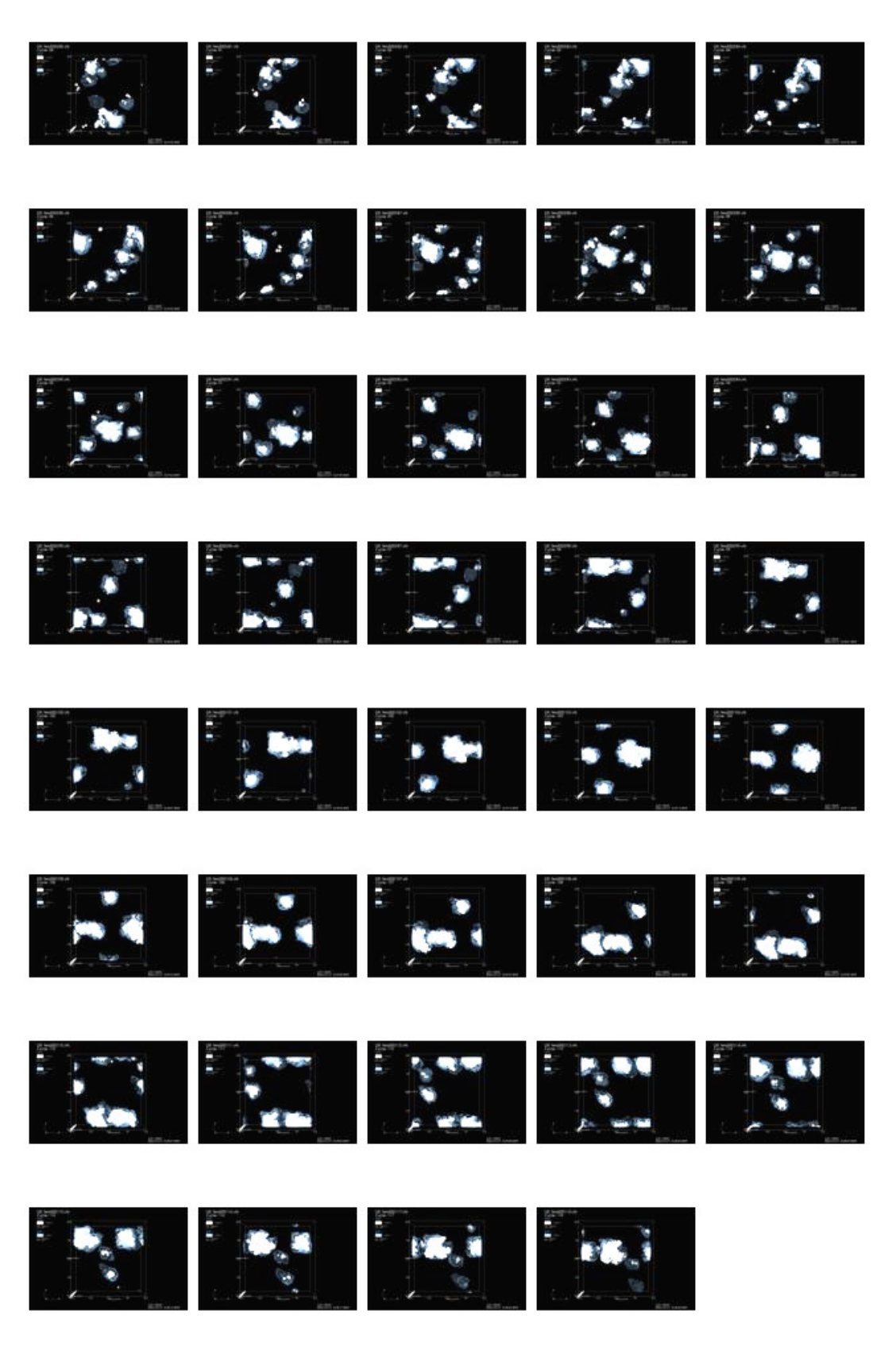
4200 to 7200 seconds



0 to 2400 seconds

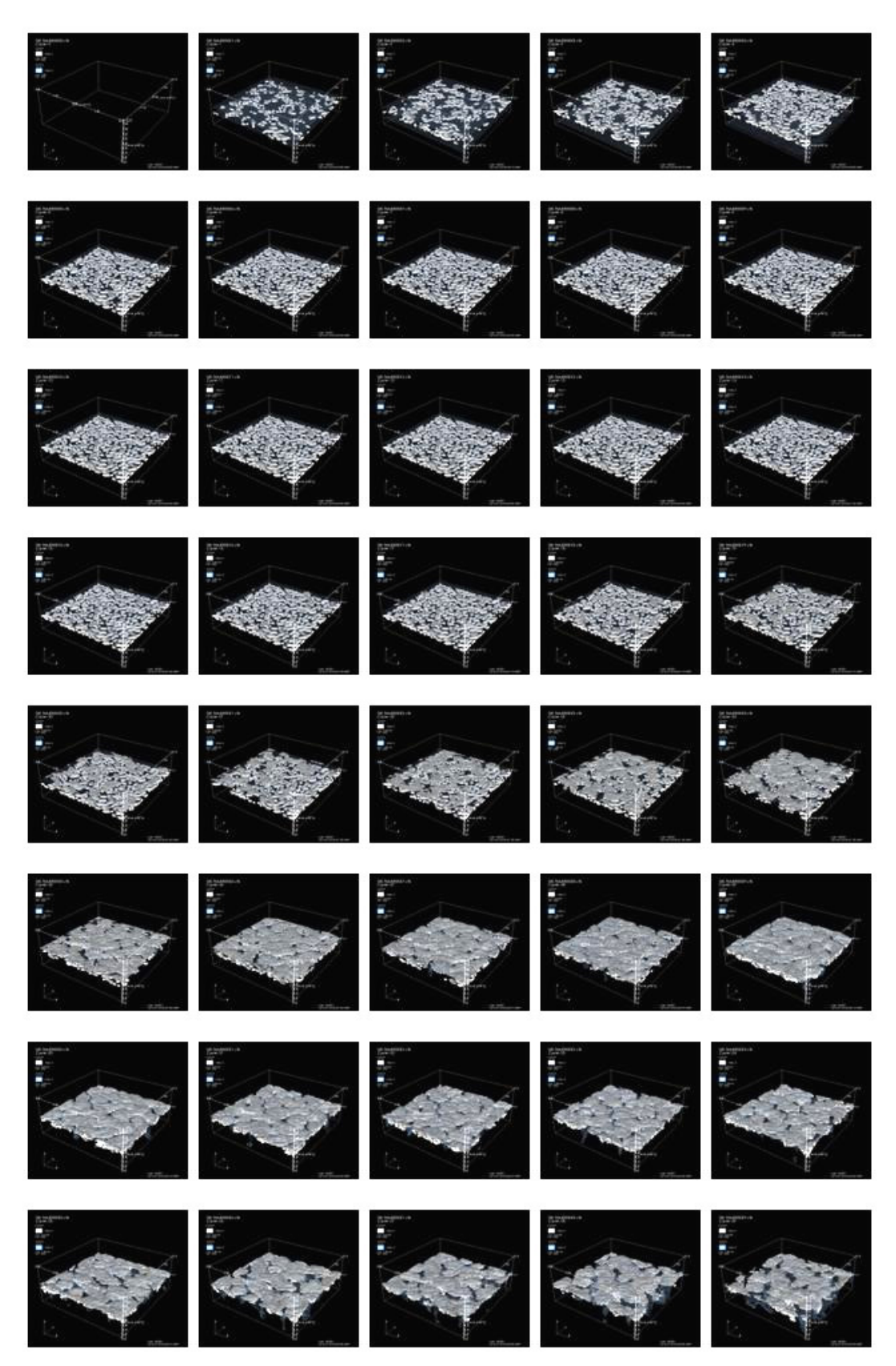


2400 to 4800 seconds



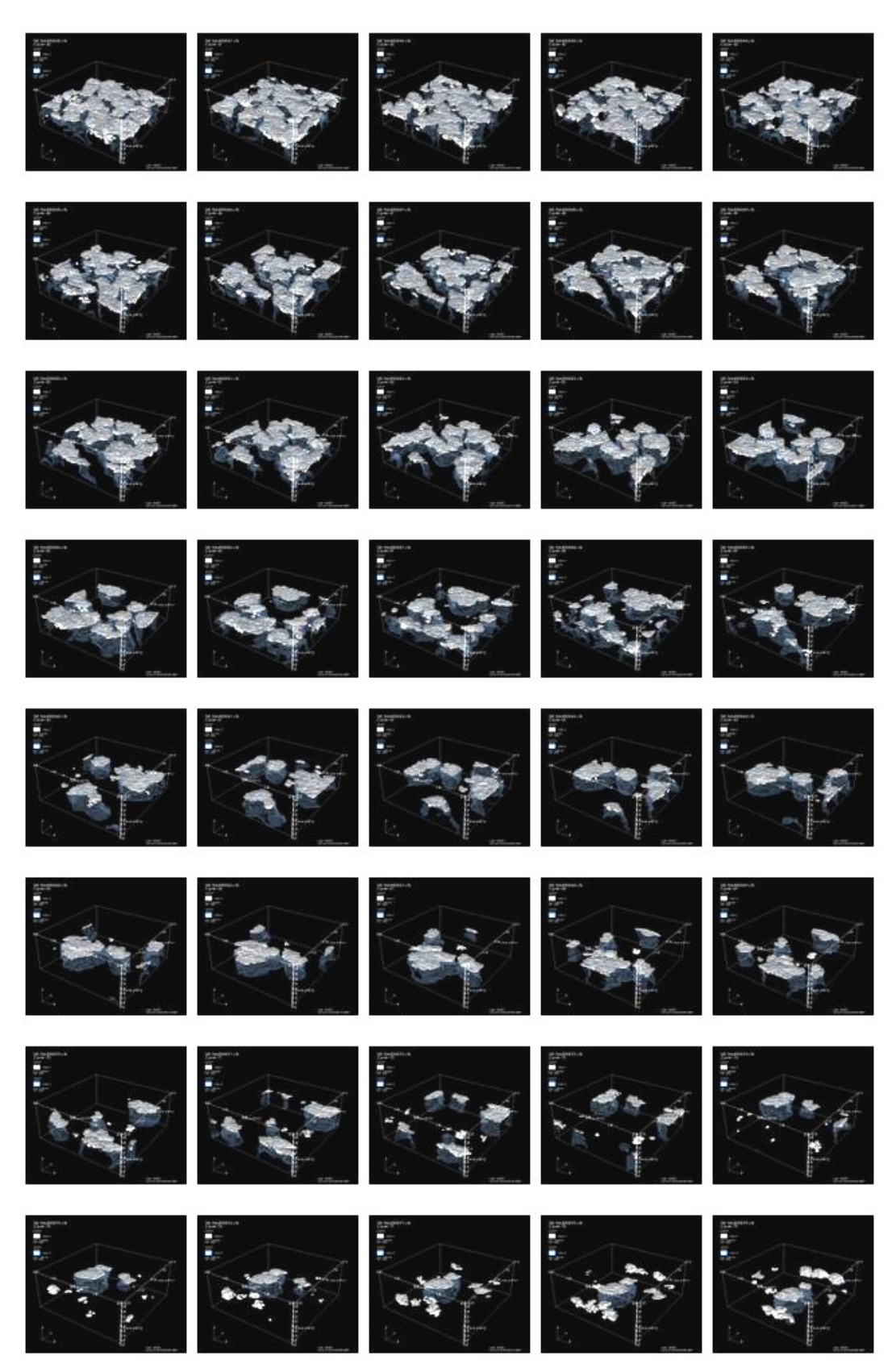
4800 to 7200 seconds

# Kessler1 - ISOMETRIC VIEW



0 to 2400 seconds

# Kessler1 - ISOMETRIC VIEW

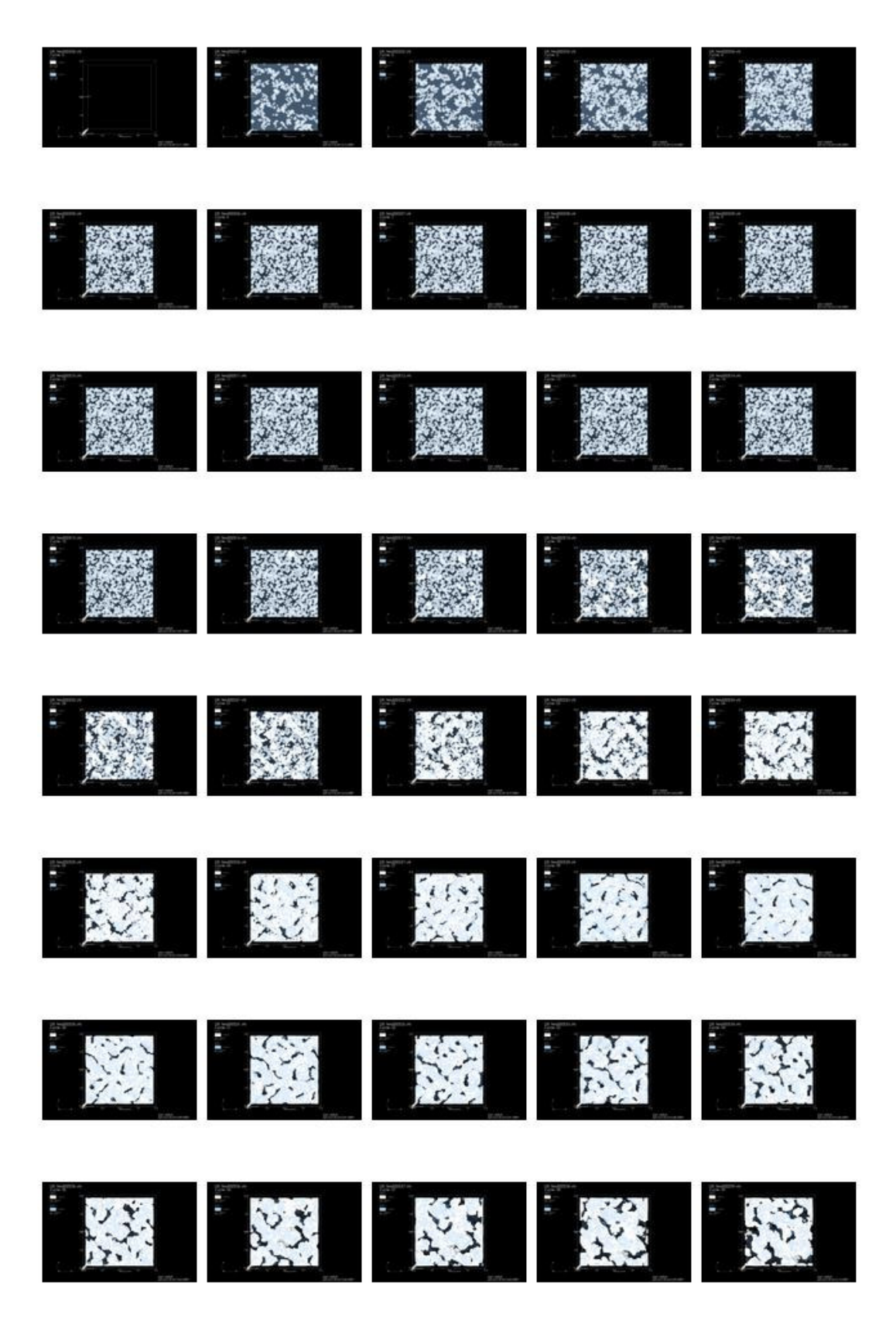


2400 to 4800 seconds

# Kessler1 - ISOMETRIC VIEW

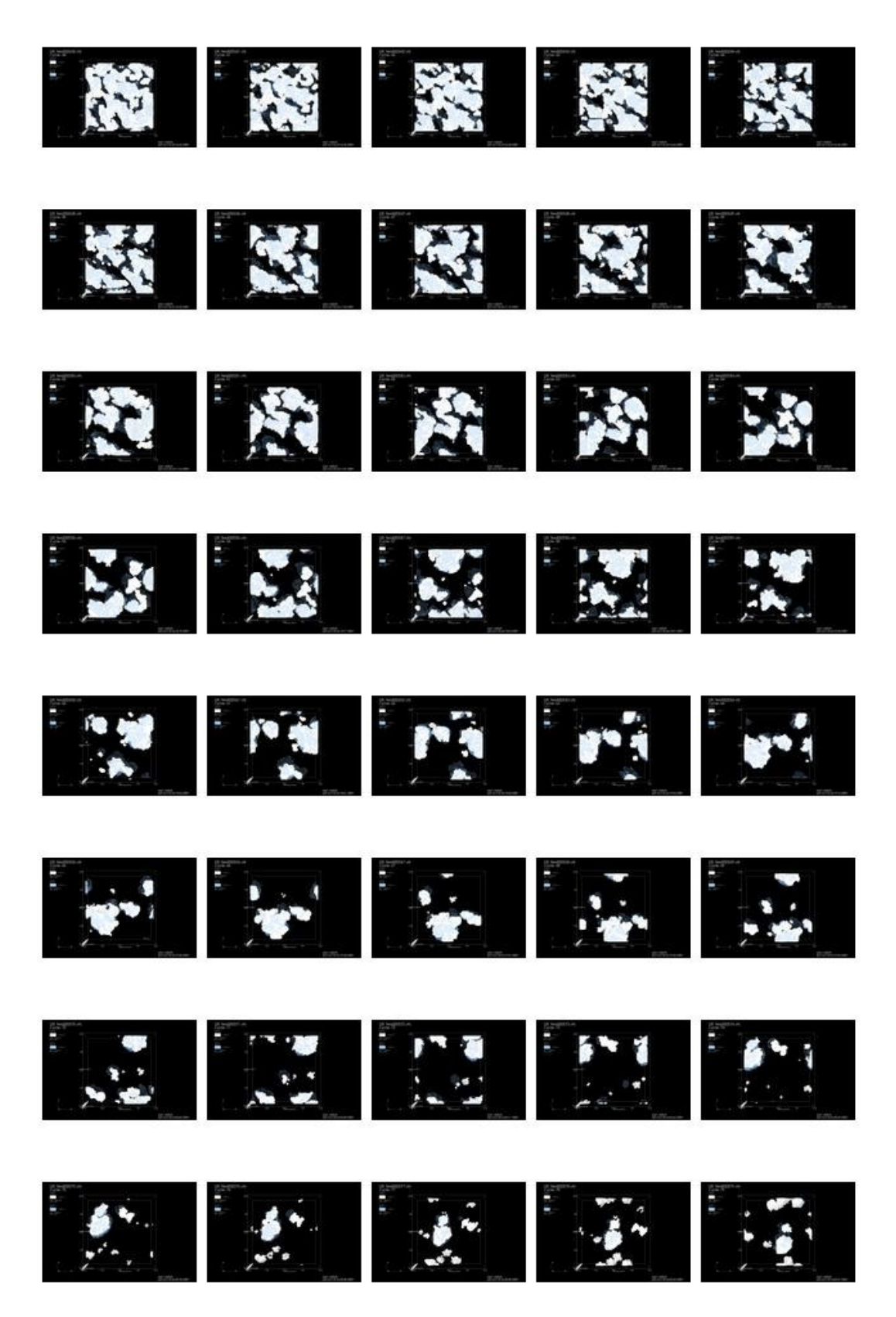


4800 to 7200 seconds



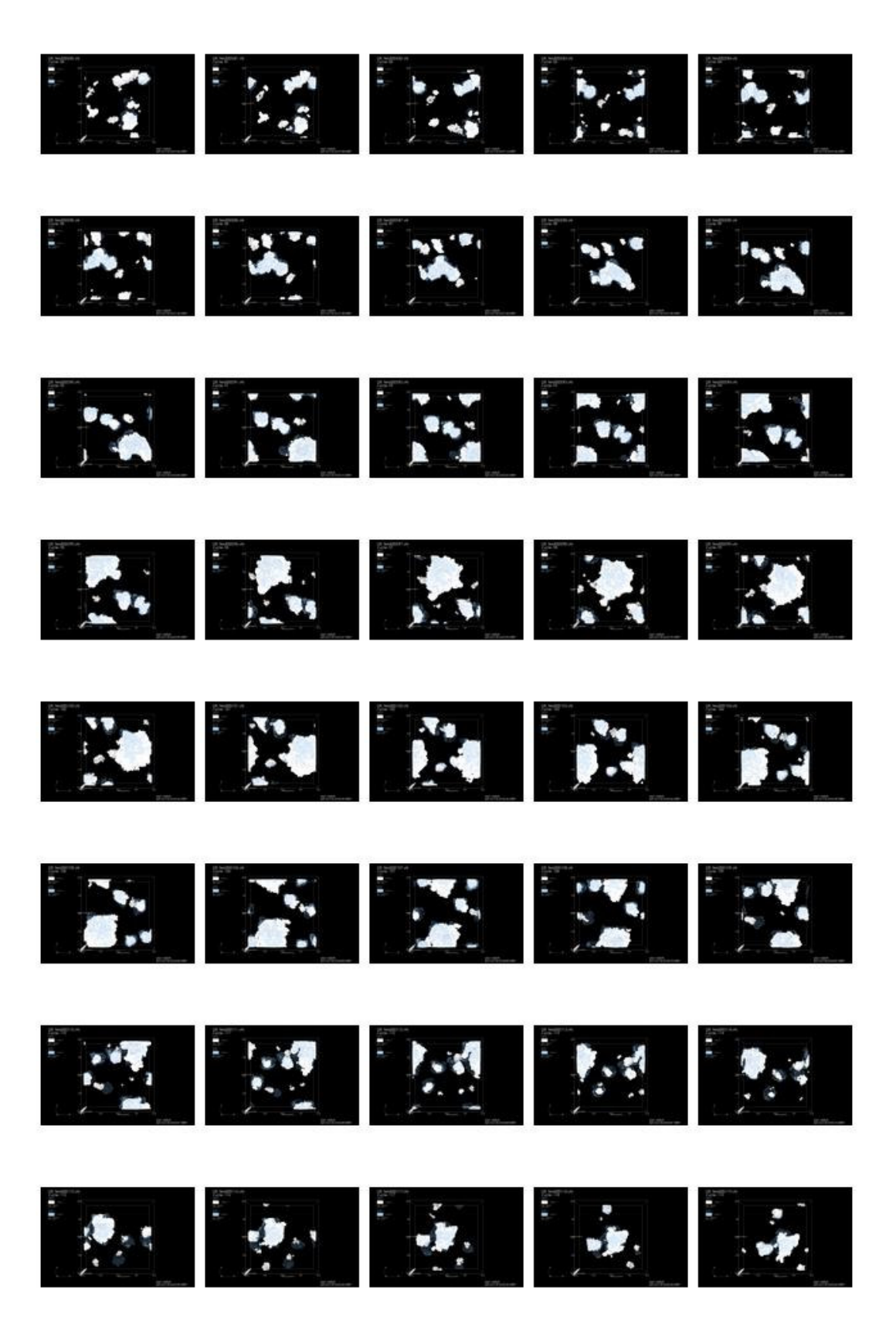
0 to 2400 seconds

## Kessler1 - TOP VIEW



2400 to 4800 seconds

# Kessler1 - TOP VIEW



4800 to 7200 second

# APPENDIX E

# DII\_base - Profile data

# Microphysics

Skewness pi	rofiles		Profiles					
Height	z <w></w>	$< w'^3 >$	qt_prof	ql_prof	θ_prof	P1_prof	P2_prof	EV_prof
5.0E+00	1.0E+01	7.4E-04	1.1E-02	0.0E+00	3.1E+02	0.0E+00	0.0E+00	4.3E-09
1.6E+01	2.2E+01	5.1E-03	1.0E-02	0.0E+00	3.1E+02	0.0E+00	0.0E+00	4.2E-09
2.9E+01	3.7E+01	1.1E-02	1.0E-02	0.0E+00	3.1E+02	0.0E+00	0.0E+00	4.2E-09
4.6E+01	5.5E+01	1.4E-02	1.0E-02	0.0E+00	3.1E+02	0.0E+00	0.0E+00	4.1E-09
6.6E+01	7.6E+01	1.0E-02	1.0E-02	0.0E+00	3.1E+02	0.0E+00	0.0E+00	4.3E-09
9.0E+01	1.0E+02	-5.4E-04	1.0E-02	0.0E+00	3.1E+02	0.0E+00	0.0E+00	4.2E-09
1.2E+02	1.3E+02	-1.6E-02	1.0E-02	0.0E+00	3.1E+02	0.0E+00	0.0E+00	4.0E-09
1.5E+02	1.7E+02	-3.3E-02	1.0E-02	0.0E+00	3.1E+02	0.0E+00	0.0E+00	3.6E-09
2.0E+02	2.2E+02	-4.7E-02	1.0E-02	0.0E+00	3.1E+02	0.0E+00	0.0E+00	3.2E-09
2.5E+02	2.8E+02	-5.3E-02	1.0E-02	0.0E+00	3.1E+02	0.0E+00	0.0E+00	2.6E-09
3.1E+02	3.5E+02	-4.8E-02	1.0E-02	0.0E+00	3.1E+02	0.0E+00	0.0E+00	2.0E-09
3.9E+02	4.3E+02	-3.0E-02	1.0E-02	0.0E+00	3.1E+02	0.0E+00	0.0E+00	1.1E-09
4.7E+02	5.1E+02	-2.2E-02	9.8E-03	5.5E-07	3.1E+02	2.5E-09	4.8E-10	4.1E-10
5.5E+02	5.8E+02	-3.2E-02	9.6E-03	2.4E-06	3.1E+02	2.6E-08	1.6E-09	2.7E-10
6.1E+02	6.4E+02	-4.1E-02	9.4E-03	2.7E-06	3.1E+02	3.4E-08	1.4E-09	2.0E-10
6.6E+02	6.9E+02	-4.4E-02	9.2E-03	2.8E-06	3.1E+02	3.7E-08	1.2E-09	1.5E-10
7.1E+02	7.3E+02	-4.4E-02	9.0E-03	2.7E-06	3.1E+02	3.5E-08	9.7E-10	1.2E-10
7.4E+02	7.6E+02	-3.8E-02	8.9E-03	3.8E-06	3.2E+02	4.4E-08	9.5E-10	9.0E-11
7.7E+02	7.8E+02	-3.0E-02	8.7E-03	4.3E-06	3.2E+02	4.6E-08	6.6E-10	6.8E-11
7.9E+02	8.1E+02	-2.2E-02	8.6E-03	5.1E-06	3.2E+02	5.0E-08	4.7E-10	4.5E-11
8.1E+02	8.2E+02	-1.5E-02	8.3E-03	4.9E-06	3.2E+02	5.2E-08	3.8E-10	3.0E-11
8.3E+02	8.4E+02	-9.5E-03	8.0E-03	2.4E-06	3.2E+02	2.0E-08	7.1E-11	2.7E-11
8.4E+02	8.5E+02	-5.9E-03	7.6E-03	1.2E-06	3.2E+02	1.1E-08	4.6E-11	3.4E-11
8.6E+02	8.6E+02	-3.6E-03	7.1E-03	7.6E-07	3.2E+02	1.0E-08	1.7E-11	2.2E-11
8.7E+02	8.7E+02	-1.7E-03	6.5E-03	2.3E-07	3.2E+02	6.3E-09	2.1E-12	1.2E-11
8.8E+02	8.9E+02	-3.8E-04	5.7E-03	0.0E+00	3.2E+02	0.0E+00	0.0E+00	9.3E-13
9.0E+02	9.0E+02	4.6E-04	4.9E-03	0.0E+00	3.2E+02	0.0E+00	0.0E+00	6.9E-14
9.1E+02	9.3E+02	9.8E-04	4.1E-03	0.0E+00	3.2E+02	0.0E+00	0.0E+00	1.5E-15
9.4E+02	9.5E+02	8.8E-04	3.4E-03	0.0E+00	3.2E+02	0.0E+00	0.0E+00	2.0E-17
9.7E+02	9.8E+02	2.0E-03	2.8E-03	0.0E+00	3.2E+02	0.0E+00	0.0E+00	2.4E-18
1.0E+03	1.0E+03	2.8E-03	2.4E-03	0.0E+00	3.2E+02	0.0E+00	0.0E+00	6.0E-19
1.0E+03	1.1E+03	-2.2E-03	2.1E-03	0.0E+00	3.2E+02	0.0E+00	0.0E+00	5.6E-19
1.1E+03	1.1E+03	-1.1E-03	1.8E-03	0.0E+00	3.2E+02	0.0E+00	0.0E+00	5.7E-19
1.1E+03	1.2E+03	-1.5E-03	1.7E-03	0.0E+00	3.3E+02	0.0E+00	0.0E+00	5.8E-19
1.2E+03	1.3E+03	3.2E-05	1.6E-03	0.0E+00	3.3E+02	0.0E+00	0.0E+00	5.8E-19
1.3E+03	1.4E+03	1.8E-05	1.6E-03	0.0E+00	3.3E+02	0.0E+00	0.0E+00	5.9E-19
1.4E+03	1.5E+03	9.6E-04	1.6E-03	0.0E+00	3.3E+02	0.0E+00	0.0E+00	6.0E-19

Total water mixing ratio profile Cloud liquid water mixing ratio profile Liquid water potential temperature profile Autoconversion profile

qt\_prof: ql\_prof: θ\_prof: P1\_prof: P2\_prof: EV\_prof: Accretion profile Evaporation profile

# DII\_fine - PROFILE DATA

Skewness	profiles		Microphy	ysics Profile	es			
Height	z <w></w>	$< w'^3 >$	qt_prof	ql_prof	θ_prof	P1_prof	P2_prof	EV_prof
2.5E+00	5.0E+00	1.5E-04	1.2E-02	5.2E-06	3.0E+02	2.5E-08	4.8E-10	7.9E-10
7.7E+00	1.0E+01	1.0E-03	1.1E-02	5.2E-07	3.0E+02	1.2E-09	6.8E-11	1.3E-09
1.3E+01	1.6E+01	2.3E-03	1.1E-02	8.4E-08	3.0E+02	1.3E-10	6.2E-12	1.7E-09
2.0E+01	2.3E+01	3.4E-03	1.1E-02	7.3E-08	3.0E+02	1.1E-10	9.2E-12	1.8E-09
2.6E+01	3.0E+01	3.3E-03	1.1E-02	2.9E-08	3.0E+02	2.3E-11	3.9E-12	1.9E-09
3.4E+01	3.8E+01	1.9E-03	1.1E-02	4.9E-08	3.0E+02	1.4E-10	1.5E-12	1.9E-09
4.2E+01	4.6E+01	-8.3E-04	1.1E-02	1.9E-08	3.0E+02	3.9E-11	5.3E-13	1.9E-09
5.1E+01	5.5E+01	-4.7E-03	1.1E-02	5.1E-08	3.0E+02	1.0E-10	4.2E-12	1.8E-09
6.0E+01	6.5E+01	-9.3E-03	1.1E-02	5.6E-08	3.0E+02	1.2E-10	5.8E-12	1.7E-09
7.1E+01	7.6E+01	-1.4E-02	1.1E-02	2.8E-07	3.0E+02	1.0E-09	2.7E-11	1.6E-09
8.2E+01	8.8E+01	-2.0E-02	1.1E-02	4.7E-07	3.0E+02	1.5E-09	5.2E-11	1.4E-09
9.5E+01	1.0E+02	-2.6E-02	1.1E-02	1.1E-06	3.0E+02	5.0E-09	1.9E-10	1.3E-09
1.1E+02	1.2E+02	-3.2E-02	1.1E-02	1.8E-06	3.0E+02	7.8E-09	3.2E-10	1.2E-09
1.2E+02	1.3E+02	-3.9E-02	1.1E-02	3.3E-06	3.0E+02	2.1E-08	7.1E-10	1.1E-09
1.4E+02	1.5E+02	-4.6E-02	1.1E-02	4.1E-06	3.0E+02	3.2E-08	1.1E-09	1.0E-09
1.6E+02	1.7E+02	-5.3E-02	1.0E-02	4.7E-06	3.0E+02	4.0E-08	1.2E-09	9.5E-10
1.8E+02	1.9E+02	-6.0E-02	1.0E-02	4.0E-06	3.0E+02	3.7E-08	1.0E-09	9.0E-10
2.0E+02	2.1E+02	-6.8E-02	1.0E-02	4.2E-06	3.0E+02	4.4E-08	1.5E-09	8.7E-10
2.2E+02	2.3E+02	-7.6E-02	1.0E-02	3.8E-06	3.0E+02	4.1E-08	1.4E-09	8.9E-10
2.4E+02	2.6E+02	-8.3E-02	1.0E-02	2.9E-06	3.0E+02	3.4E-08	1.4E-09	9.4E-10
2.7E+02	2.9E+02	-9.2E-02	1.0E-02	1.9E-06	3.0E+02	2.0E-08	1.1E-09	9.0E-10
3.0E+02	3.2E+02	-1.0E-01	9.9E-03	2.3E-06	3.0E+02	2.6E-08	1.6E-09	9.0E-10
3.3E+02	3.5E+02	-1.1E-01	9.8E-03	2.0E-06	3.0E+02	2.4E-08	1.6E-09	8.7E-10
3.7E+02	3.9E+02	-1.2E-01	9.7E-03	1.5E-06	3.0E+02	1.7E-08	1.3E-09	8.1E-10
4.1E+02	4.3E+02	-1.3E-01	9.6E-03	1.6E-06	3.0E+02	2.0E-08	1.4E-09	7.8E-10
4.5E+02	4.7E+02	-1.4E-01	9.5E-03	2.0E-06	3.0E+02	2.8E-08	1.7E-09	6.9E-10
4.9E+02	5.0E+02	-1.4E-01	9.4E-03	2.0E-06	3.1E+02	2.7E-08	1.5E-09	6.5E-10
5.2E+02	5.4E+02	-1.4E-01	9.3E-03	2.5E-06	3.1E+02	3.3E-08	1.7E-09	5.6E-10
5.5E+02	5.7E+02	-1.4E-01	9.2E-03	2.8E-06	3.1E+02	4.0E-08	1.6E-09	5.0E-10
5.8E+02	6.0E+02	-1.4E-01	9.2E-03	2.6E-06	3.1E+02	4.0E-08	1.5E-09	4.9E-10
6.1E+02	6.2E+02	-1.5E-01	9.1E-03	2.9E-06	3.1E+02	4.6E-08	1.4E-09	4.2E-10
6.4E+02	6.5E+02	-1.4E-01	9.0E-03	2.8E-06	3.1E+02	4.5E-08	1.4E-09	3.5E-10
6.6E+02	6.7E+02	-1.4E-01	8.9E-03	2.8E-06	3.1E+02	4.3E-08	1.3E-09	3.0E-10
6.8E+02	6.9E+02	-1.4E-01	8.9E-03	3.1E-06	3.1E+02	4.7E-08	1.3E-09	2.6E-10
7.0E+02	7.1E+02	-1.4E-01	8.8E-03	3.3E-06	3.1E+02	5.0E-08	1.2E-09	2.4E-10
7.2E+02	7.2E+02	-1.4E-01	8.7E-03	2.9E-06	3.1E+02	4.0E-08	9.9E-10	2.3E-10
7.3E+02	7.4E+02	-1.3E-01	8.6E-03	2.7E-06	3.1E+02	3.8E-08	8.5E-10	2.4E-10
7.5E+02	7.5E+02	-1.3E-01	8.6E-03	2.2E-06	3.1E+02	3.0E-08	8.0E-10	2.4E-10
7.6E+02	7.7E+02	-1.3E-01	8.5E-03	2.1E-06	3.1E+02	2.7E-08	8.1E-10	2.3E-10
7.7E+02	7.8E+02	-1.2E-01	8.4E-03	2.0E-06	3.1E+02	2.4E-08	6.6E-10	2.3E-10
7.8E+02	7.9E+02	-1.2E-01	8.4E-03	2.3E-06	3.1E+02	2.9E-08	7.7E-10	2.1E-10
7.9E+02	8.0E+02	-1.1E-01	8.3E-03	2.4E-06	3.1E+02	3.1E-08	7.4E-10	2.0E-10
8.0E+02	8.1E+02	-1.0E-01	8.3E-03	2.4E-06	3.1E+02	2.8E-08	6.7E-10	1.8E-10
8.1E+02	8.2E+02	-9.7E-02	8.2E-03	2.6E-06	3.1E+02	3.1E-08	7.3E-10	1.6E-10
8.2E+02	8.3E+02	-9.1E-02	8.2E-03	2.6E-06	3.1E+02	3.0E-08	6.7E-10	1.5E-10
8.3E+02	8.3E+02	-8.5E-02	8.1E-03	2.9E-06	3.1E+02	3.1E-08	5.8E-10	1.4E-10
8.4E+02	8.4E+02	-7.8E-02	8.0E-03	3.3E-06	3.1E+02	3.6E-08	5.7E-10	1.3E-10
8.4E+02	8.4E+02	-7.3E-02	8.0E-03	3.3E-06	3.1E+02	3.7E-08	5.9E-10	1.2E-10
8.5E+02	8.5E+02	-6.7E-02	7.9E-03	3.6E-06	3.1E+02	3.7E-08	5.4E-10	1.1E-10

8.5E+02	8.6E+02	-6.2E-02	7.8E-03	3.7E-06	3.1E+02	3.5E-08	4.8E-10	1.0E-10
8.6E+02	8.6E+02	-5.7E-02	7.7E-03	4.5E-06	3.1E+02	4.2E-08	4.7E-10	8.8E-11
8.6E+02	8.7E+02	-5.1E-02	7.5E-03	4.2E-06	3.1E+02	3.7E-08	3.9E-10	8.2E-11
8.7E+02	8.7E+02	-4.4E-02	7.4E-03	4.9E-06	3.1E+02	4.6E-08	4.4E-10	6.7E-11
8.8E+02	8.8E+02	-3.8E-02	7.1E-03	4.2E-06	3.1E+02	3.9E-08	3.2E-10	6.4E-11
8.8E+02	8.9E+02	-3.1E-02	6.8E-03	3.8E-06	3.1E+02	3.9E-08	2.9E-10	5.4E-11
8.9E+02	9.0E+02	-2.5E-02	6.4E-03	2.3E-06	3.1E+02	2.7E-08	2.1E-10	5.0E-11
9.0E+02	9.1E+02	-1.8E-02	5.9E-03	2.0E-06	3.1E+02	2.6E-08	1.7E-10	4.4E-11
9.1E+02	9.2E+02	-1.3E-02	5.4E-03	8.8E-07	3.1E+02	1.2E-08	5.9E-11	3.9E-11
9.2E+02	9.3E+02	-8.1E-03	4.7E-03	5.8E-07	3.1E+02	9.5E-09	5.3E-11	3.3E-11
9.3E+02	9.4E+02	-4.4E-03	4.0E-03	7.1E-07	3.1E+02	1.1E-08	4.0E-11	9.8E-12
9.4E+02	9.5E+02	-1.6E-03	3.3E-03	0.0E+00	3.1E+02	0.0E+00	0.0E+00	5.4E-12
9.6E+02	9.6E+02	-2.3E-05	2.7E-03	0.0E+00	3.1E+02	0.0E+00	0.0E+00	1.3E-13
9.7E+02	9.8E+02	7.2E-04	2.3E-03	0.0E+00	3.1E+02	0.0E+00	0.0E+00	1.1E-15
9.9E+02	1.0E+03	9.8E-04	2.0E-03	0.0E+00	3.1E+02	0.0E+00	0.0E+00	6.9E-19
1.0E+03	1.0E+03	7.1E-04	1.8E-03	0.0E+00	3.1E+02	0.0E+00	0.0E+00	5.5E-19
1.0E+03	1.0E+03	6.5E-04	1.7E-03	0.0E+00	3.1E+02	0.0E+00	0.0E+00	5.5E-19
1.0E+03	1.1E+03	3.4E-04	1.6E-03	0.0E+00	3.1E+02	0.0E+00	0.0E+00	5.5E-19
1.1E+03	1.1E+03	6.0E-04	1.6E-03	0.0E+00	3.1E+02	0.0E+00	0.0E+00	5.5E-19
1.1E+03	1.1E+03	3.9E-04	1.6E-03	0.0E+00	3.1E+02	0.0E+00	0.0E+00	5.6E-19
1.1E+03	1.1E+03	1.4E-04	1.6E-03	0.0E+00	3.2E+02	0.0E+00	0.0E+00	5.6E-19
1.2E+03	1.2E+03	4.9E-05	1.6E-03	0.0E+00	3.2E+02	0.0E+00	0.0E+00	5.6E-19
1.2E+03	1.2E+03	7.6E-06	1.6E-03	0.0E+00	3.2E+02	0.0E+00	0.0E+00	5.6E-19
1.2E+03	1.2E+03	7.6E-06	1.6E-03	0.0E+00	3.2E+02	0.0E+00	0.0E+00	5.6E-19
1.3E+03	1.3E+03	9.7E-06	1.6E-03	0.0E+00	3.2E+02	0.0E+00	0.0E+00	5.6E-19
1.3E+03	1.3E+03	8.0E-06	1.6E-03	0.0E+00	3.2E+02	0.0E+00	0.0E+00	5.6E-19
1.3E+03	1.4E+03	2.3E-05	1.6E-03	0.0E+00	3.2E+02	0.0E+00	0.0E+00	5.6E-19
1.4E+03	1.4E+03	7.2E-05	1.6E-03	0.0E+00	3.2E+02	0.0E+00	0.0E+00	5.6E-19
1.4E+03	1.5E+03	9.2E-05	1.6E-03	0.0E+00	3.2E+02	0.0E+00	0.0E+00	5.6E-19
1.5E+03	1.5E+03	3.4E-05	1.6E-03	0.0E+00	3.2E+02	0.0E+00	0.0E+00	5.6E-19

# NoRad - Profile data

Skewness	profiles		Microphysi	cs Profiles				
Height	z <w></w>	$< w'^3 >$	qt_prof	ql_prof	θ_prof	P1_prof	P2_prof	EV_prof
5.0E+00	1.0E+01	6.1E-04	1.1E-02	0.0E+00	3.1E+02	0.0E+00	0.0E+00	5.7E-09
1.6E+01	2.2E+01	4.1E-03	1.0E-02	0.0E+00	3.1E+02	0.0E+00	0.0E+00	5.7E-09
2.9E+01	3.7E+01	8.5E-03	1.0E-02	0.0E+00	3.1E+02	0.0E+00	0.0E+00	4.9E-09
4.6E+01	5.5E+01	1.0E-02	1.0E-02	0.0E+00	3.1E+02	0.0E+00	0.0E+00	5.0E-09
6.6E+01	7.6E+01	6.8E-03	1.0E-02	0.0E+00	3.1E+02	0.0E+00	0.0E+00	5.2E-09
9.0E+01	1.0E+02	-2.0E-03	1.0E-02	0.0E+00	3.1E+02	0.0E+00	0.0E+00	5.3E-09
1.2E+02	1.3E+02	-1.5E-02	1.0E-02	0.0E+00	3.1E+02	0.0E+00	0.0E+00	5.2E-09
1.5E+02	1.7E+02	-3.0E-02	1.0E-02	0.0E+00	3.1E+02	0.0E+00	0.0E+00	4.9E-09
2.0E+02	2.2E+02	-4.3E-02	1.0E-02	0.0E+00	3.1E+02	0.0E+00	0.0E+00	4.6E-09
2.5E+02	2.8E+02	-4.5E-02	1.0E-02	0.0E+00	3.1E+02	0.0E+00	0.0E+00	4.1E-09
3.1E+02	3.5E+02	-3.7E-02	1.0E-02	0.0E+00	3.1E+02	0.0E+00	0.0E+00	3.4E-09
3.9E+02	4.3E+02	-2.1E-02	1.0E-02	0.0E+00	3.1E+02	0.0E+00	0.0E+00	2.3E-09
4.7E+02	5.1E+02	-1.0E-02	1.0E-02	0.0E+00	3.1E+02	0.0E+00	0.0E+00	9.7E-10
5.5E+02	5.8E+02	-8.3E-03	9.9E-03	3.6E-06	3.1E+02	2.6E-08	1.4E-09	2.7E-10
6.1E+02	6.4E+02	-1.1E-02	9.7E-03	7.0E-06	3.1E+02	7.5E-08	2.3E-09	2.0E-10
6.6E+02	6.9E+02	-1.2E-02	9.6E-03	6.8E-06	3.1E+02	7.3E-08	1.6E-09	1.5E-10
7.1E+02	7.3E+02	-9.5E-03	9.4E-03	7.2E-06	3.2E+02	7.7E-08	1.4E-09	9.9E-11
7.4E+02	7.6E+02	-7.8E-03	9.3E-03	6.2E-06	3.2E+02	6.1E-08	7.7E-10	7.1E-11
7.7E+02	7.8E+02	-5.4E-03	9.1E-03	5.0E-06	3.2E+02	4.9E-08	5.4E-10	5.8E-11
7.9E+02	8.1E+02	-3.3E-03	8.8E-03	3.6E-06	3.2E+02	3.4E-08	2.1E-10	4.5E-11
8.1E+02	8.2E+02	-1.8E-03	8.4E-03	2.0E-06	3.2E+02	2.3E-08	1.2E-10	4.7E-11
8.3E+02	8.4E+02	-9.1E-04	7.9E-03	1.5E-06	3.2E+02	1.7E-08	4.7E-11	3.8E-11
8.4E+02	8.5E+02	-3.7E-04	7.3E-03	9.7E-07	3.2E+02	9.6E-09	1.5E-11	3.5E-11
8.6E+02	8.6E+02	-3.1E-05	6.6E-03	5.0E-08	3.2E+02	1.5E-10	7.6E-31	2.5E-11
8.7E+02	8.7E+02	2.7E-04	5.8E-03	0.0E+00	3.2E+02	0.0E+00	0.0E+00	3.8E-13
8.8E+02	8.9E+02	4.6E-04	5.0E-03	0.0E+00	3.2E+02	0.0E+00	0.0E+00	7.7E-15
9.0E+02	9.0E+02	1.0E-03	4.3E-03	0.0E+00	3.2E+02	0.0E+00	0.0E+00	3.0E-16
9.1E+02	9.3E+02	8.2E-04	3.6E-03	0.0E+00	3.2E+02	0.0E+00	0.0E+00	3.4E-17
9.4E+02	9.5E+02	1.8E-03	3.1E-03	0.0E+00	3.2E+02	0.0E+00	0.0E+00	4.2E-18
9.7E+02	9.8E+02	3.7E-03	2.6E-03	0.0E+00	3.2E+02	0.0E+00	0.0E+00	6.4E-19
1.0E+03	1.0E+03	2.4E-03	2.3E-03	0.0E+00	3.2E+02	0.0E+00	0.0E+00	5.6E-19
1.0E+03	1.1E+03	-4.6E-03	2.0E-03	0.0E+00	3.3E+02	0.0E+00	0.0E+00	5.8E-19
1.1E+03	1.1E+03	-5.3E-03	1.9E-03	0.0E+00	3.3E+02	0.0E+00	0.0E+00	5.9E-19
1.1E+03	1.2E+03	-3.1E-03	1.7E-03	0.0E+00	3.3E+02	0.0E+00	0.0E+00	5.9E-19
1.2E+03	1.3E+03	3.4E-03	1.7E-03	0.0E+00	3.3E+02	0.0E+00	0.0E+00	6.0E-19
1.3E+03	1.4E+03	-1.9E-04	1.6E-03	0.0E+00	3.3E+02	0.0E+00	0.0E+00	6.0E-19
1.4E+03	1.5E+03	2.4E-02	1.6E-03	0.0E+00	3.3E+02	0.0E+00	0.0E+00	6.0E-19

# Kessler1 - Profile data

Skewness	profiles		Microph	ysics Profil	es			
Height	z <w></w>	$< w'^3 >$	qt_prof	ql_prof	θ_prof	P1_prof	P2_prof	EV_prof
5.0E+00	1.0E+01	8.3E-04	1.0E-02	0.0E+00	3.1E+02	0.0E+00	0.0E+00	1.6E-09
1.6E+01	2.2E+01	5.5E-03	1.0E-02	0.0E+00	3.1E+02	0.0E+00	0.0E+00	1.7E-09
2.9E+01	3.7E+01	1.1E-02	1.0E-02	0.0E+00	3.1E+02	0.0E+00	0.0E+00	1.7E-09
4.6E+01	5.5E+01	1.4E-02	1.0E-02	0.0E+00	3.1E+02	0.0E+00	0.0E+00	1.7E-09
6.6E+01	7.6E+01	1.1E-02	1.0E-02	0.0E+00	3.1E+02	0.0E+00	0.0E+00	1.6E-09
9.0E+01	1.0E+02	-1.3E-04	1.0E-02	0.0E+00	3.1E+02	0.0E+00	0.0E+00	1.6E-09
1.2E+02	1.3E+02	-1.6E-02	1.0E-02	0.0E+00	3.1E+02	0.0E+00	0.0E+00	1.5E-09
1.5E+02	1.7E+02	-3.3E-02	9.9E-03	0.0E+00	3.1E+02	0.0E+00	0.0E+00	1.4E-09
2.0E+02	2.2E+02	-5.0E-02	9.9E-03	0.0E+00	3.1E+02	0.0E+00	0.0E+00	1.3E-09
2.5E+02	2.8E+02	-6.1E-02	9.9E-03	0.0E+00	3.1E+02	0.0E+00	0.0E+00	1.1E-09
3.1E+02	3.5E+02	-6.2E-02	9.8E-03	0.0E+00	3.1E+02	0.0E+00	0.0E+00	9.4E-10
3.9E+02	4.3E+02	-5.2E-02	9.8E-03	0.0E+00	3.1E+02	0.0E+00	0.0E+00	7.0E-10
4.7E+02	5.1E+02	-4.4E-02	9.6E-03	0.0E+00	3.1E+02	0.0E+00	0.0E+00	4.3E-10
5.5E+02	5.8E+02	-5.4E-02	9.4E-03	2.1E-06	3.1E+02	0.0E+00	1.4E-10	2.6E-10
6.1E+02	6.4E+02	-7.8E-02	9.2E-03	7.0E-06	3.1E+02	3.7E-10	3.9E-10	2.5E-10
6.6E+02	6.9E+02	-9.8E-02	9.0E-03	9.9E-06	3.1E+02	2.7E-09	9.7E-10	2.0E-10
7.1E+02	7.3E+02	-1.2E-01	8.9E-03	1.4E-05	3.1E+02	4.2E-09	1.5E-09	1.3E-10
7.4E+02	7.6E+02	-1.2E-01	8.8E-03	1.9E-05	3.1E+02	6.7E-09	1.8E-09	1.3E-10
7.7E+02	7.8E+02	-1.2E-01	8.7E-03	2.4E-05	3.1E+02	8.9E-09	2.4E-09	1.3E-10
7.9E+02	8.1E+02	-1.1E-01	8.5E-03	2.3E-05	3.2E+02	9.9E-09	1.9E-09	1.7E-10
8.1E+02	8.2E+02	-1.0E-01	8.4E-03	2.5E-05	3.2E+02	1.2E-08	2.1E-09	1.6E-10
8.3E+02	8.4E+02	-8.7E-02	8.3E-03	2.6E-05	3.2E+02	1.4E-08	2.1E-09	1.5E-10
8.4E+02	8.5E+02	-7.6E-02	8.1E-03	2.8E-05	3.2E+02	1.7E-08	2.0E-09	1.5E-10
8.6E+02	8.6E+02	-6.5E-02	8.0E-03	3.1E-05	3.2E+02	1.9E-08	2.3E-09	1.1E-10
8.7E+02	8.7E+02	-5.3E-02	7.8E-03	2.3E-05	3.2E+02	1.5E-08	1.6E-09	1.3E-10
8.8E+02	8.9E+02	-3.9E-02	7.6E-03	2.0E-05	3.2E+02	1.3E-08	1.2E-09	1.2E-10
9.0E+02	9.0E+02	-2.5E-02	7.2E-03	2.1E-05	3.2E+02	1.4E-08	1.3E-09	7.2E-11
9.1E+02	9.3E+02	-1.2E-02	6.6E-03	8.5E-06	3.2E+02	5.5E-09	5.6E-10	6.0E-11
9.4E+02	9.5E+02	-2.2E-03	5.5E-03	5.7E-06	3.2E+02	4.0E-09	3.8E-10	3.4E-11
9.7E+02	9.8E+02	1.4E-03	4.2E-03	1.3E-06	3.2E+02	9.2E-10	6.5E-11	2.8E-11
1.0E+03	1.0E+03	1.5E-03	2.9E-03	0.0E+00	3.2E+02	0.0E+00	0.0E+00	4.7E-14
1.0E+03	1.1E+03	7.4E-04	2.1E-03	0.0E+00	3.2E+02	0.0E+00	0.0E+00	1.0E-16
1.1E+03	1.1E+03	2.1E-04	1.7E-03	0.0E+00	3.2E+02	0.0E+00	0.0E+00	6.4E-19
1.1E+03	1.2E+03	7.6E-06	1.6E-03	0.0E+00	3.3E+02	0.0E+00	0.0E+00	5.9E-19
1.2E+03	1.3E+03	-2.1E-05	1.6E-03	0.0E+00	3.3E+02	0.0E+00	0.0E+00	5.9E-19
1.3E+03	1.4E+03	-2.6E-05	1.6E-03	0.0E+00	3.3E+02	0.0E+00	0.0E+00	5.9E-19
1.4E+03	1.5E+03	-1.2E-04	1.6E-03	0.0E+00	3.3E+02	0.0E+00	0.0E+00	6.0E-19

# Kessler2 - Profile data

			Microphy	sics				
Skewness p	rofiles	2	Profiles					
Height	z <w></w>	$< w'^3 >$	qt_prof	ql_prof	θ_prof	P1_prof	P2_prof	EV_prof
5.0E+00	1.0E+01	8.6E-04	1.0E-02	0.0E+00	3.1E+02	0.0E+00	0.0E+00	1.1E-09
1.6E+01	2.2E+01	5.7E-03	1.0E-02	0.0E+00	3.1E+02	0.0E+00	0.0E+00	1.2E-09
2.9E+01	3.7E+01	1.2E-02	1.0E-02	0.0E+00	3.1E+02	0.0E+00	0.0E+00	1.2E-09
4.6E+01	5.5E+01	1.5E-02	1.0E-02	0.0E+00	3.1E+02	0.0E+00	0.0E+00	1.2E-09
6.6E+01	7.6E+01	1.2E-02	9.9E-03	0.0E+00	3.1E+02	0.0E+00	0.0E+00	1.1E-09
9.0E+01	1.0E+02	3.9E-04	9.9E-03	0.0E+00	3.1E+02	0.0E+00	0.0E+00	1.1E-09
1.2E+02	1.3E+02	-1.6E-02	9.9E-03	0.0E+00	3.1E+02	0.0E+00	0.0E+00	1.0E-09
1.5E+02	1.7E+02	-3.5E-02	9.9E-03	0.0E+00	3.1E+02	0.0E+00	0.0E+00	9.3E-10
2.0E+02	2.2E+02	-5.5E-02	9.8E-03	0.0E+00	3.1E+02	0.0E+00	0.0E+00	8.3E-10
2.5E+02	2.8E+02	-7.1E-02	9.8E-03	0.0E+00	3.1E+02	0.0E+00	0.0E+00	7.3E-10
3.1E+02	3.5E+02	-7.4E-02	9.8E-03	0.0E+00	3.1E+02	0.0E+00	0.0E+00	6.3E-10
3.9E+02	4.3E+02	-6.2E-02	9.7E-03	0.0E+00	3.1E+02	0.0E+00	0.0E+00	4.9E-10
4.7E+02	5.1E+02	-5.5E-02	9.6E-03	0.0E+00	3.1E+02	0.0E+00	0.0E+00	2.9E-10
5.5E+02	5.8E+02	-6.1E-02	9.4E-03	4.7E-07	3.1E+02	0.0E+00	1.5E-12	1.7E-10
6.1E+02	6.4E+02	-8.7E-02	9.2E-03	4.9E-06	3.1E+02	0.0E+00	9.5E-11	1.2E-10
6.6E+02	6.9E+02	-1.1E-01	9.0E-03	7.0E-06	3.1E+02	1.0E-11	2.4E-10	9.7E-11
7.1E+02	7.3E+02	-1.4E-01	8.9E-03	7.3E-06	3.1E+02	6.5E-10	5.7E-10	7.9E-11
7.4E+02	7.6E+02	-1.5E-01	8.8E-03	9.9E-06	3.1E+02	1.5E-09	5.7E-10	8.5E-11
7.7E+02	7.8E+02	-1.5E-01	8.7E-03	9.6E-06	3.1E+02	1.9E-09	4.4E-10	8.8E-11
7.9E+02	8.1E+02	-1.4E-01	8.6E-03	1.4E-05	3.2E+02	2.9E-09	7.9E-10	6.7E-11
8.1E+02	8.2E+02	-1.3E-01	8.4E-03	1.6E-05	3.2E+02	4.1E-09	8.8E-10	5.9E-11
8.3E+02	8.4E+02	-1.2E-01	8.3E-03	1.1E-05	3.2E+02	3.1E-09	5.8E-10	7.5E-11
8.4E+02	8.5E+02	-1.1E-01	8.2E-03	1.1E-05	3.2E+02	3.8E-09	6.4E-10	7.0E-11
8.6E+02	8.6E+02	-9.4E-02	8.0E-03	1.2E-05	3.2E+02	5.3E-09	6.3E-10	6.2E-11
8.7E+02	8.7E+02	-7.9E-02	7.9E-03	8.0E-06	3.2E+02	2.9E-09	3.5E-10	7.3E-11
8.8E+02	8.9E+02	-6.0E-02	7.7E-03	8.9E-06	3.2E+02	4.4E-09	5.6E-10	4.6E-11
9.0E+02	9.0E+02	-4.1E-02	7.3E-03	6.2E-06	3.2E+02	3.2E-09	2.7E-10	5.1E-11
9.1E+02	9.3E+02	-2.2E-02	6.8E-03	3.9E-06	3.2E+02	2.1E-09	1.5E-10	4.0E-11
9.4E+02	9.5E+02	-6.8E-03	5.9E-03	1.9E-06	3.2E+02	9.5E-10	3.6E-11	1.8E-11
9.7E+02	9.8E+02	1.5E-03	4.6E-03	0.0E+00	3.2E+02	0.0E+00	0.0E+00	1.9E-13
1.0E+03	1.0E+03	1.7E-03	3.2E-03	0.0E+00	3.2E+02	0.0E+00	0.0E+00	2.9E-16
1.0E+03	1.1E+03	6.0E-04	2.2E-03	0.0E+00	3.2E+02	0.0E+00	0.0E+00	5.6E-19
1.1E+03	1.1E+03	-5.8E-05	1.7E-03	0.0E+00	3.2E+02	0.0E+00	0.0E+00	5.8E-19
1.1E+03	1.2E+03	2.1E-05	1.6E-03	0.0E+00	3.3E+02	0.0E+00	0.0E+00	5.9E-19
1.2E+03	1.3E+03	-4.6E-06	1.6E-03	0.0E+00	3.3E+02	0.0E+00	0.0E+00	5.9E-19
1.3E+03	1.4E+03	-5.4E-05	1.6E-03	0.0E+00	3.3E+02	0.0E+00	0.0E+00	5.9E-19
1.4E+03	1.5E+03	-1.7E-04	1.6E-03	0.0E+00	3.3E+02	0.0E+00	0.0E+00	6.0E-19